

**X-ray Induced Changes in Electronic Properties of
Stabilized Amorphous Selenium Based Photoconductors**

A Thesis

Submitted to the College of Graduate Studies and Research

In Partial Fulfillment of the Requirements for the Degree of

Master of Science

In the Division of Biomedical Engineering

University of Saskatchewan

By

Junyi Yang

Saskatoon, Saskatchewan

Copyright Junyi Yang, May 2016.

PEMISSION TO USE

In presenting this thesis in partial fulfillment of the requirements for a Postgraduate degree from the University of Saskatchewan, I agree that the Libraries of this University may make it freely available for inspection. I further agree that permission for copying of this thesis in any manner, in whole or in part, for scholarly purposes may be granted by the professor or professors who supervised my thesis work or, in their absence, by the Chair of the Department or the Dean of the College in which my thesis work was done. It is understood that due recognition shall be given to me and to the University of Saskatchewan in any scholarly use which may be made of any material in my thesis.

Request for permission to Copy or to make other use of material in this thesis in whole or part should be addressed to:

Chair of the Division of Biomedical Engineering

57 Campus Drive

University of Saskatchewan

Saskatoon, Canada, S7N 5A9

ABSTRACT

Amorphous selenium and its alloy are important materials for flat panel digital X-ray detectors. The performance of the X-ray detector is directly related to the carrier mobility and carrier-trapping lifetime of amorphous selenium and its alloy. An experiment was conducted to examine the dose rate effects on the carrier-trapping lifetime reduction of amorphous selenium alloy due to X-ray irradiation. In addition, an experiment was conducted to investigate the temperature effects on X-ray induced carrier-trapping lifetime decrease and relaxation process. X-ray induced capacitance changes have been investigated as well. The interrupted field time of flight (IFTOF) techniques are used in order to acquire the carrier-trapping lifetime. Several amorphous selenium alloy films are irradiated under X-ray. The composition of films are a-Se: 0.3% As: 5ppm Cl and the thickness of the films are about 150 μm . Different dose rates, which range from 0.2 Gy/s up to 2 Gy/s, are applied during the irradiation. The experiments are done for both electrons and holes. The dose rate difference does not result in a significant change in the X-ray induced carrier-trapping lifetime decrease. The same set of samples is studied under three different temperatures, 10 $^{\circ}\text{C}$, 23.5 $^{\circ}\text{C}$ and 35.5 $^{\circ}\text{C}$. The X-ray induced hole-trapping lifetime changes at different temperatures are investigated. After irradiation, the hole-trapping lifetime begins to recovery gradually. The temperature during the relaxation process remains unchanged. The change of hole-trapping lifetime is measured by IFTOF measurement. At higher temperature, upon receiving a certain amount of X-ray dose, the hole-trapping lifetime decreases more than it at lower temperature; however, it also recoveries more quickly at higher temperature. The relaxation process at different temperature also gives activation energy for holes. The X-ray irradiation does not result in any capacitance changes for a-Se films.

ACKNOWLEDGEMENTS

I would like to extend my sincerest appreciation to my supervisor, Dr. Safa.O Kasap, for his guidance, leadership, and patience throughout the course of this work. I also want thank my co-supervisor, Dr. Michael.P Bradley, for this encouragement, guidance, and support. I would like to thank Dr. George Belev, for helping me fix the experimental setup problems, prepare samples for experiments and discuss the problems in the experiment phenomenon. I would like to thank Dr. Robert Johanson and Mr. Bud Fogal for their efforts on the initial design of the experimental setup. I would like to thank Dr. Cyril Koughia and Dr. Dancho Tonchev for helping me get familiar with the lab. I would like to thank University of Saskatchewan, Analogic Canada Corp, and NSERC for financial supports. I would like to thank my colleagues Dr. Go Okada, Mr. Farley Chicilo, Mr. Thomas Meyer and Mr. Ozan Gunes for their supports on my course work. Finally, I would like to thank my family for their continuing support and encouragement.

TABLE OF CONTENTS

PERMISSION TO USE.....	i
ABSTRACT.....	ii
ACKNOWLEDGEMENTS.....	iii
TABLE OF CONTENTS.....	iv
LIST OF TABLES.....	vii
LIST OF FIGURES.....	ix
LIST OF ABBREVIATIONS.....	xiv
1. Introduction.....	1
1.1 Introduction.....	1
1.2 X-ray imaging.....	2
1.3 Materials for X-ray Detectors.....	8
1.4 Research Objectives.....	13
2. Background and Theory.....	16
2.1 a-Se structures and properties.....	16
2.1.1 Introduction.....	16
2.1.2 Structure of Amorphous Solids.....	16
2.1.3 Band Theory for Amorphous Semiconductors.....	19
2.1.4 The Atomic Structure of Amorphous Selenium.....	21
2.1.5 Density of States of a-Se and Carrier Transport in a-Se.....	25
2.1.6 Optical Properties of a-Se.....	28
2.2 X-ray Absorption.....	30
2.3 Time-of-Flight and Interrupted-Field Time-of-Flight Transient Photoconductivity.....	33
2.3.1 Introduction.....	33
2.3.2 The Time-of-Flight Measurement Technique.....	33
2.3.3 The Interrupted-Field Time-of-Flight Technique.....	38

2.4 Transient Trap Limited Theories.....	40
2.4.1 Monoenergetic Trap Level.....	41
2.4.2 Multiple Trap Distribution.....	44
2.5 Capacitance.....	46
2.6 Summary.....	47
3. Experimental Procedure.....	50
3.1 Sample Preparation.....	50
3.2 X-ray Dose Measurement.....	54
3.2.1 X-ray Tube System.....	54
3.2.2 X-ray Dose Measurement System.....	55
3.2.3 X-ray Dose Rate Adjustment.....	56
3.3 Carrier-trapping Lifetime Measurement and IFTOF Experiment.....	57
3.3.1 Overview.....	57
3.3.2 Laser and Trigger System.....	62
3.3.3 High Voltage Switch.....	64
3.3.4 Amplifier System.....	66
3.3.5 Control and Data Acquisition System.....	67
3.4 X-ray Induced Carrier-trapping Lifetime Changes.....	69
3.4.1 Accumulated Dose Measurement.....	69
3.4.2 Lifetime Recovery Measurement.....	70
3.5 Temperature Control Systems.....	71
3.6 Measurement of Capacitance Changes Due to X-ray.....	72
3.6.1 Capacitance Measurement.....	72
3.6.2 Long Time Irradiation Measurement.....	73
3.7 Summary.....	73
4. Results and Discussion.....	75
4.1 Introduction.....	75
4.2 Experimental Calculation of X-ray Dose Deposited in the a-Se Samples.....	75
4.3 X-ray Dose Rate Dependence of Carrier-trapping Lifetime Reduction.....	77
4.4 Temperature Dependence of X-ray Induced Hole-trapping Lifetime Changes.....	87
4.5 Capacitance Changes Due to X-ray Irradiation.....	94
4.6 Summary.....	95
5. Conclusion and Summary.....	97
5.1 X-ray Induced Electronic Properties Changes for Amorphous Selenium.....	97

5.2 Future Works.....	99
6. Reference.....	101
Appendix A.....	106
Appendix B.....	110

LIST OF TABLES

Table 3.1 Working cycle of the X-ray tube.....	55
Table.4.1 Dosimeter measurement results for Gendex GX-1000 at 75Kvp at different position and different filament current.....	76
Table.4.2 Dose deposited rate at 40um beneath the surface.....	76
Table 4.3 Theoretical dose rate estimation based on inverse square law.....	77
Table 4.4 Different interruption times for IFTOF measurements.....	78
Table 4.5 The transient voltage drop ratio for different interruption time.....	79
Table 4.6 Carrier-trapping lifetime before irradiation.....	80
Table 4.7 Different dose rate chosen for electron and hole measurement.....	81
Table 4.8 The dependence of the normalized lifetime change rate of holes on the dose rate.	83
Table 4.9 The dependence of the normalized lifetime change rate of electrons on the dose rate.....	84
Table 4.10 Hole-trapping lifetime before irradiation at different temperatures.....	87
Table 4.11 The normalized lifetime change rate of hole at different temperature.....	89
Table. 4.12 Comparison with previous measurement on normalized lifetime change rate at different temperature.....	89

Table 4.13 Structural relaxation time for different temperature.....	92
Table 4.14 Comparison with previous electron measurement.....	93
Table 4.15 Samples used in effective capacitance measurements.....	94

LIST OF FIGURES

Figure 1.1	A typical projection radiography system consists of X-ray tube, collimator and X-ray detector.....	3
Figure 1.2	A typical structure of indirect conversion X-ray detector.....	5
Figure 1.3	A flat panel amorphous selenium based X-ray detector from Analogic Canada Corporation.....	5
Figure 1.4	A cross-section view of a-Se direct conversion X-ray detector.....	7
Figure 1.5	A section of active matrix array structure thin film transistors.....	8
Figure 1.8	A breast image taken by a-Se based flat panel X-ray detector.....	10
Figure 2.1	The bonding arrangements for crystalline and amorphous solids.....	17
Figure 2.2	Density of states models for crystalline and amorphous semiconductors.....	19
Figure 2.3	The selenium chain model.....	22
Figure 2.4	The random chain model of the structure a-Se with both chain-like and ring-like regions.....	23

Figure 2.5	The structure and energy of simple bonding configurations for selenium atoms.....	24
Figure 2.6	The VAP defects with a distribution of a net charge.....	25
Figure 2.7	Density of states model suggested by Abkowitz.....	25
Figure 2.8	Generalized DOS model.....	27
Figure 2.9	Density of states distribution for shallow traps.....	27
Figure 2.10	Absorption coefficient and quantum efficiency as a function of incident photon energy ($h\nu$) for various applied fields.....	29
Figure 2.11	A typical spectrum of X-ray at 75Kvp coming from a tungsten X-ray tube..	30
Figure 2.12	A typical schematic of TOF measurement.....	35
Figure 2.13	Simulated TOF signal.....	38
Figure 2.14	A typical waveform of IFTOF measurement.....	40
Figure 2.15	A schematic of carrier transportation under multiple traps distribution.....	46
Figure 3.1	NRC 3117 stainless steel vacuum coater system.....	51
Figure 3.2	Schematic diagram of the NRC 3117 vacuum deposition system used to make the samples in this study.....	51
Figure 3.3	Hummer VI sputtering system.....	52
Figure 3.4	Schematic diagram of the Hummer VI sputtering system used to generate contacts on the a-Se samples.....	53

Figure 3.5	A 150um thick a-Se:0.3% As:5ppm Cl sample.....	53
Figure 3.6	Gendex GX-1000 X-ray system and lead chamber protection.....	54
Figure 3.7	Keithley 35050 Dosimeter and Ion chamber for X-ray exposure measurement.....	55
Figure 3.8	An example of dose calculation by dose.py.....	56
Figure 3.9	A movable white sample holder holds the a-Se film. The film can be moved closer to X-ray tube or further away. The laser optical fiber is placed beneath in order to generate injected carriers at the surface of the sample.....	57
Figure 3.10	A schematic process of IFTOF measurement.....	58
Figure 3.11	A typical IFTOF signal.....	59
Figure 3.12	A typical example of semi-logarithm plot of ratio of photocurrent drop and interruption time.....	60
Figure 3.13	The TOF/IFTOF system schematic.....	61
Figure 3.14	Partially experimental setup for TOF/IFTOF.....	61
Figure 3.15	Experimental setup inside lead chamber.....	62
Figure 3.16	Trigger timing requirements for LN103C Laser.....	63
Figure 3.17	The PCI-CTR05 interface circuit for generating the trigger system.....	63
Figure 3.18	The Timing signals from the PCI-CTR05 counter board and interface.....	64
Figure 3.19	A 1kV fast switching high voltage HEXFET switch.....	65

Figure 3.20 2-Stage bandwidth difference amplifier with 16dB gain.....	66
Figure 3.21 a) The circuitry of the protection system. b) The timing diagram.....	67
Figure 3.22 GUI user interface in LabView for TOF/IFTOF.....	68
Figure 3.23 Procedure for accumulated dose measurement.....	69
Figure 3.24 Procedure for recovery measurement.....	70
Figure 3.25 A chamber with the thermal controlling system.....	71
Figure 3.26 GenRed RLC 1658 digibridge.....	72
Figure 3.27 Faxitron X-ray cabinet.....	73
Figure 4.1 The interruption field time of flight waveform for three different interruption time.....	79
Figure 4.2 The logarithm of voltage ratio verse the interruption time.....	79
Figure 4.3 Normalized hole-trapping lifetime reduction due to X-ray irradiation at different dose rates.....	81
Figure 4.4 Normalized electron-trapping lifetime reduction due to X-ray irradiation at different dose rates.....	82
Figure 4.5 NLCCR at different dose rates.....	84
Figure 4.6 Normalized X-ray sensitivity versus deposited X-ray dose.....	86
Figure 4.7 Normalized hole-trapping lifetime reduction due to X-ray dose at different temperature.....	88

Figure 4.8	Normalized hole-trapping lifetime versus time on a semi-log plot.....	90
Figure 4.9	The fitting plot of logarithmic structural relaxation time verse inverse temperature.....	93
Figure 4.10	Measured capacitance changes due to X-ray.....	94

LIST OF ABBREVIATIONS

a-Se	amorphous selenium
AMA	active matrix array
EHP	electron-hole-pair
GPIB	general-purpose instrument bus
DOS	density of states
TOF	Time-of-flight
IFTOF	Interrupted-field Time-of-flight
HV	High voltage
ITO	Indium tin oxide
PCB	printed circuit board
PCI	peripheral component interconnect

1. Introduction

1.1 Introduction

Radiography, Ultrasound and Magnetic Resonance are the most widely used diagnostic tools for medical treatments around the world. Among them, X-ray based radiography has been recognized as the most important and common diagnostic tool. From tissue to bones and from breast to chest, they all can be diagnosed with the help of X-ray imaging. The imaging techniques for X-ray imaging have been evolved from Rontgen to Computed Tomography and from 2 dimensional imaging to 3 dimensional imaging. The materials for X-ray films or imaging plates also vary from small atomic number element to large atomic number element. The most recent development of X-ray based radiography is digital imaging technology. Amorphous Selenium (a-Se) is currently used as the main material for mammography, as the direct conversion photoconductor. Amorphous selenium has a lot of advantages as an X-ray photoconductor. Amorphous selenium can be fabricated into large-size uniform films by conventional vacuum deposition techniques. [1] In addition, amorphous selenium based photoconductors have relatively low dark currents compared to other material based photoconductors. [1] The performance of a-Se based X-ray detector is directly controlled by the carrier mobility and carrier-trapping lifetime. Therefore, it is necessary to conduct research on these properties of a-Se in order to improve the overall performance of a-Se based X-ray detectors.

In order to study these properties of a-Se, appropriate measurement techniques need to be applied. Time-of-Flight (TOF) and Interrupted-Field Time-of-Flight (IFTOF) transient photoconductivity measurements are developed aiming to measure the carrier transportation

properties in a-Se. These measurements measure the transient response caused by the carriers induced by a short pulse of light. A bias electrical field is applied to the sample in order to assist the drift of the carriers. The TOF measurement provides the transit time of the injected carriers as they travel through the sample. This is further used to determine the carrier drift mobility, μ . The IFTOF experiment measures the fractional change in photocurrent caused by the interruption of the bias voltage while the carriers are travelling through the sample. The bias voltage is switched off and then backs on after a short period. This fractional loss of transient current determines the deep carrier-trapping lifetime. The product of the mobility (μ) and lifetime (τ), which is found in the TOF and IFTOF experiments, is directly related to the sensitivity of the photo-detector. [1]

TOF and IFTOF experimental systems provide information about the carrier mobility and carrier-trapping lifetime. In addition, these techniques can be applied to investigate how environmental factors would affect carrier mobility and carrier-trapping lifetime. Then, several experiments are developed in order to provide a better understanding of properties of carrier-trapping lifetime. Since the a-Se is used as the material for X-ray detector, it is important to understand how X-ray photons are going to change the properties of the a-Se. Through a better understanding of how the carrier-trapping lifetime of a-Se responds to X-ray effects, better operating modes for a-Se based X-ray detectors could be developed.

1.2 X-ray Imaging

As mentioned before, X-ray based radiographic imaging is one of the most widely used diagnostic techniques. X-ray imaging depends on the imaging technique and detector function. One of the most common X-ray imaging techniques works by measuring the amount of X-ray radiation that has passed through an object. Since different material and composition have different attenuation coefficient for X-rays, the amount of X-ray absorbed

by these objects is different. The amount of X-rays, which pass through the objects, depends on the X-ray photon energy, properties of object and its thickness. [2] X-ray, which passed through the object, is then converted into image on the X-ray detector. The attenuation difference makes it possible to distinguish different materials and structures on the image. A typical system that applies X-ray absorption imaging technique is shown in Figure 1.1 below.

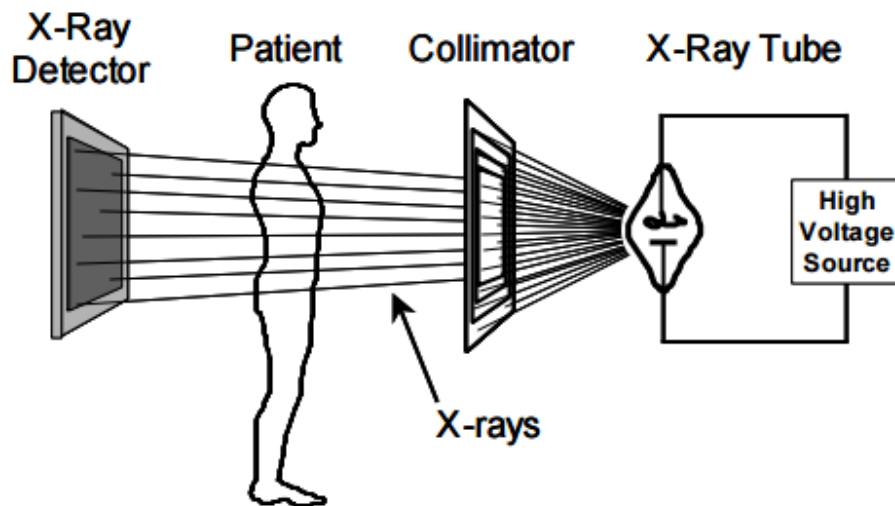


Figure 1.1 A typical projection radiography system consists of X-ray tube, collimator and X-ray detector. After Fogal [3].

X-rays are emitted from a medical X-ray tube. The X-rays are collimated before they reach the patient. The patient body absorbs some of the X-ray photons and the rest of them reach the X-ray detector. The X-ray detector provides imaging of the patient's body depending on the flux of X-rays that reach the detector. This X-ray absorption imaging technique works well for both tissues and bones; therefore, it is the most common X-ray technique used in hospitals. This method has a relatively low resolution compared to Magnetic Resonance Imaging (MRI) and a relatively high risk since the patient's body absorbs most of the X-ray photons. Hence, some other X-ray based imaging techniques, like diffraction enhanced imaging and K-edge subtraction imaging, have been studied in recent years. However, most medical X-ray tubes cannot be used as the X-ray source for these techniques; therefore, these techniques are only designed and tested for synchrotron

radiation imaging. [5][6]

For conventional medical imaging, X-ray absorption based radiography is still the mainstream diagnostic technique. In order to improve the performance of the X-ray imaging system, an improvement of X-ray detector should be achieved. The original radiography detector consists of a phosphorescent screen and a film. Together they serve as an X-ray cassette. The cassette is inserted into radiography system before the exposure and transferred to a separate place for imaging processing after irradiation. It takes a long time to acquire the X-ray image and it is very inconvenient for frequent X-ray imaging demands. In order to improve the efficiency, digital radiography is developed. The digital X-ray detector would convert the X-ray incident photon intensity into electronic response. The magnitude of the electronic response depends on the intensity of X-ray that hits the panel. Based on how the X-ray detector converts the X-ray photon into electronic response, X-ray detectors can be divided into two groups.

There are two methods to convert the X-ray photon intensity into electronic response: indirect conversion and direct conversion. Indirect conversion is a two-step conversion process. The X-ray photons are first coupled with scintillation screen, which converts the X-ray photons into the photons of visible light wavelength. Based on the amount of X-ray photons absorbed by the scintillation screen, different fractions of visible-wavelength photons will be generated. These photons are then collected by photodiodes. Some of indirect conversion X-ray detectors have optical fiber to aid the transmission of photons. [7] These photodiodes would further convert these visible lights into electronic response. The computer will use the electronics response to construct the image. A typical setup of an indirect conversion X-ray detector is shown in Figure 1.2.

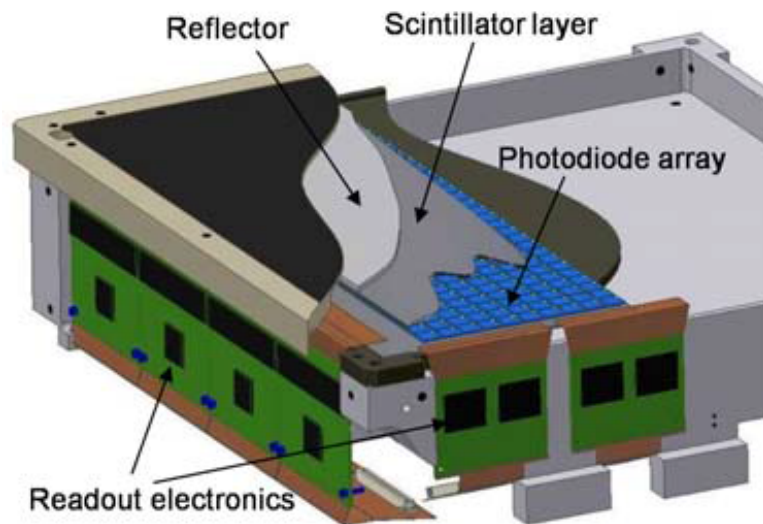


Figure 1.2 A typical structure of an indirect conversion X-ray detector. A reflector is used as a filter, which only allows designed X-ray to reach scintillator layer. The scintillator layer absorbs X-ray photons and emits visible light, which is then absorbed by photodiode array. After Kim et al [8].

In a direct conversion detector, the detector will directly convert X-ray photons into electronic response. An X-ray sensitive photoconductive material based film or panel will absorb the incoming X-ray photons. The field created by the bias voltage will separate the electron and hole generated by X-ray photons. These carriers will then drift under the field and be collected by electrodes. A typical direct conversion X-ray detector is shown in Figure 1.3.

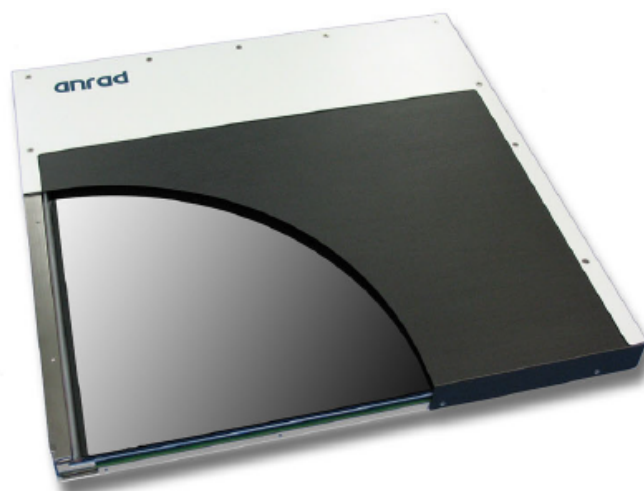


Figure 1.3 A flat panel amorphous selenium based X-ray detector from Analogic Canada

Corporation. After Kasap et al [9].

Direct conversion detectors have several advantages over indirect conversion detectors. The inherent resolution for direct conversion X-ray detector is better than that for indirect conversion X-ray detector. [3] In direct conversion, the X-ray generated charged carriers drift perpendicular to the imaging plane, which makes the position on the readout plane matches the position on the absorption plane. This helps to reduce the lateral spread of the x-ray image. In indirect conversion, even though optical fiber and lens setup help to reduce spread out of the light emitted by the scintillating screen, it dose not perfectly match. In addition, using new material and improving the relationship between bias voltage and material can improve the sensitivity of direct conversion X-ray detector. [10] On the other hand, for an indirection conversion X-ray detector, improving the performance of the scintillation screen is the only way to improve the x-ray sensitivity of the system.

One of the most common direct conversion X-ray detectors is the large area digital flat-panel x-ray detector. This technology relies on the Active Matrix Array (AMA) technology to capture the data. [11] This AMA technology is widely used in liquid crystal display and other imaging technologies. An AMA circuit consists of a lot of small image-producing element, pixel. Each pixel contains a mall charge capacitor and a thin-film-transistor (TFT) switch. [3] These small pixels are placed in an N by M array and then form a complete display AMA circuit. For a direct conversion x-ray detector, a layer of X-ray photon conversion material is coated onto the surface of the AMA. A thin layer of semi transparent metal contact is deposited on the X-ray photon conversion layer. This contact layer serves as the electrode, which makes possible to apply a bias voltage across the X-ray conversion material layer. A cross section of an individual pixel is shown in Figure 1.4.

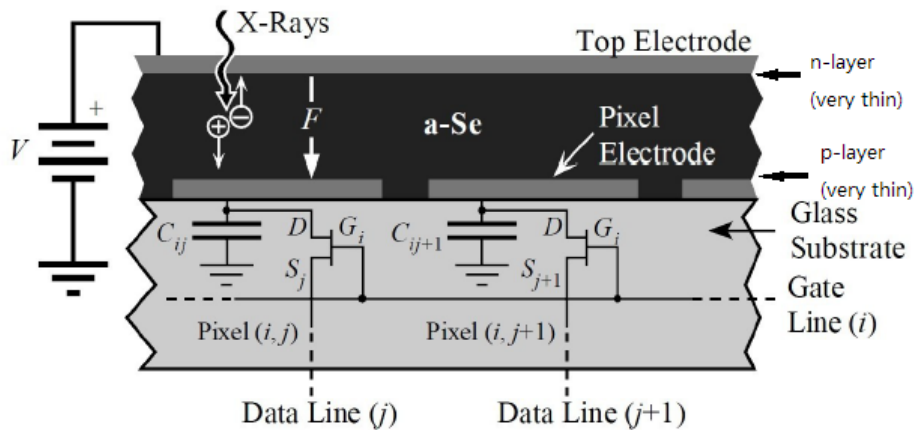


Figure 1.4 A cross-section view of a-Se direct conversion X-ray detector. Adapted from Fogal [3].

For a typical direct conversion X-ray detector, the layer of X-ray photosensitive material will absorb the X-ray photons that pass through the patient. This layer serves as the photoconductor and converts X-ray photon into electron-hole pair. Depending on the bias voltage, the surface contact layer will collect one type of carriers and the other type of carriers will be collected by each pixel. The voltage change of will be determined by number of charges stored in the capacitor of pixel. The total x-ray image can be constructed based on the charges collected by the pixels in the AMA. The image can be read from the AMA by carefully coordinating the activation of the TFTs in the array. For transistors in a row, a Gate Line connects all their gate terminals. For transistors in a column, a Data Line connects all their source terminals. For each transistor, its drain terminal is connected to the capacitor corresponds to each pixel. The data information is transferred to digitizer and collected by computer row by row. When the Gate Line for a row is activated, then the entire row is on and the stored charge in each capacitor is passed onto each corresponding Data Line. The charge signals from transistors in a row are collected column by column through each Data Line. The charge signal will be converted into digital signals by digitizer before computer collects it. The process continues until charges from all rows are collected. The computer then uses the data to reconstruct the X-ray image. A small section of an $M \times N$ AMA is shown in Figure 1.5.

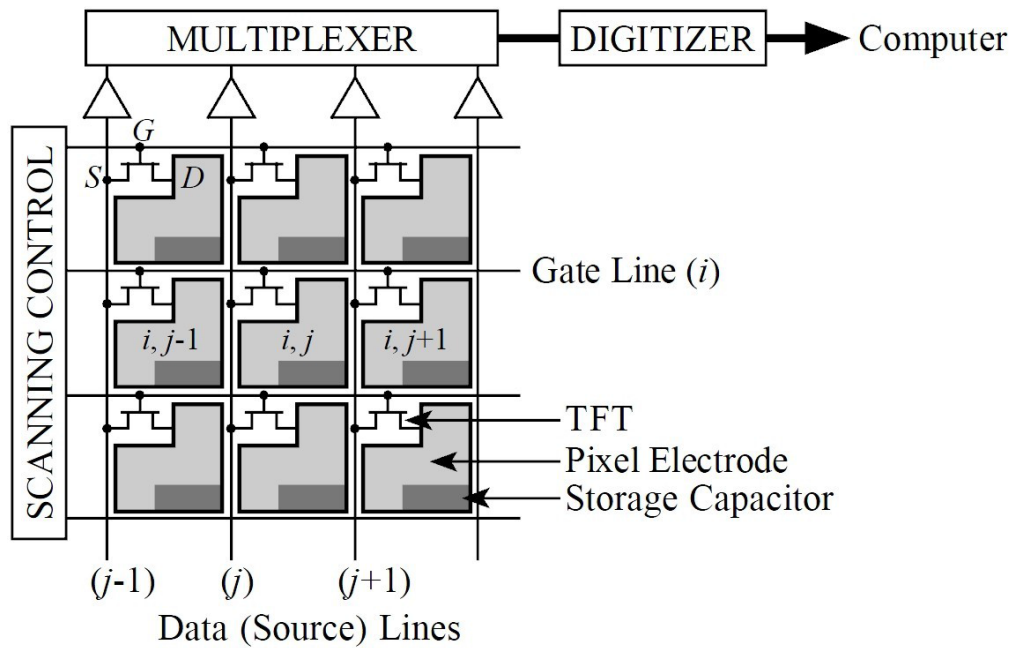


Figure 1.5 A section of active matrix array structure thin film transistors. After Fogal [3]

1.3 Materials for X-ray detector.

The performance of the direct conversion X-ray detector relies on the quality of the photoconductive material. As mentioned before, the performance of the indirect conversion X-ray detector also relies on the quality of the scintillating material for the screen. For the direct conversion X-ray detector, there are several criteria that could be applied to choose the best X-ray photoconductive material. First, the material should have a strong ability to absorb X-ray. In general, for single element material, the larger atomic number of the material, the more X-ray it can absorb. Second, the electron-hole pair creation energy should be as small as possible. Lower electron-hole pair creation energy allows more charges to be generated by the X-ray. Third, the dark current of the photoconductor should be as small as possible in order to provide a high signal noise ratio. There are multiple ways to reduce the dark current, like using a large band-gap material and non-injecting contacts. Fourth, the deep trapping effect within the photoconductor should be negligible. In other words, the Schubweg should be much greater than the photoconductor thickness. Fifth, the longest transit time of the generated carriers should be shorter than the access time for a

pixel. Sixth, the material should be stable. The properties of the material should not be completely destroyed by X-ray. These are criteria for an ideal material for X-ray detector. [3] However, it is extremely hard to find a material that satisfies all the conditions. Normally, an element with large atomic number absorbs more X-ray; however, its band-gap is small, which creates a worse signal noise ratio and large electron-hole pair creation energy. Therefore, continuing research has been done on the current X-ray detector materials in order to understand their electronic properties better and optimize their performance.

As mentioned above, there are some parameters that could be used to decide whether the material is suitable for X-ray detector or not. The X-ray absorption depth provides information of whether the materials have good X-ray absorption. The X-ray absorption depth δ gives the thickness of the photoconductor needed to absorb 63% of the incident X-ray photons. Twice thickness of the X-ray absorption depth will absorb 86% of the incident X-ray photons. The X-ray absorption depth depends on the X-ray photon energy as well. In general, the large atomic number element has a short X-ray absorption depth. It makes large atomic number element material absorb much X-ray energy with a limited thickness. Another important parameter to evaluate materials for X-ray detectors is electron-hole pair creation energy. The electron-hole pair creation energy is the amount of radiation energy needed to generate a single electron-hole pair. The amount of charges generated by a certain amount of X-ray energy is directly related to this electron-hole pair creation energy. Some research has shown that the electron hole pair creation energy depends on the energy of the mobility gap in amorphous materials based semiconductor. [12] The electron hole pair creation energy also has some dependence on the applied electric field. [13] As mentioned before, in order to have good carriers transportation, the schubweg should be much larger than the thickness of the film. [3] The schubweg is the product of the mobility (μ), carrier-trapping lifetime (τ), and applied field (E). It gives the average distance a generated carrier will travel without becoming trapped. Conspicuously it depends on the applied electrical field. In order to have good carrier transportation, the thickness of the

photoconductive material should be much less than the schubweg of the material. For a given material, increasing the applied field is used to increase the schubweg.

Amorphous selenium is a major material that is used in direct-conversion detectors. It is mainly used in digital mammography flat panel X-ray detectors. These flat panel detectors with an AMA using a-Se as an x-ray photoconductor are self-scanning and can produce good images for general x-ray imaging. Since selenium has a relatively small Z number compared to other high Z materials, the optimized X-ray energy range for a-Se based X-ray detector is low X-ray energy range. Therefore, a-Se based X-ray detector is usually used in mammography. A typical breast image taken by a-Se based digital X-ray detector is shown in Figure 1.6

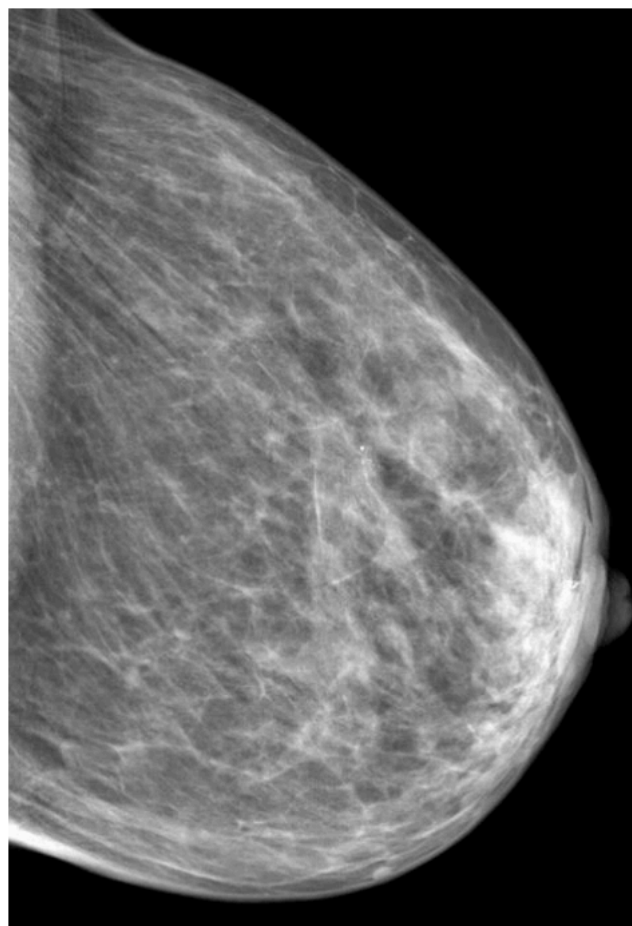


Figure 1.6 A breast image taken by a-Se based flat panel X-ray detector. After Kasap et al [14]

Amorphous selenium can be easily coated onto an AMA panel using conventional vacuum deposition techniques. The deposition process will not damage the thin-film-transistors that are used in AMA circuits. In addition, a-Se has good electron and hole transport properties, acceptable x-ray absorption, and a low dark current. The atomic number of Se is 34 so it is not too small. The X-ray absorption in a-Se depends on the X-ray photon energy. For mammography, the mean X-ray photon energy is 20 keV. A 200 μm layer a-Se would absorb 98% of X-ray photons. For chest radiography, the mean X-ray photon energy is about 60 keV. The thickness required to absorb 98% of X-ray photons is about 4 mm. The thickness of amorphous selenium required to absorb most of X-ray in chest radiography is so large that it makes it impossible to use a-Se based X-ray detector for chest imaging. It is because it is very difficult and expensive to deposit the photoconductor onto the AMA with large thicknesses while still maintaining the uniformity and preventing defects from occurring. In addition, the large thickness requires a higher bias voltage and it could be as high as 10 kV. For a-Se, its electron-hole pair creation energy decreases as the applied field increases. The relationship of electron hole pair creation energy and applied field can be approximated by [13]

$$W_{EHP} \approx W_{EHP}^0 + \frac{B}{E} \quad (1.1)$$

where W_{EHP} is the electron hole pair creation energy, W_{EHP}^0 is the saturated electron hole pair creation energy (at infinite applied field), B is a constant that depends on the x-ray photon energy, and E is the applied field. The intrinsic electron-hole pair creation energy is about 5 eV. [15] This makes it possible to generate more carriers at a higher field and strengthen the readout signal. With a higher field the schubweg for amorphous selenium also increases, which makes carriers be able to travel longer before they are trapped by defects. For holes in a-Se, the schubweg under a field of 10 V/ μm is about 500 μm . This means that one can make a layer of a-Se with good hole transportation up to 100 μm . However, a higher field normally causes a larger dark current in amorphous selenium based semiconductors. The magnitude of dark current has a dependence of the contact material for the electrode. [16] Amorphous selenium is a good material for X-ray detector especially at

low X-ray energy.

There are other materials that could be used as the material for X-ray detector. Lead oxide has once been considered to be a good candidate for X-ray detector. One of the advantages of lead oxide is that it can absorb a lot of X-ray photons because lead is a heavy metal element with an atomic number 82. Since lead oxide is a modified high Z material, the thickness for lead oxide to absorb high-energy X-ray photons is much less than that for amorphous selenium. This makes lead oxide a better material for chest imaging than amorphous selenium. The schubweg for lead oxide under a field of 3 V/ μm is about 132 μm . Under 10 V/ μm field, the schubweg is about 450 μm . The dark current density of lead oxide with aluminum contact is about 150 pA/ mm^2 when applied field is about 2 V/ μm . [17] Another potential high Z modified material candidate is mercury iodide. The schubweg for mercury iodide at 10 V/ μm is about 10mm. This means that mercury iodide has good carrier transportation. The dark current density for mercury iodide varies from 22 pA/ mm^2 to 1100 pA/ mm^2 under 1 V/ μm . [18] This variation is caused by the different technique applied during the sample preparation. There is another material named lead iodide. Lead iodide has a band gap of 2.3 eV, which is very close to the band gap of mercury iodide. In general lead iodide has a higher dark current density than mercury iodide and a smaller schubweg than mercury iodide. The electron-hole pair creation energy for lead iodide is slightly larger than that of mercury iodide. [18]

Some research also focuses on developing an organic material based X-ray detector. Methylammonium lead iodide perovskite ($\text{CH}_3\text{NH}_3\text{PbI}_3$) is one of the candidates. Organic perovskites are known to be potential solar cell materials. Methylammonium lead iodide perovskite based photovoltaic cells show a high power conversion efficiency of up to 20%. Since methylammonium lead iodide perovskite contains heavy elements lead and iodine, it is assumed to have a good absorption of X-ray photons. One recent research on methylammonium lead iodide perovskite based X-ray detector shows that the mobility

lifetime product is about $2 * 10^{-7} \text{ cm}^2\text{V}^{-1}$. [19] This gives that schubweg under $10 \text{ V}/\mu\text{m}$ is about $200 \mu\text{m}$. This makes it very difficult to make a thick layer film while still preserve the carrier transportation quality. In addition, some other lead halide perovskite materials have been tested. Colloidal nanocrystals of cesium lead bromide has been tested for its performance as the material for X-ray detector. Previous experiment on cesium lead bromide nanocrystal has shown that it has a very good visible light absorption and exhibits a bright photoluminescence in the visible light range. [20] Since it contains a lot of large Z number materials, it is once thought to have a good absorption for X-ray photon. However, it turns out that cesium lead bromide nanocrystal based films does not have much advantage over the existing materials.

Currently amorphous selenium is still the major material for X-ray detectors, especially for mammography. Alternative materials like lead oxide and mercury iodide have some promising features, but there are also some difficulties in manufacturing. Organic materials are quite limited. Though they have advantages in manufacturing, their performances are not good enough. Therefore, currently, it is still important to understand amorphous selenium better and improve the performance of amorphous selenium based X-ray detector.

1.4 Research Objectives

This research focuses on the X-ray irradiation effect on carrier transportation. It includes the investigation of X-ray irradiation effects on carrier-trapping lifetime in the amorphous selenium and the capacitance of the amorphous selenium samples. One of the main objectives of the research is to investigate if there is an X-ray dose rate dependence of X-ray induced carrier-trapping lifetime changes in the amorphous selenium. The other main objective of the research is to investigate the X-ray induced carrier-trapping lifetime changes under different temperatures.

The carrier-trapping lifetime of the amorphous selenium is obtained through interrupted field time of flight measurement. The measurement essentially measures the transient current caused by carrier drift. In order to measure the transient current, amorphous selenium based thin film samples need to be prepared initially. The structure of the samples should be amorphous selenium material sandwiched by two electrodes. In interrupted field time of flight measurement, the carriers are excited by ultra short laser pulse and drift under external field. The field is interrupted during the transient. The transient signal loss before and after field interruption provides the information about carrier-trapping lifetime. Therefore an experiment setup that could realize the interrupted time of flight measurement should be built.

Based on the previous experiments, X-ray irradiation creates defects in amorphous selenium and it changes the carrier-trapping lifetime. The carrier-trapping lifetime decreases upon receiving X-ray dose. It brings out the question if there is a X-ray dose rate dependence. Some biological systems not only have dose dependence but also dose rate dependence. In addition, understanding the dose rate effects on the performance of X-ray detector provides some information about designing the X-ray tube. Adjusting the output of the X-ray tube and adjusting the dose that reaches the samples achieve the dose rate adjustment. The dose rate dependence is investigated for both electrons and holes.

Previous research has also shown that X-ray induced carrier-trapping lifetime changes have temperature dependence. [21] The experiments were done on electron-trapping lifetime. In the accumulated dose measurements, the electron-trapping lifetime decreases as dose increases; in addition, same amount of dose generates more defects at higher temperature than that at lower temperature. The temperature variance has been investigated on electron-trapping lifetime relaxation process as well. The X-ray induced defects gradually disappear with respect to time. In previous experiments, at higher temperature, X-ray induced defects disappears much faster than those at lower temperature.

The previous experiments did not include hole-trapping lifetime; therefore, a similar experiment should be done on holes in order to see if both carriers share the same temperature dependence.

An additional experiment could be done on X-ray induced capacitance changes for amorphous selenium. Theoretical analysis has suggested that X-ray induced defects are charged defects. Since polarized dipole moments in the material would change the capacitance, a capacitance measurement could be done on amorphous selenium films to see if X-ray has induced polarized dipole moments in the amorphous selenium.

2. Background and Theory

2.1 a-Se structure and properties

2.1.1 Introduction

The major application of amorphous Selenium (a-Se) today is photoconductor in flat-panel x-ray imaging detectors. Its ability to directly convert X-ray photons into electronic charges makes it an appealing material for Mammography X-ray detector. Since the optical and electronic properties of a-Se significantly affect its performance as the photoconductor, it is important to understand its structure and properties. Theoretically, the band theory for solids provides a good theoretical base to study the properties of a-Se. In a crystalline solid, a band model can be easily derived due to the periodicity of the crystal. However, the disorder of an amorphous solid, like amorphous selenium, makes the derivation of an exact model extremely difficult. Nevertheless, a band model for amorphous solids can be found through noting the similarities to crystalline solids, as well as using experimental observations. Therefore, an experiment technique named TOF/IFTOF measurement is introduced to study the electronic and optical properties for amorphous selenium. Through TOF/IFTOF measurement, the transportation of carriers in the bulk structure of a-Se can be analyzed.

2.1.2 Structure of Amorphous Solids

The majority of solid materials can be divided into two groups: amorphous solids and

crystalline solids. The bonding structure of crystalline solids and amorphous solids are different and their bonding arrangements are shown in Figure 2.1.

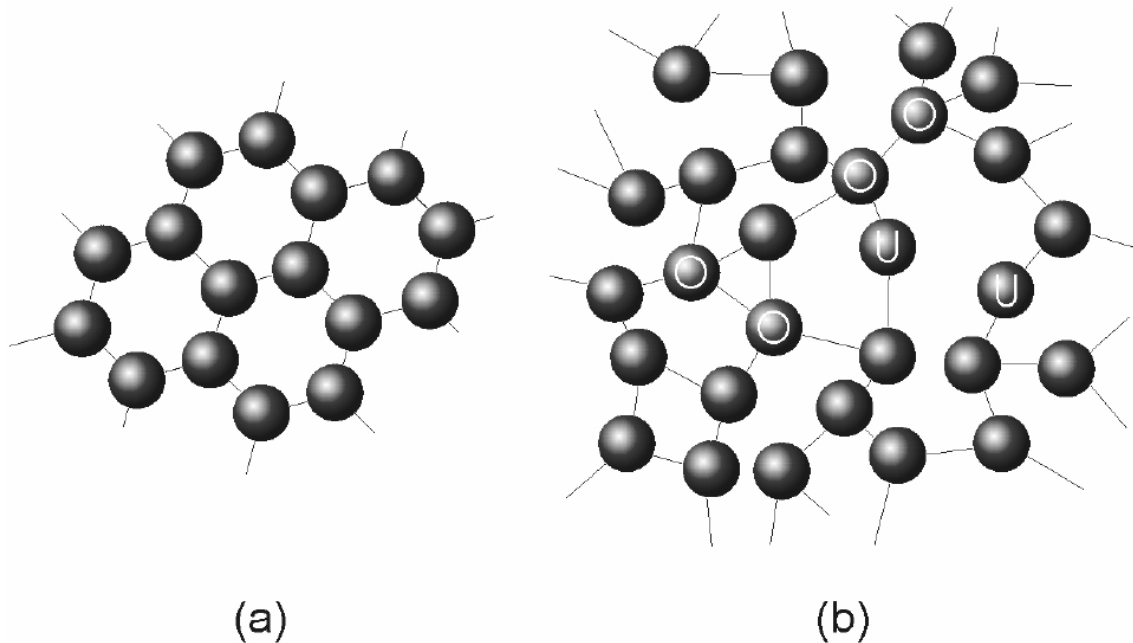


Figure 2.1 The bonding arrangements for crystalline and amorphous solids. The dark spheres in the figure represent the atoms. The lines between the spheres represent the bonds between each atom and its nearest neighbors. A crystalline structure is shown in Figure 2.1 (a). The amorphous structure is shown in Figure 2.1 (b). After Fogal [3].

A solid consists of a three dimensional network of atoms interconnected by atomic bonds. One of the main bonding interactions in solids is the covalent bond. It is formed when multiple atoms share their valence electrons to complete the sub-shells of each atom. The wave function no longer constrains to one atom, instead it overlaps with the whole volume. [3] The number of nearest neighbors of an atom is defined as the coordination number. The difference of crystalline solid and amorphous solid is decided by the difference of bond information and coordination number. As shown in Figure 2.1 (a), the crystalline structure exhibits a highly ordered arrangement of atoms. For each atom, the coordination number is the same and the bond lengths are all equal. Additionally, the bond angles are the same between all atoms. This order carries throughout the crystal and therefore, if the surface states are ignored, the equilibrium position of any atom in the crystal can be determined from any other position in the network. [14] Since such periodicity exists through the whole bulk

structure of the solid, one can define this as long-range order.

On the other hand, an amorphous structure, shown in Figure 2.1 (b), is far more complicated than the crystalline case. The bond length and angles varies from atom to atom. The coordination number is not the same for each atom. Due to such variation, the periodicity is no longer valid beyond a few atom radii. [21] Though there is no long-range order observed in amorphous solids, some short-range order still exists. The short-range order in both amorphous and crystalline structure results in a similar electronic structure in both structures. The overall disorder in amorphous solids also generates various localized electronic states. The energy level and density of these localized states have strong impact on the electronic and optical properties of amorphous semiconductors.

Defects exist in both amorphous solid based semiconductors and crystalline solid based semiconductors. In the crystalline solids based semiconductors, defects are defined as atoms that are not in their equilibrium position. In the amorphous solid based semiconductors, defects are defined as atoms with abnormal coordination numbers. The bonding lengths and angles cannot be specified in the amorphous solids which leaves the coordination number as the major determination method. [22] The normal bonding structure of the atom has the same coordination number as its crystalline structure. A defect in amorphous solid based semiconductors is therefore any atom with a different number of bonds. As shown in Figure 2.1(b), some atoms are labeled with U and some atoms are labeled with O. Atoms labeled with U represent those atoms are under coordinated which means they have a smaller coordination number than the normal ones. On the other hand, atoms labeled with O represent those atoms are over coordinated which means they have a larger coordination number than the normal ones. Both of under and over coordination case introduce localized electronic states. These localized electronic states play a big role in the electronic properties of amorphous solid based semiconductors.

2.1.3 Band Theory for Amorphous Semiconductors

Band models are commonly used to explain the electronic and optical properties of semiconductors. The theory is based on quantum mechanics and is derived by treating a solid as a collection of atoms with specific arrangement. [3] For a single atom, its energy is discrete which can be easily understood through solving Schrodinger equation for a single atom. When a large number of atoms are assembled together, the energy levels may appear to be continuous. The formation of solid through a large quantity of atoms allows the solid to have a continuous band states. Density of states function $g(E)$ is introduced to describe the distribution of electron states per energy per unit volume at energy E . Four different models of density of states distribution are shown in Figure 2.2.

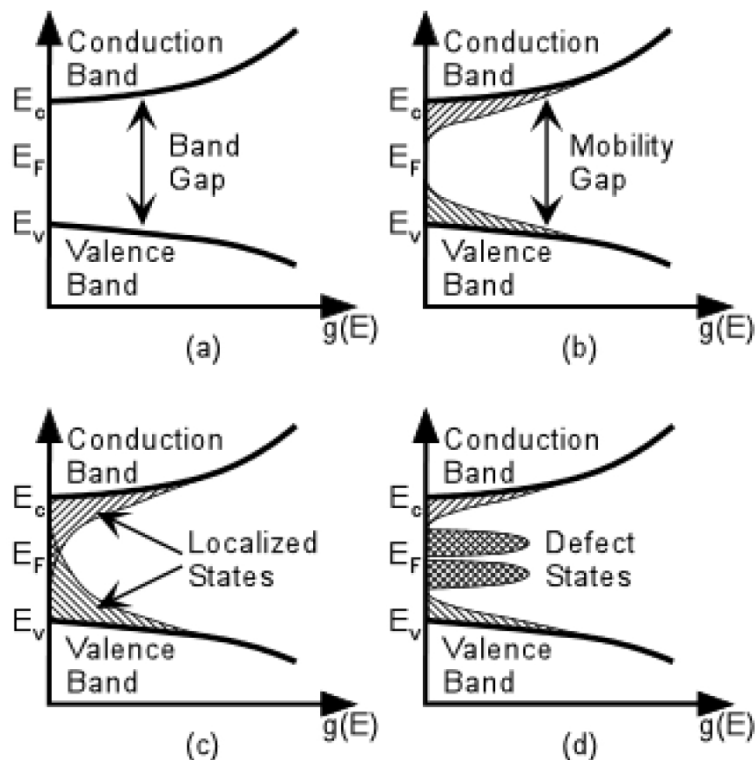


Figure 2.2 Density of states models for crystalline and amorphous semiconductors. (a) Crystalline semiconductor: two bands separated by a forbidden energy region. (b) Initial DOS model for amorphous semiconductors; localized states encroach into the band gap. (c) The CFO model; the localized states extend all the way into the band gap and overlap. (d) Marshall and Owen model; structural defects create a large number of localized states deep in the band gap. After Fogal [3].

Figure 2.2 shows band diagrams for different phase of solids. The density of states model for crystalline semiconductors is shown in Figure 2.2 (a). It is one of the most simplified models for density of states of crystalline semiconductors. It considers periodicity of the crystalline structure as the key concept. A region of forbidden energy states separates only two bands of allowed energies. The lower band is known as the valence band while the upper band is known as the conduction band. The valence band is filled with electrons, so in principle electrons are not able to freely move in the valence band. The conduction band is almost completely devoid of electrons so that an electron can move freely in the conduction band. In addition, the travelling of electrons in the conduction band would result in an electron current. The region between the conduction band and the valence band is known as the band gap. Band gap energy is determined by the energy difference between the conduction band edge energy E_C and valence band edge energy E_V .

The density of states model for crystalline semiconductor is relatively simple due to its long-range order feature. Since the situation for amorphous semiconductor is relatively complicated, more than one models are introduced. The initial attempting comes from the modification of density of states model for crystalline semiconductors by N.F Mott. [23] Mott noticed that for crystalline semiconductors, the electrons could be well described by extended Bloch wave functions that possess long-range order in both amplitude and phase. He hypothesized that for amorphous semiconductor, the extended Bloch wave function possesses long-range order in amplitude but short-range order in phase. This difference would result in an encroachment of localized electron states into the forbidden gap region. As shown in Figure 2.2 (b), the tails of localized states are introduced to both conduction band and valence band. They begin at the band edges and trail off into the forbidden gap. Mott also argued that the transition from the tail of localized states to the extended band states was well defined, corresponding to a sharp increase in mobility where the extended band states began. [24] Electrons in the tail of localized states move with mobility controlled by thermally activated tunneling between states, while electrons in the extended band states would move with a mobility determined by the electron's effective mass in the solid and scattering from potential fluctuations due to the randomness in the structure. A concept called the mobility gap is

introduced based on such a mobility transition. This mobility gap for amorphous semiconductor is analogous to the band gap for crystalline semiconductors.

Cohen, Fritzsche, and Ovshinsky later expanded the original model developed by Mott. [25] When they considered both topological and composition disorder, they believed that number of disorders in amorphous semiconductors should be larger than what Mott model states. They postulated that, the localized tail states extended much deeper into the mobility gap and overlapped around the Fermi level. Even though there would be a continuous distribution of states throughout the mobility gap, metallic conduction would not occur because the gap states are still highly localized in space. This model is referred to the CFO model.

In addition, there are over coordinated and under coordinated atoms in amorphous solid based semiconductors. These structures may cause some local defects such as dangling bonds, chain ends, vacancies, substitutable impurities, and interstitials. Due to these defects, there will be additional localized states within the mobility gap. Another model, by Marshall and Owen, has taken these local defects into consideration. [26] They argue that these defects caused by the abnormal coordinated structure should result in a significant density of mid-gap states. As shown in Figure 2.2 (d), there are two regions of localized states in the mobility gap. These states form two small bands, which look like donor and acceptor states in the doping case. The Fermi level is determined by these mid-gap states and appears to be in the middle of gap. The amount and distribution of these local states will affect the electronic properties of amorphous solid based semiconductors.

2.1.4 The Atomic Structure of Amorphous Selenium

Selenium has an atomic number of 34, and belongs to Group VI in the periodic table. The elements in this group are normally referred to chalcogens. Six valence electrons in the outermost shell can occupy eight states. There are normally two different types of non-bonding states for chalcogens. Two electrons in the s-states form a lone pair and another

two electrons in p-state form another lone pair. Two remaining electrons in the p-state are used to form bonding with electrons from other atoms. The lowest energy configuration for Se atoms consists of a two-fold coordinated bonding structure with an optimum bond angle of 105° and dihedral angle of 102° . [27]

There are two different forms of Se in its crystalline phase due to the two-fold coordinated bonding structure. α -Monoclinic Se (α -Se) and trigon Se (γ -Se) are the different forms of Se. In α -Se, the atoms bond together and form rings that contain eight Se atoms. [27] The trigon structure consists of parallel and spiral Se_n molecule chains. The initial guessing of the amorphous selenium structure contains a mixture of both states. These states are randomly distributed in the solid. In the later study, it is suggested that a ‘random chain model’ is more accurate based on some observation of a-Se structural behaviors. This model specifies that the atoms be linked together in a two fold coordinated chain structure where the magnitude of the dihedral angle ϕ is constant but randomly changes sign. The dihedral angle is defined as the angle between two adjacent bonding planes. Since the angle is defined as the angle between two planes, four atoms totally are required to define the two planes. [27][28] The selenium atoms arrangement for selenium chain model is shown in Figure 2.3.

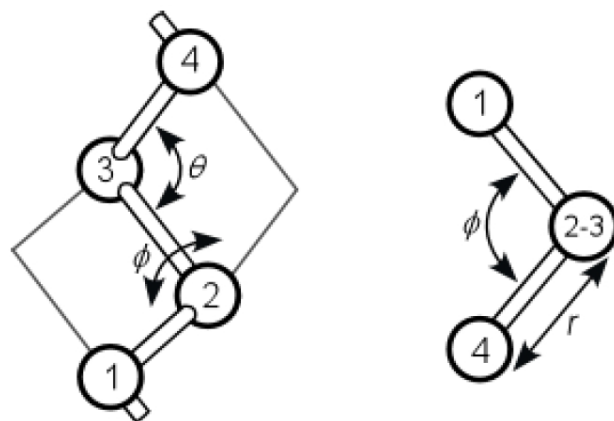


Figure 2.3 The selenium chain model. The dihedral angle ϕ is observed as the angle between the planes formed by atoms 1 and 2 and atoms 3 and 4. The bond angle θ between in plane atoms and the bond length r are also shown. After Kasap [29].

The positions of atoms in the crystalline structures are fixed due to the symmetry, bond length and bond angle. The magnitude of dihedral angle is decided by bond length and bond

angle and its sign depends on which type of crystalline Se is being observed. For trigon Se, the dihedral angle varies to form a spiral pitch of three atoms while its variation forms either chain-like or ring-like structures in α -Se structures. If plus + and minus – signs are used to represent the relative phase of dihedral angles, then the mixture of + and – signs will represent ring structure and mono combination of either + or – will represent chain structure. [27] The example shown in Figure 2.4 contains both ring-like and chain-like structures. The previous notation as +++-+-+--- characterizes it.

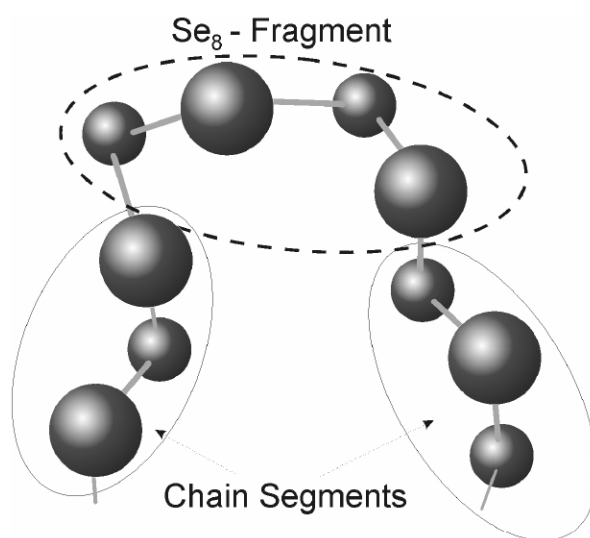


Figure 2.4 The random chain model of the structure α -Se with both chain-like and ring-like regions. After Lucovsky [27]

As shown in the previous section, there are some over-coordinated and under-coordinated atomic bindings in α -Se. These bonding configurations would contribute to the structural defects in the α -Se like amorphous chalcogen. Some of these structural defects are electrically charged while others are neutral. [3] For α -Se, the Electron Spin Resonance (ESR) studies have shown that the possibility for neutral defects is small. [30][31] Therefore, the major contribution to defects would come from thermodynamically derived charged structural defects. These defects are called valence alternation pairs (VAPs). These defects are either a negative charged one-fold Se atom Se_0^- , or a positive charged three-fold Se atom Se_3^+ . These types of defects are prevalent because the formation of a diamagnetic pair of charged over- or under-coordinated VAP centers is energetically more favorable than the formation of singly or triply coordinated defects. [21] The valence alternation pairs can also form intimate

valence alternative pairs (IVAPs) together. The structure and energy of various simple bonding configurations of selenium atoms are shown in Figure 2.5. [32] Figure 2.6 shows possible defects formed by selenium atoms. [9]

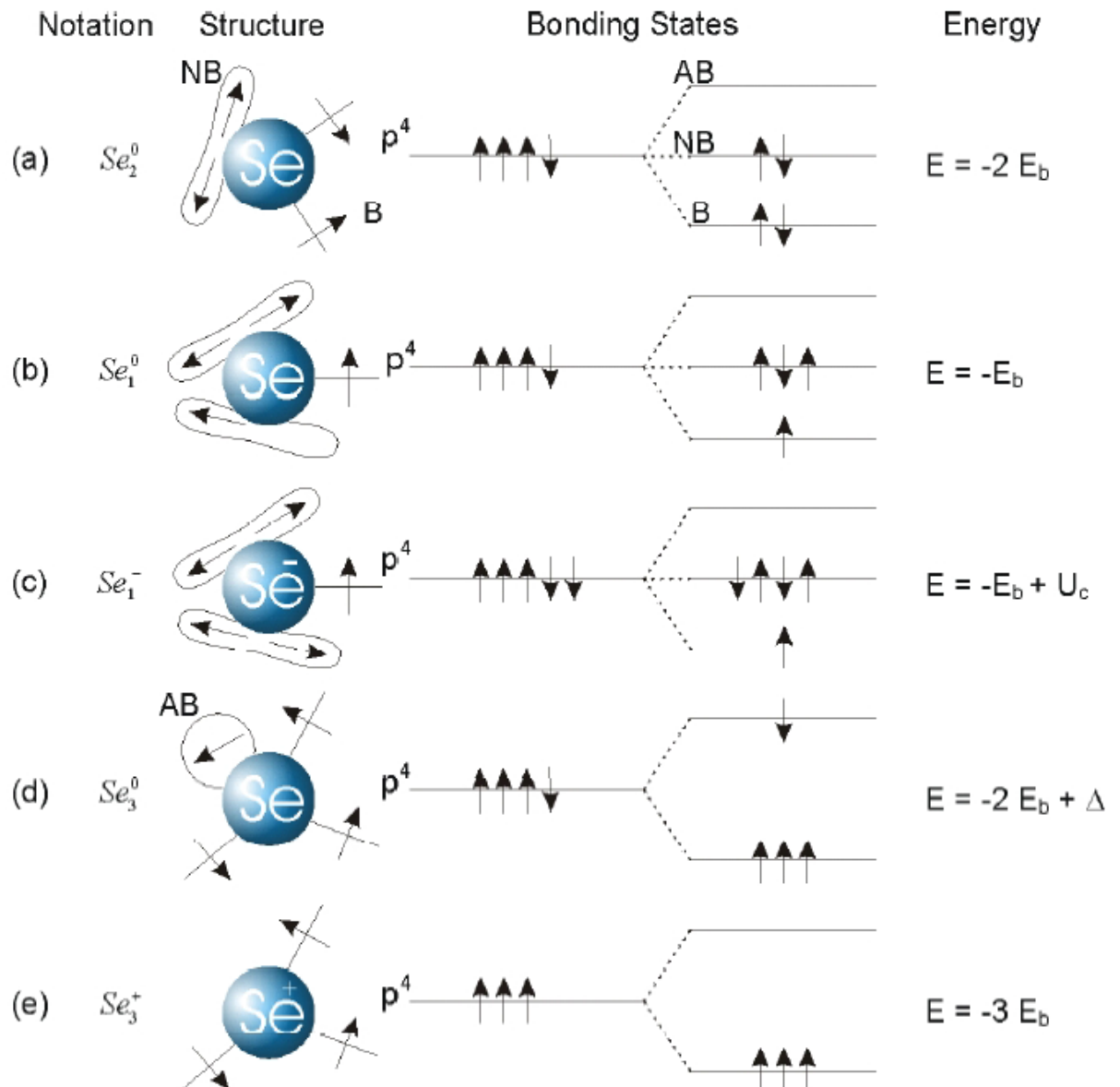


Figure 2.5 The structure and energy of simple bonding configurations for selenium atoms. a) It shows a two-fold coordinated neutral Se atom. b) It shows a one-fold coordinated neutral Se atom. c) It shows a one-fold coordinated negatively charged Se atom. d) It shows a three-fold coordinated neutral Se atom. e) It shows a three-fold coordinated positively charged Se atom. Adapted from Adler et al [32].

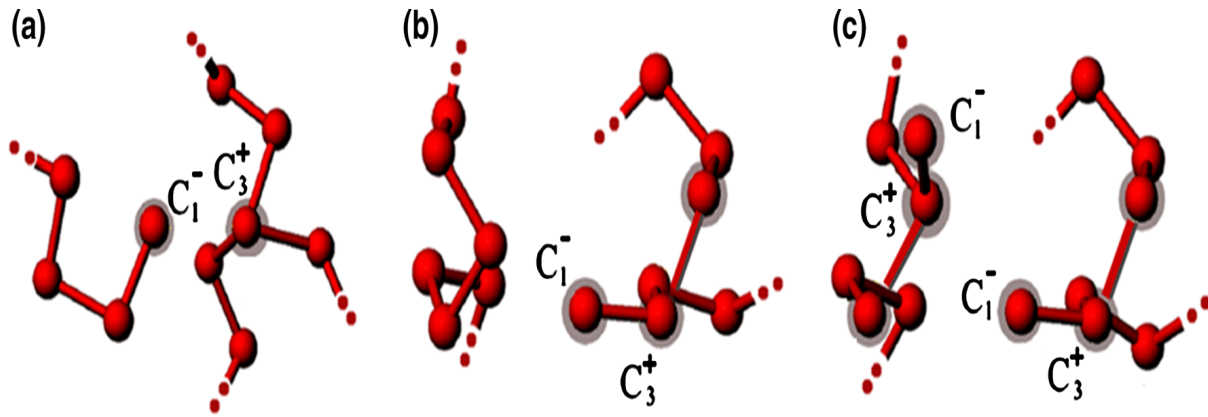


Figure 2.6 The VAP defects with a distribution of a net charge a) two chain VAPs defects. b) Single IVAP defects while a one-fold coordinated negatively charged Se atom C_1^- and a three-fold coordinated positively charged Se atom C_3^+ are on the same side. c) Two IVAPs belongs to different chains and form a common one. After Kasap et al [9]

2.1.5 Density of States of a-Se and Carrier Transport in a-Se

There are various density of states models for a-Se. Abkowitz model as an extension of the Owen-Marshall DOS model has been the most commonly used model. [33] It is shown in Figure 2.7.

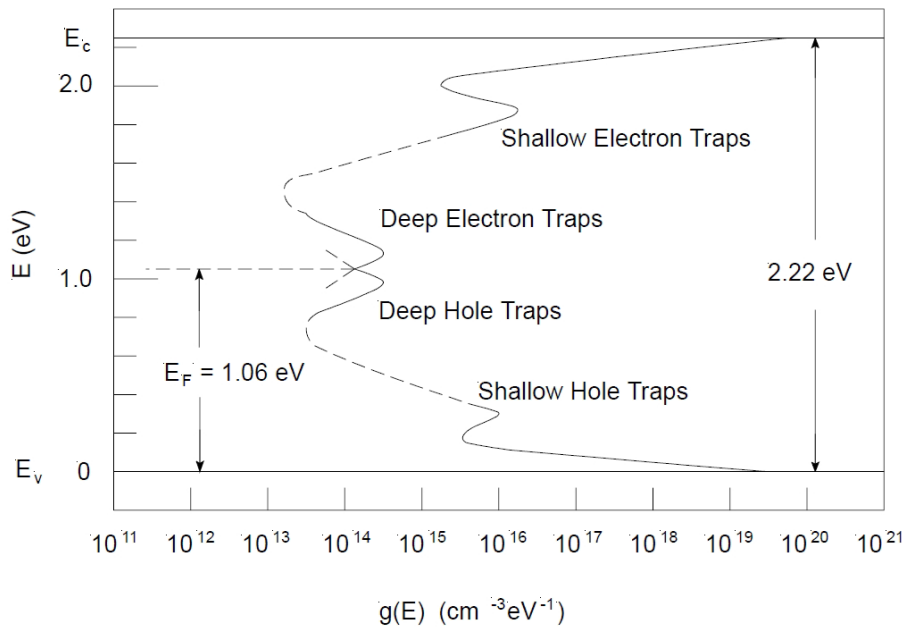


Figure 2.7 Density of states model suggested by Abkowitz. After Abkowitz [33].

It preserves most features of Owen-Marshall model with some additional peaks in the mobility gap. It has a decaying density of localized states from band edges, with two peaks

close to conduction and valence band respectively. These two additional peaks corresponds to localized states named shallow traps while the original peaks close to the Fermi level are known as deep traps. The mobility gap for a-Se in this model is 2.22 eV. [33]

The electron mobility and hole mobility in a-Se are believed to be shallow trap controlled through trapping and releasing process from these shallow traps. [34] The carrier mobility for a-Se, which consists of, a discrete set of monoenergetic shallow traps can be given as [1]

$$\mu = \mu_0 \left[1 + \frac{N_t}{N_v} \exp\left(-\frac{E}{kT}\right) \right]^{-1} \quad (2.1)$$

where N_t is the shallow trap concentration, N_v is the density of states at the valence band mobility edge and E is the energy depth of the shallow traps from the edge. Since the density of states for shallow traps and their energy levels are very crucial to the mobility of carriers, a lot of studies have done to investigate these shallow traps. Based on the Abkowitz's model and some experimental measurements, it has shown that the peak of shallow hole traps is 0.29 eV above the valence band and the peak of shallow electron traps is 0.35 eV below the conduction band. These analyses also suggest that the peak of the deep hole traps is 0.87 eV above valence band and the peak of the deep electron traps is 1.22 eV below the conduction band. [35] The peaks for the deep traps have been measured using photo induced discharge measurements and cycled-up xerographic residual voltage measurements. [36]

Some of the recent works have shown a more detailed analysis for shallow carrier traps distribution. This recent study shows a little different result as the analysis mentioned above. [9] Both of the previous analysis and recent study show that the deep carrier trap's energy level is at least 0.55 eV away from the band edge. The band tails show an exponential behavior. However, the recent study has shown that there are two Gaussian peaks near the conduction band while there is no Gaussian peak near the valence band. Figure 2.8 shows a recent density of state model of amorphous selenium. [9] It provides a distribution in the near band edge region and an estimation of number of deep traps in the amorphous selenium mobility gap. Furthermore, a shallow electron trap distribution is shown in the Figure 2.9 as well. [9]

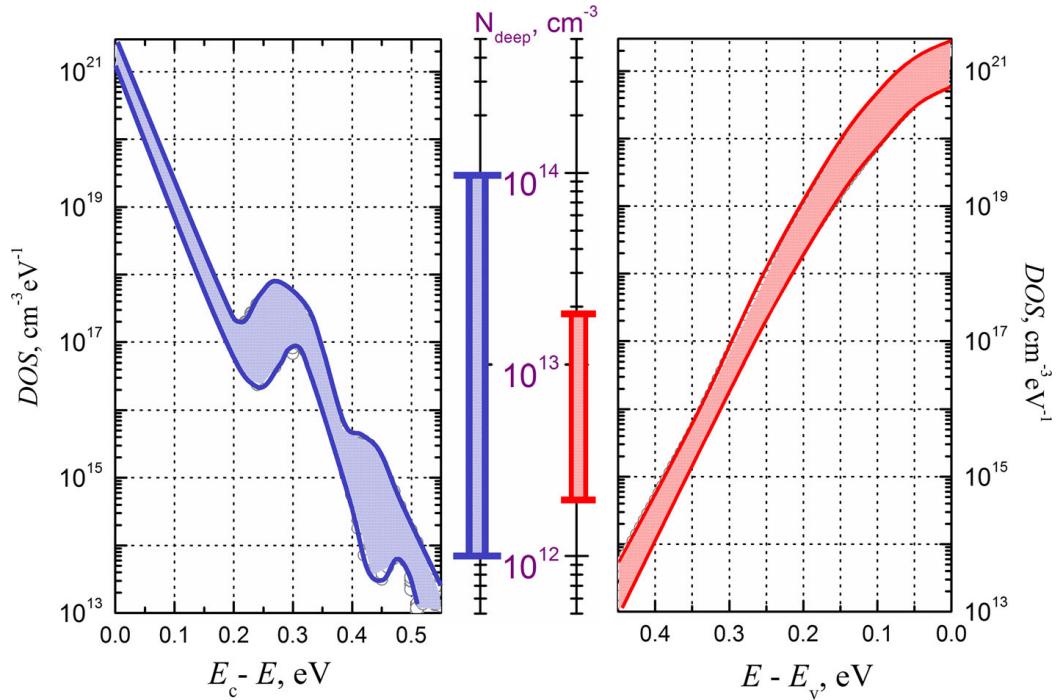


Figure 2.8 Generalized DOS model. The Left side is the DOS in the vicinity of conduction band while the right side is the DOS in the vicinity of valence band. The bars in the center show the concentration of deep carrier traps for both electrons and holes. After Kasap et al [9].

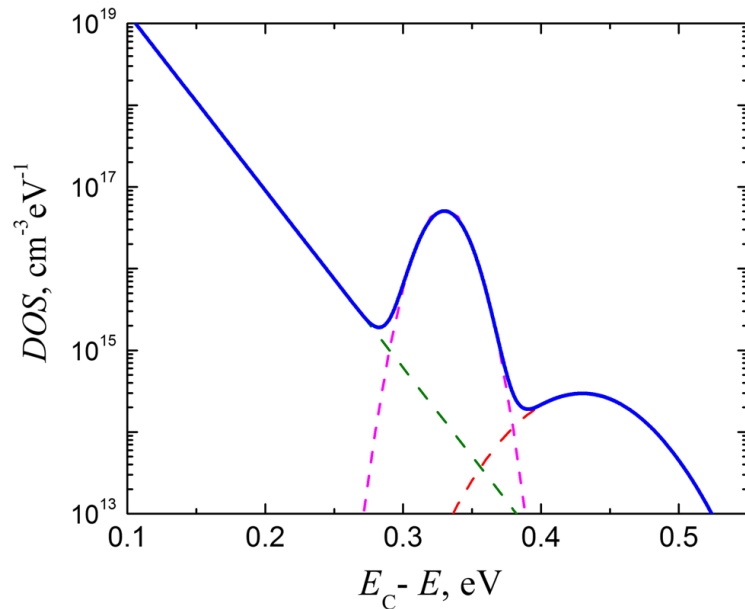


Figure 2.9 Density of states distribution for shallow traps. One Gaussian peak is observed 0.27-0.33eV below the band edge. Another Gaussian peak is observed 0.38-0.48eV below the band edge. After Kasap et al [9]

Evidence has shown that both shallow and deep carrier traps, which are generated by structural defects, are thermodynamically stable at room temperature. [37][38][39] Particularly, the deep traps are important because they are crucial for determining the carrier "schubweg". The sensitivity of the X-ray detector is then decided by these deep trap states.

In addition, some of effort has been devoted to improve the carriers' transportation and structural stability of the a-Se based semiconductor. [40] Impurities and alloying method have been tested on a-Se, and arsenic and chlorine are the most common elements for the research. Arsenic is doped into a-Se in order to increase its stability and prevent a-Se from crystallization. However, arsenic doping would increase number of VAPs and thus undermine the transportation of carriers, especially holes. In order to counter this negative effect on carrier transportation, chlorine is added to compensate the effects brought by arsenic. The balance of arsenic and chlorine would result in a stabilized a-Se with good carrier transportation.

2.1.6 Optical Properties of a-Se

Since a-Se is mainly used for photoconductors, its optical properties are important. Incident photons can excite electrons from the valence band up into the conduction band and the possibility for these photons to be absorbed is determined by the optical absorption coefficient. This coefficient depends on the wavelength of incident light and the magnitude of the density of states at the band edges. For a-Se, the optical absorption coefficient exhibits an Urbach edge of the form [14]

$$\alpha(E) = 7.35 * 10^{-12} \exp\left(\frac{E}{0.058\text{eV}}\right) \text{cm}^{-1} \quad (2.2)$$

This also corresponds to the excitation of charge carriers from the mid-gap localized states into the extended states. [41] At higher photon energies, the absorption coefficient follows different forms. Davis suggests that the absorption coefficient is proportional to [42]

$$\alpha(E) \propto (E - 2.05\text{eV}) \quad (2.3)$$

while Tauc's law shows [43]

$$\alpha(E) \propto (E - 1.9\text{eV})^2 \quad (2.4)$$

Electron-hole pairs (EHPs) are generated once photons are absorbed. An electron from the valence band is excited into the conduction band, while a hole is left in the valence band. Under external field photon excited electrons and holes will drift which result in the photocurrent. In addition, the probability for an electron-hole pair to be separated by the field before recombination is determined by the quantum efficiency. The quantum efficiency exhibits a strong dependence on the external applied field. Onsager theory gives a more explicit analysis for this dependence. In his theory, the quantum efficiency is defined as. [44]

$$\eta = \eta_0 f(E, T, r) \quad (2.5)$$

where η_0 is the quantum efficiency for the intrinsic photon generation process and $f(E, T, r)$ is the probability that an EHP will separate and r is the initial separation of the photo-induced pair. The relationship between X-ray photon energy and absorption coefficient and the relationship between X-ray photon energy and quantum efficiency are shown in Figure 2.10

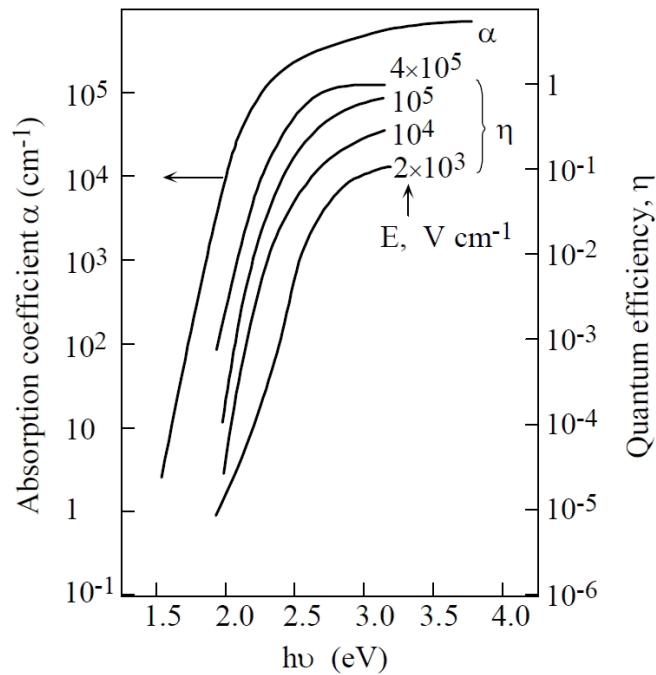


Figure 2.10 Absorption coefficient and quantum efficiency as a function of incident photon energy ($h\nu$) for various applied fields. After Pai et al. [44]

2.2 X-ray absorption

X-ray is essentially one type of electromagnetic waves with photon energies ranging from 100 eV to 100 keV. Since the X-ray source that is used in this research is tungsten X-ray tube, Bremsstrahlung radiation is the major mechanism for generating the X-ray. It is realized by slowing down the high-speed electron from filament current at a tungsten plate. The spectrum of X-ray generated by X-ray normally spreads over a large range. A typical X-ray energy spectrum of a medical X-ray tube is shown in Figure 2.11.

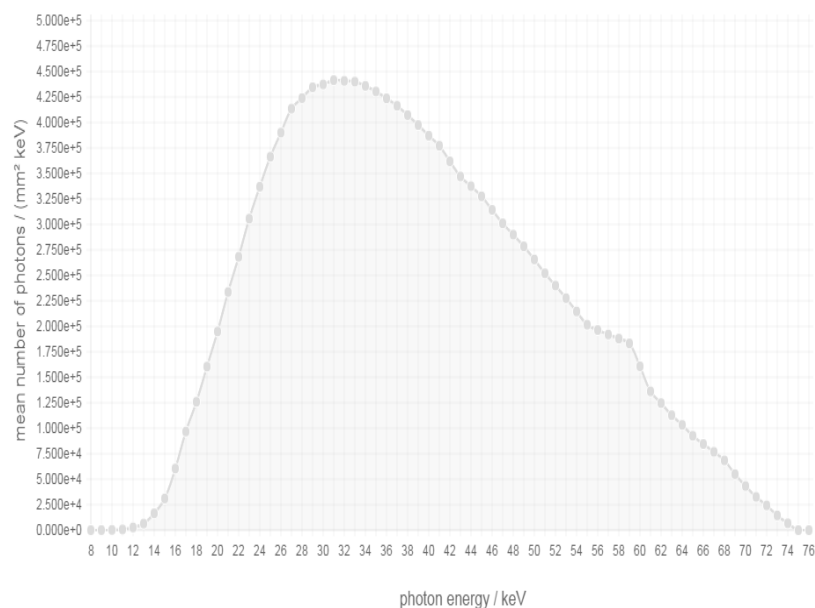


Figure 2.11 A typical spectrum of X-ray at 75Kvp coming from a tungsten X-ray tube. The spectrum was taken from X-ray spectrum simulation program provided by Siemens.

This continuous spectrum of X-ray can be understood for following reasons: [45]

1. The continuously varying voltage difference between the target and the filament, which is characteristic of half wave rectification, causes the electrons striking the target to have varying levels of kinetic energy.
2. Most electrons participate in many interactions before all their kinetic energy is expended. As a consequence, an electron carriers differing amounts of energy at the time of each interaction with a tungsten atom that results in the generation of an X-ray photon.

3. The bombarding electrons pass at varying distances around tungsten nuclei and are thus deflected to varying extents, As a result, they give up varying amounts of energy in the form of Bremsstrahlung photons.
4. Depth of generation of photons in the target.

X-rays interact with matter in different ways. Photoelectric absorption, coherent scattering, Compton scattering and pair production are the four main interactions between X-rays and matter. For medical application, photoelectrical absorption and Compton scattering are the primary interactions. [45] For photoelectric absorption, an X-ray photon collides with an inner shell electron. The electron is excited and ejected from the inner shell. The photon is absorbed and its energy is converted into the kinetic energy of the electron and the binding energy required to excite the electron. For Compton scattering, the X-ray photon is deflected instead of being absorbed. The X-ray photon interacts with an outer shell electron and the electron get excited and recoils. The loss of photon energy is then converted into kinetic energy of electron and dissipated for overcoming the binding energy. The scattered electron can go any direction.

The energy per unit mass absorbed by the sample object is defined as dose. The dose measures the energy density absorbed in the sample and it is a very important quantity to evaluate the X-ray effects for the a-Se X-ray detector. In order to calculate the dose, it is essential to calculate the energy that is deposited into the sample. The X-ray energy absorbed in the sample follows both mass attenuation and energy attenuation. In other words, the X-ray photon energy absorbed inside the sample depends on the depth beneath the sample surface; different X-ray energy attenuates different distance. The energy attenuation at x position for energy E_i is given as

$$E(E_i, x) = NE_i \exp(-\mu_{\text{mass}}\rho x) \quad (2.6)$$

Where μ_{mass} is the mass attenuation coefficient, which can be obtained from NIST websites, ρ is the sample density, and N is total number of X-ray photons, which can expressed as.

$$N = A\psi(E_i) \quad (2.7)$$

Where $\psi(E_i)$ is spectrum of the X-ray tube, A is the irradiation area. Since the X-ray tube

provides a continuous spectrum, it is necessary to figure out the flux at a specific energy. The energy attenuation is linear and can be expressed as

$$dE = \mu_{\text{energy}} \rho E(E_i, x) dx \quad (2.8)$$

Where μ_{energy} is the energy attenuation coefficient. Combining the previous three equations, the total energy absorbed in the thickness $\Delta x = x_1 - x_2$ can be expressed as [21]

$$E = \int_{x_2}^{x_1} \int_0^{\infty} \rho \mu_{\text{energy}} A \psi(E) E \exp(-\mu_{\text{mass}} \rho x) dE dx \quad (2.9)$$

The dose is then obtained as

$$\text{Dose} = \frac{E}{\rho A \Delta x} \quad (2.10)$$

For the actual measurement, since the actual flux of the X-ray tube is unknown, it has to be measurement by the dosimeter and then use the result to normalize flux, which is used to calculate the dose deposited into the sample. The normalized parameter is given as.

$$\psi_{\text{real}}(E) = \frac{Q_{\text{measured}}}{Q_{\text{ideal}}} \psi_{\text{ideal}}(E) \quad (2.11)$$

Where $\psi_{\text{ideal}}(E)$ is a theoretical simulation of the spectrum of the X-ray tube at specific peak-voltage. Q_{ideal} and Q_{measured} are given as. [14]

$$Q_{\text{ideal}} = \frac{e E_{\text{dosimeter}}}{W_{\text{air}}} \quad (2.12)$$

and

$$Q_{\text{measured}} = RV \rho_{\text{air}} 2.58 \times 10^{-7} (\text{C/g}) \quad (2.13)$$

where e is the electron charge, $E_{\text{dosimeter}}$ is the estimated energy that is absorbed by the ion chamber. The theoretical calculation for this energy involves applying Equation 2.9 with photon flux $\psi_{\text{ideal}}(E)$. R is the readout from dosimeter in unit of Rontgen. V is the volume of the ion chamber. By obtaining the real photon flux from the X-ray tube one is able to calculate the actual dose that is deposited into the sample. For average dose that is deposited in a sample, the Δx is equal to the thickness of the sample while for dose at specific location.

$$x_1 = x - \delta x < x < x + \delta x = x_2 \quad (2.14)$$

where $\delta x \ll x$.

2.3. Time-of-Flight and Interrupted-Field Time-of-Flight Transient

Photoconductivity

2.3.1 Introduction

Since amorphous solids have a relative complicated structure, which makes it very difficult to determine the properties of amorphous solids only through theoretical model, experimental techniques are introduced. The major techniques that are applied in this research are time-of-flight (TOF) and interrupted-field time-of-flight (IFTOF) transient photoconductivity measurements, which are developed by Kasap [46][47]. The combination of the two techniques could provide a lot of information about the drift mobility and carrier-trapping lifetime in amorphous semiconductors. The experimental techniques are based on the current transient due to the carriers drift in the bulk of the amorphous solid based semiconductor. The carriers are injected by photons and drift by an external field. The experimental technique captures the signals and also manipulates the drift process. Though TOF is not used in the later research, it is the base for IFTOF. Therefore it is necessary to first understand the principle of TOF measurement.

2.3.2 The Time-of-Flight Measurement Technique

The TOF technique measures the transient response generated by the drift of photo-injected carriers as they travel through a sample of highly resistive material. The carriers are excited by pulse of light. Absorbed photons generate electron-hole pairs. The absorption depth of the excitation must be much less than the sample thickness L in order to have carriers to travel through the sample. [3] Normally, the sample would have a top electrode and a bottom electrode. The light pulse would hit the top electrode and generate the carriers at very surface of the sample. If the absorption depth were in the magnitude of sample thickness, then dual types of carriers might be generated. This would largely interference the measurement of one type of carriers. The absorption depth has to be large enough so that the

top electrodes would not immediately absorb the injected carriers. Other than the wavelength of the light source, the duration of excitation is also important. The duration of excitation has to be relatively small compared to the transient time of carriers. Finally, the number of photons has to be limited. This is because, the TOF measurement has an assumption of weak injection, which would be explain in detail later. An external electrical field is applied through the sample in order to assist carriers' drift. The resistance of sample is normally small enough that the majority of the voltage drops across the high resistivity of the sample. [3] As the injected carriers drift across the sample under the external field, they will induce a photocurrent $i(t)$ through an external resistor. The measurement can be done for both holes and electrons by simply reverse the bias of applied field. In order to have a good and valid TOF measurement, it is crucial to maintain a good condition for the light excitation source.

One of the most important assumption for TOF measurement to be valid is that the internal field is uniform unchanged through the whole sample. [48] The carriers travelling through the sample would affect the electrical field inside the sample. In detail, the electrical field inside the sample at position x can be expressed as [49]

$$E = E_0 + \frac{epw}{\epsilon} \frac{x}{L} \quad (2.15)$$

where E is the electrical field at position x , E_0 is the applied field, e is charge, p is the concentration of the carriers within the charge sheet, w is the width of charge sheet and L is the thickness of the sample. Carriers are considered as a narrow sheet of charges when they travel through the sample. The assumption is that the electrical field within in the sample is independent of position or the effect brought by the carriers can be neglected. [48]

$$\frac{epw}{\epsilon} \ll \frac{V}{L} \quad (2.16)$$

where V is the applied voltage on the sample. The electrical field caused by carriers has to be much smaller than the applied field. This condition can be referred as small signal condition as mentioned before. In experiment measurement, this condition is realized by controlling the number of injected carriers generated by photon excitation. In principle, the total injected carrier charge Q has to be smaller than the charges collected on the electrode, which is CV . C is the capacitance of the sample. This capacitance could be obtained through direct

experiment measurement or theoretical estimation. V is the voltage applied through the sample. The experimental adjustment for small signal condition would be explained in detail later. Figure 2.12 shows a typical process of TOF measurement.

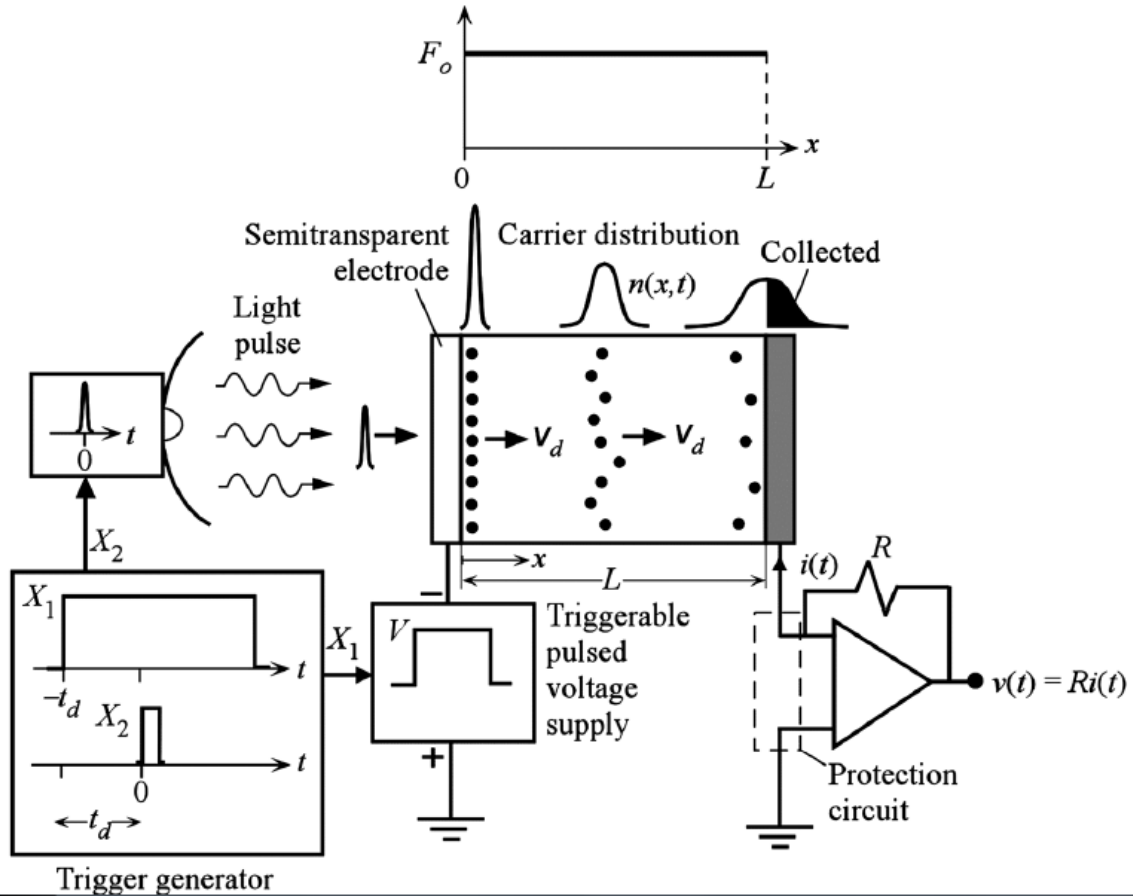


Figure 2.12 A typical schematic of TOF measurement. The small signal assumption is made so that the carrier's drift velocity remains constant. After Kasap et al. [9]

Once the electrical field is assumed to be uniform through the sample, a deeper understanding of the carrier transient current of TOF measurement can be achieved. The photocurrent produced by the drift of the charge sheet through the sample can be found using Ramo's theorem. [50] One can consider a carrier with charge q travels through the sample under the applied field E . The applied field E is equal to V/L , which is the uniform through the sample. The drift velocity of the carrier can be expressed as

$$v = \mu E = \frac{\mu V}{L} \quad (2.17)$$

where μ is the mobility of the carrier. The drift velocity of the carrier through the sample remains constant under the small signal condition. The transient time for the carrier to cross

the sample is then expressed as

$$t_T = \frac{L}{v} \quad (2.18)$$

The transient time is the time of carrier travels from the surface of the sample to the bottom electrode of the sample. Knowing the above information, one can write down the transient current for a single carrier drift through the sample with thickness L under applied voltage V .

$$i_{ph} = \begin{cases} \frac{qv(t)}{L} & 0 < t < t_T \\ 0 & \text{else} \end{cases} \quad (2.19)$$

This equation can be applied to the TOF experiment as long as the small signal condition is met. This equation for a single carrier can be expanded to a real case by applying the total number of injected carriers in the TOF experiment. [21]

$$Q = epwA \quad (2.20)$$

where p is the concentration of injected carriers, w is the width of the charge sheet and A is the area of the charge sheet. Since the small signal assumption is valid throughout the TOF experiments, the drift velocity of carriers remains constant during the transient process. In addition, it is more convenient to use the transient time to replace the drift velocity of the sample

$$i_{ph}(t) = \begin{cases} \frac{epwAv(t)}{L} = \frac{epwA}{L} \times \frac{L}{t_T} = \frac{epwA}{t_T} & 0 < t < t_T \\ 0 & \text{else} \end{cases} \quad (2.21)$$

A small signal AC analysis can be applied for the TOF experiment. [3] The whole system can be treated as a combination of capacitor and resistor. C_s is the combination of the sample capacitance and any parasitic in the external electronics. The photocurrent provides a voltage by passing through a combination of the C_s and the external resistor; R . Laplace transform can be applied for further studying. The voltage and current relation can be expressed as

$$V(s) = \frac{R}{sRC_s + 1} I_{ph}(s) \quad (2.22)$$

where $V(s)$ is the Laplace transformation of the voltage signal and $I_{ph}(s)$ is the Laplace transformation of the photocurrent. This relation can be used to study the photocurrent and voltage signal by taking the inverse Laplace transformation. Based on the relation among

resistance, capacitance and transient T, two different solutions exist.

The first one is called the I-mode signal because the magnitude of the received signal is directly proportional to the photocurrent. [3] This solution comes out when $RC_s \ll t_T$.

$$v(t) = \begin{cases} Ri(t) & 0 < t < t_T \\ 0 & \text{else} \end{cases} \quad (2.23)$$

An ideal I-mode signal looks similar to a square wave pulse; it rises sharply at the start and remains constant as the photo-induced carriers drift through the sample, then drops back to zero. However, the real case in amorphous solid based semiconductors is more complicated than this. In amorphous solid based semiconductors, there are a large amount of localized states within the mobility gap of the semiconductors. Charge carriers will be trapped in these localized states and removed from the transportation band during the transient process. This will result in a decrease of number of mobile charge carriers. Since the photocurrent is proportional to the number of charge carriers or the concentration, the photocurrent is about to decrease with respect to time.

Therefore, taking these localized states into consideration should carry out a revised solution. [3] First, one can assume a set of traps at a discrete energy level in the mobility gap with a mean trapping time τ . Once these traps, which are some localized states, trapped the carriers, the time it took for carriers to be released would be much longer than the transient time. From previous research, it has already shown that the number of carriers in the charge sheet will decay exponentially as they travel through the sample, and are captured by the traps. Therefore, an exponential decay term could be added to previous equation

$$i_{ph} = \frac{epwA}{t_T} \exp\left(-\frac{t}{\tau}\right) \quad (2.24)$$

The I-mode signal can be then modified as

$$v(t) = \begin{cases} Ri(t)\exp(-t/\tau) & 0 < t < t_T \\ 0 & \text{else} \end{cases} \quad (2.25)$$

Another mode is known as the V-mode signal and it is the solution when $RC_s \gg t_T$. This signal begins at zero and will increase linearly as the carriers travel through the sample. After the carriers reach the collection electrode, the signal will flatten and remain constant at a value proportional to the total number of injected charges.

$$v(t) = \frac{1}{C_s} \int_0^t i_{ph}(\alpha) d\alpha \quad (2.26)$$

without considering any localized states. If the localized states are taken into account, the voltage signal is given by [51]

$$v(t) \begin{cases} \frac{epwA\tau}{C_s t_T} \left(1 - \exp\left(-\frac{t}{\tau}\right)\right) & 0 < t < t_T \\ \frac{epwA\tau}{C_s t_T} \left(1 - \exp\left(-\frac{t_T}{\tau}\right)\right) & t > t_T \end{cases} \quad (2.27)$$

Since V-mode is not used in this research, there are no further explanation and discussion for it. A typical signal shape of I-mode TOF and V-mode TOF are shown in Figure 2.13.

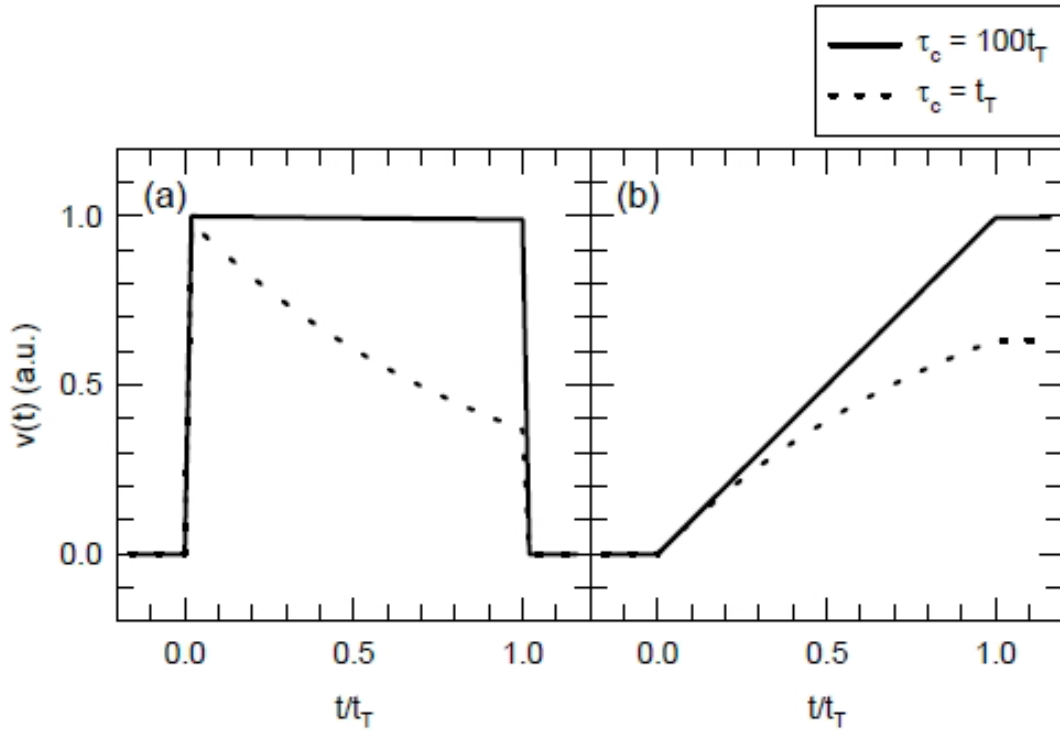


Figure 2.13 Simulated TOF signal. a) I-mode: the solid line is the ideal case while dot is the case with defects. b) V-mode: the solid line is the ideal case while dot is the case with defects. After Fogal [3].

2.3.3 The Interrupted-Field Time-of-Flight Technique

The interrupted-field time-of-flight technique is a method to determine the carrier-trapping lifetime in high resistivity materials. It is based on the Time-of-Flight technique described in the previous section. For TOF measurement, the applied field assists the carriers

to drift through the sample. The carriers initially drift through the sample under the applied field E . After time t_1 , the applied field is switched off. The applied field will be switched back on after time t_i then the carriers are going to drift again under the applied field. This is the only difference between TOF measurement and IFTOF measurement. Since the carriers are going to be trapped by traps when the field is off, one can use the information from the reduction of photocurrent to analysis the carrier-trapping lifetime.

The IFTOF technique measures the deep trapping lifetime of the carriers by interrupting the drift of the carriers and allowing them to interact with the deep traps in the semiconductor. As mentioned above, the applied field is switched off after t_1 . As soon as the applied field is off, the drift of carriers is halted, which result in the zero measurement of the photocurrent. The carriers remain stopped at this position. Note that carriers will not completely stop at the position. Instead, they would diffuse in all direction for a small region but they remain stop at the position averagely. The carriers would interact with traps during the stop. Once the applied field is resumed, the rest of carriers will begin to drift again. The photocurrent is going to drop because of the loss of charge carriers. Since the carriers are moving at a constant speed inside the sample, the drop of the magnitude of the photocurrent is proportional to the number of the loss of the charge carriers. If these traps in the mobility gap can be characterized by a carrier-trapping lifetime τ_c , then the drop of photocurrent can be expressed as. [21]

$$\frac{i(t_2)}{i(t_1)} = \exp\left(-\frac{t_i}{\tau_c}\right) \quad (2.28)$$

The drop of the photocurrent is obtained during IFTOF measurement. It is then used to obtain the carrier-trapping lifetime. The carrier-trapping lifetime is then given as

$$\tau_c = \frac{t_i}{\ln(i(t_1)/i(t_2))} \quad (2.29)$$

The interruption time t_i can be adjusted and normally it should be long enough for carriers to interact with traps. If the interruption time is too long then the recovered photocurrent will be too small to measure. There are two ways to obtain the carrier-trapping lifetime through the signal loss during the IFTOF measurement. One can choose an interruption time t and perform an IFTOF measurement. Then the carrier-trapping lifetime

can be obtained through Equation 2.29. Another way is to use set of different interruption time and perform multiple IFTOF measurements. Then one can plot $i(t_1)/i(t_2)$ verse t_i on a semi-logarithmic plot and use the slope of the plot to obtain the carrier-trapping lifetime. The advantage for the second method is that it eliminates the time delay due to the actual circuit. The interruption time might be slight longer than it should be in the actual experiments. Therefore, if the circuit designed for the experiment is not sensitive enough, then the carrier-trapping lifetime obtained from the first method will be larger than its real carrier-trapping lifetime. Normally the interruption time for the carrier is slightly longer than its transient time, which can be acquired by a TOF measurement. A typical waveform of IFTOF measurement is shown in Figure 2.14.

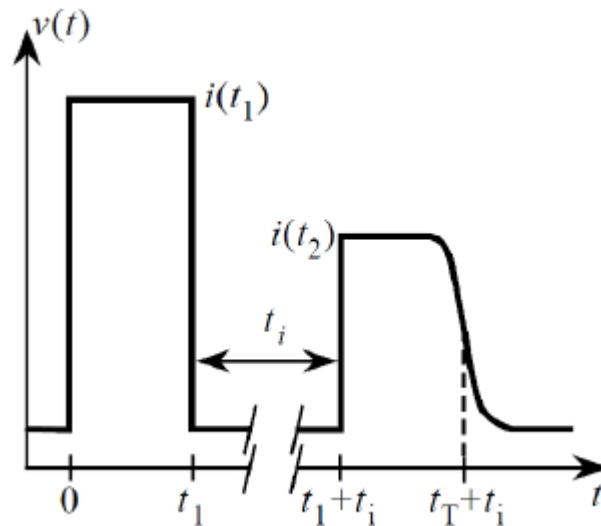


Figure 2.14 A typical waveform of IFTOF measurement. The waveform is a very ideal case with no trapping process during the transient. The photocurrent before interruption is $i(t_1)$ and the photocurrent after the interruption is $i(t_2)$. The interruption time is t_i . After Fogal [3]

2.4 Transient Trap Limited Theories

The previous sections detailed the principles of the TOF and IFTOF experiments. However, as mentioned in the previous section, the amorphous solid based semiconductor is very complicated. In the previous TOF measurement section, localized states have been mentioned and an exponential decay term has been added to the photocurrent expression.

These localized states served as traps and interference the analysis based on the ideal model. Therefore, it is important to have a deeper understanding of the effects of these localized states. These traps can be analyzed in three different distributions.

2.4.1 Monoenergetic Trap Level

The first type starts with assuming the localized states have a single energy distribution in the mobility gap. These localized states as mentioned before serve as traps for carriers. In order to analysis how these traps affect the carrier transportation, one can first assume that carriers travel in the form of infinitesimal slice. The number of free carriers in the slice is due to the current flowing through the slice, as well as the thermal release of trapped carriers within the slice. The rate of change in the number of carriers in the slice can be then obtained [3]

$$\frac{\partial p(x,t)}{\partial t} = \frac{1}{q} \frac{\partial J(x,t)}{\partial x} - \frac{\partial p_t(x,t)}{\partial x} \quad (2.30)$$

where $p(x,t)$ is the concentration of free carriers, $J(x,t)$ is the net current density flowing, q is the carrier charge and $p_t(x,t)$ is the concentration of trapped carriers in the slice. This continuous equation is only valid if the slice thickness is very small.

The net current density consists of the conduction current and the diffusion current. The drift of carriers under applied field will induce the conduction current. As discussed before, it can be given as [3]

$$J_c(x,t) = qp(x,t)v(x,t) = qp(x,t)\mu E(x,t) \quad (2.31)$$

where μ is the carrier mobility and q is the carrier charge. Carrier charge is $-e$ for the hole and e for the electron. In addition, the diffusion current is caused by spatial variations in the concentration of charge carriers. It can be given as. [3]

$$J_D(x,t) = qD \frac{\partial p(x,t)}{\partial x} \quad (2.32)$$

where D is the diffusion coefficient. The total current density can then be written as

$$J(x,t) = J_c(x,t) + J_D(x,t) = qD \frac{\partial p(x,t)}{\partial x} + qp(x,t)\mu E(x,t) \quad (2.33)$$

Then the continuity equation for the carrier transportation can be rewritten as

$$\frac{\partial p(x,t)}{\partial t} = D \frac{\partial^2 p(x,t)}{\partial x^2} - \frac{\partial p_t(x,t)}{\partial x} + \mu E(x,t) \frac{\partial p(x,t)}{\partial x} + \mu p(x,t) \frac{\partial E(x,t)}{\partial x} \quad (2.34)$$

Since $p_t(x,t)$ represent the trapped carrier density, $\frac{\partial p_t(x,t)}{\partial x}$ is then the change rate of trapped carriers. The change rate of trapped carriers is determined by the carrier-trapping rate and carrier-releasing rate. [3]

$$\frac{\partial p_t(x,t)}{\partial t} = \frac{p(x,t)}{\tau_c} - \frac{p_t(x,t)}{\tau_r} \quad (2.35)$$

where τ_c is the capture time or trapping time and τ_r is the release time. The concentration of trapped carriers increases if more carriers are trapped and decreases if more trapped carriers are released.

By solving the rate equation and the continuity equation for the carrier, one can obtain an expression for the carrier density in the charge packet. Though the continuity equation looks very complicated, there are some simplifications could be applied to solve the equation. One of the main assumptions that has been made for TOF/IFTOF measurement is small signal condition. Under the small signal condition, the internal field inside the semiconductor is independent of time and position. Therefore, the applied field $E(x,t)$ is actually equal to a constant field. The diffusion portion of the current density can be neglected based on the assumption the diffusion of the charge carrier packet is negligible compared with the drift. The experimental observation has shown that when applied field is off the photocurrent is extremely small compared with that when applied field is on. This experimental observation accords with the assumption. Based on the previous section of TOF measurement, boundary conditions and initial states can be obtained to help solve the continuity equation for carrier density. There are no carriers at $t < 0$. The carriers are all excited by light pulse at $t = 0$. Since the duration of light pulse is extremely small, a delta function can be used to describe the carrier density at $t = 0$

$$p(x,0) = P\delta(x,0) \quad (2.36)$$

where P is the total number of generated carriers. In addition, the number of trapped carriers should remain zero at $t=0$. Carriers should be confined inside the sample; therefore, for both carriers and trapped carriers

$$p(x, t) = p_t(x, t) = 0 \quad x > L \quad (2.37)$$

Laplace transformation is applied. The solution is obtained based on boundary condition. It is given as [52][53]

$$p(x, t) = \frac{P}{\mu E} \exp\left(-\frac{z}{\tau_c}\right) \delta(t - z) + \frac{P}{\mu E} \exp\left(-\frac{z}{\tau_c} - \frac{t-z}{\tau_r}\right) \frac{\xi}{2} \frac{I(\xi)}{(t-z)} U(t - z) \quad (2.38)$$

where E is the applied field, z is the time it takes for carrier to reach distance x , $z = x/\mu E$, $I(\xi)$ is the first order hyperbolic Bessel function and $U(x)$ is the unit step function.

$$\xi = \frac{2\sqrt{\frac{\tau_c z(t-z)}{\tau_r}}}{\tau_c} \quad (2.39)$$

The equation contains two components. The first one represents the charge carriers remaining in the injected packet as it drifts across the sample. These carriers are not delayed by trapping and release as they travel through the sample, but do decrease exponentially. The second term represents carriers that have experienced at least one time trapping and releasing process. It represents the carriers have been trapped and released at a later time, t , into the transport band. These charges contribute to the photocurrent for times longer than the transient time.

Integrating the carrier density equation can solve the I-mode transient current response in a medium with a monoenergetic distribution of traps. However, due to the complexity of the carrier density equation, it is not easy to apply the equation to study the transient response. In order to simplify the analysis, two limiting cases are usually considered. Usually they are distinguished by low field case and high field case. Based on the setup of the TOF measurement either one of them can be used to predict the carrier transient response.

The low field case assumes that the transit time of the carriers is much longer than the carrier capture time. Additionally this transient time is in the same order of releasing time.

$$\tau_c \ll \frac{L}{\mu E} \approx \tau_r \quad (2.40)$$

This indicates that carriers are immediately been trapped and they are not to be released during the transient process. Since the trapped carriers have no contribution to the transient current, the second term in the equation can be neglected. Based on the conservation of total carriers and rate equation of the carriers, the number of free carriers inside the sample can be

expressed as the total number of injected carriers. [54]

$$P = P_0 \frac{\tau_c}{\tau_c + \tau_r} \quad (2.41)$$

The photocurrent can be further expressed as

$$i_{ph} = \frac{epE\mu}{L} \quad (2.42)$$

where

$$\mu = \frac{\tau_c}{\tau_c + \tau_r} \mu_0 \quad (2.43)$$

where μ_0 is the carrier mobility in a trap-free environment. The expression is very close to the ideal case of TOF. The only difference is that the carrier mobility becomes smaller due to traps. This mechanism can be referred as shallow trap controlled transportation.

Another case is the high field case, of which the applied field is large. The capture time in this case is much larger than the transient time, which means that few carriers are trapped during the transient process. The photocurrent is divided into two different time regimes. One is the transient time regime, which means carriers have reached the bottom electrode yet. Marini et al give an expression. [55]

$$i_{ph}(t) = \frac{eP_0}{t_T} \left[\frac{\tau_c}{\tau_c + \tau_r} + \frac{\tau_c}{\tau_c + \tau_r} \exp\left(-\frac{\tau_c + \tau_r}{\tau_c \tau_r} t\right) \right] \quad (2.44)$$

Though the trapping time is much larger than the transient, there are still portion of carriers to be trapped during the transient. They will be released subsequently and contribute to the photocurrent after transient time. This can be expressed as [52]

$$i_{ph} = \frac{eP_0}{2} (t_T / \tau_c \tau_r) \exp(-t / \tau_r) \quad (2.45)$$

These two equations indicate that the transient photocurrent will initially decay exponentially until carriers reach the bottom electrodes. At that time a step down in magnitude will occur, followed by another exponential decay to zero as the trapped carriers are released and collected.

2.4.2 Multiple Trap Distribution

The previous section only considers one energy state traps; however, in reality, the

localized states would have more than one energy state. The easiest model is a binary trap distribution, which involves two different traps with different capture time and release time. A simplification is made in order to study the problem easier. The concentration of injected carriers is much less than the concentration of traps at each energy state. Since the concentration of carriers does not exceed the concentration of the trap, carriers would have chance to be captured by either of traps. It is also assumed that only trapping free carriers contribute to the number of carriers trapped at a particular level. In the binary trap distribution case, carriers are assumed to be trapped only once during the transient. However, in the multiple traps distribution, the carriers are trapped and released by different energy states of traps multiple times.

Blakney and Grunwald give the transient current for a binary traps distribution. [56] Essentially it can be treated as a combination of two individual monoenergetic trap distribution with capturing time τ_{c1}, τ_{c2} and releasing time τ_{r1}, τ_{r2} respectively.

$$j(t) = A\exp(-at) + B\exp(-bt) + j \quad (2.46)$$

where

$$a + b = \frac{1 + \frac{\tau_{c1}}{\tau_{r1}}}{\tau_{c1}} + \frac{1 + \frac{\tau_{c2}}{\tau_{r2}}}{\tau_{c2}} \quad (2.47)$$

$$ab = \frac{\left[\frac{\tau_{c1} + \tau_{c2}}{\tau_{r1} + \tau_{r2}} \left(1 + \frac{\tau_{c1}}{\tau_{r1}} \right) \right]}{\tau_{c1}\tau_{c2}} \quad (2.48)$$

$$aA + bB = \frac{j_0}{\tau_{c1}} + \frac{j_0}{\tau_{c2}} \quad (2.49)$$

$$A + B + j = j_0 \quad (2.50)$$

where j is the steady state current. If the binary trap distribution happens to be a combination of shallow and deep traps, then the equation can be simplified by assuming of the trap releasing time is extremely large.

$$j(t) = A\exp\left(-\frac{t}{\tau_{c1}}\right) + B\exp\left(-\frac{\tau_{c1}t}{\tau_{c2}\tau_{r1}}\right) \quad (2.51)$$

The first term indicates a spike that will decay exponentially until the carriers reach equilibrium with the shallower traps. [57][58] The second term is a slow exponential decay.

For multiple trap distribution, a photocurrent solution can still be obtained through solving the continuity equation and considering a combination of multiple monoenergetic trap distribution. The Laplace transformation of the photocurrent solution is given as. [9]

$$i(s) = \frac{\frac{en}{t_0}(1-\exp(-a(s)t_0))}{a(s)} \quad (2.52)$$

where

$$a(s) = \frac{s}{t_0} \left(t_0 + \sum \frac{c_i t_0}{s+r_i} \right) \quad (2.53)$$

where t_0 is the transient time for carriers in a trap free sample, c_i is the capture rate for i level energy states and r_i is the release rate for i level energy states. Figure 2.15 shows the multiple trapping transportation process.

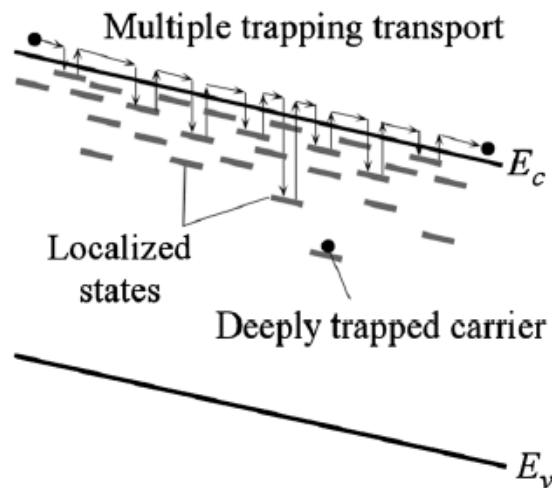


Figure 2.15 A schematic of carrier transportation under multiple traps distribution condition. Carriers can be trapped and released multiple times by different traps. However, carriers are not released in a short time once deep traps trap them. After Kasap et al. [9]

2.5 Capacitance

The capacitance shows the ability the material to store electric charges under a certain voltage. It is an essential concept for electronics since capacitor is normally recognized as one of the three basic element of electric circuit. Every material that could be electrical charged

has capacitance for itself. Though there are lot classifications of capacitance in different environment, in this section, only the basic capacitance is considered. The capacitance is defined as

$$C = \frac{\dot{Q}}{\dot{V}} \quad (2.51)$$

where C is the capacitance, \dot{Q} is the change rate of the stored charges or it normally refers to the current in the circuit, \dot{V} is the change rate of the voltage. Since the amorphous selenium samples that are used in this research can be simplified as parallel plates capacitors, it is more efficient to consider the capacitance of parallel plates capacitors. The general capacitance of a parallel capacitor is given as

$$C = \frac{\epsilon_r \epsilon_0 A}{L} \quad (2.52)$$

where A is the area of the plate, L is the distance between two plates, ϵ_0 is the electric permittivity in the vacuum and it is a constant, and ϵ_r is the relative permittivity for the dielectric material. In addition, the relative permittivity can be further related to electric susceptibility, which can be given as

$$\epsilon_r = 1 + \chi_e \quad (2.53)$$

where χ_e is the electrical susceptibility of the dielectric material. In other words, the relative permittivity is related to the induced polarization. In the concept of molecular polarization, one can further write electric susceptibility as [59]

$$\chi_e = \frac{N\gamma_{mol}}{1 - \frac{1}{3}N\gamma_{mol}} \quad (2.54)$$

where N is the total number of dipoles, and γ_{mol} is defined as molecular polarizability. It is the average molecular dipole moment to ϵ_0 times the applied field at the molecular.

2.6 Summary

In this chapter, the electronic and optical properties of amorphous selenium are introduced. The amorphous selenium shares a lot of common properties with other amorphous solids. Since amorphous selenium is not a crystalline material, its properties are more complicated and hard to observe. The electronic properties are determined by the atomic

bonding arrangement of selenium atoms. The single bonding configuration of selenium atoms takes various forms and they can further form defect structures for amorphous selenium based semiconductors. These defects largely affect the transportation of electronic carriers in the amorphous selenium based semiconductors. The density of states models, which are developed to enhance the understanding the carrier transportation, are reviewed. Since the nature of amorphous solids is complicated, there is no absolute right density of state model for amorphous selenium. Several models are introduced including some recent simulation models. Each model has provided some useful information about the distribution of defects in the mobility gap of the amorphous selenium based semiconductors. The optical properties of amorphous selenium are also introduced. Since the main research goal is to study the X-ray induced changes in electronic properties of amorphous selenium, the X-ray generation and absorption is introduced as well. A theoretical estimation method of X-ray energy absorbed in the material is introduced, which is used later in the experiment to estimate the X-ray dose deposited in the samples.

The theoretical base for the measurement technique is introduced in this chapter as well. Time of flight and interrupted field time of flight are the techniques used in the later experiments. These techniques are developed in order to measure the electronic properties of amorphous selenium. Time of flight measurement provides a method to obtain the carrier mobility of amorphous selenium. Interrupted field time of flight measurement provides a method to obtain the carrier-trapping lifetime of amorphous selenium. The sensitivity of X-ray detectors can be then acquired by combining the information from these two parameters. The small signal condition is the prefix for both TOF and IFTOF measurements, which ensures the uniform distribution of the internal field during the measurement. Both measurements measure the photocurrent induced by the drift of carriers. The interruption of the applied field during the IFTOF measurement provides the information of carrier-trapping lifetime. Since the density of states in the mobility gap is very complicated, several modified carrier transit model for TOF/IFTOF measurements are also discussed. The transportation of carriers due to different trap models is discussed in detail. The shallow traps are the main governing elements for carrier transportation in the amorphous selenium based

semiconductors. The models include monogenetic trap level and multiple trapping processes.

The concept of the capacitance is briefly introduced in this chapter as well. Though it is not the main research goal for the experiment, the capacitance measurement is included in the later chapters. The changes of capacitance in the experiments are caused by generation of dipoles in the bulk of amorphous selenium.

3. Experimental Procedure

3.1 Sample Preparation

Vacuum deposited amorphous selenium (a-Se) films (layers) are used as test samples for the experiments. The samples are chosen to be a-Se:0.3% As: 5ppm Cl films with a thickness of 150 μm . The arsenic alloying is used to stabilize the a-Se films against crystallization. Since alloying with arsenic undermines the hole transport (hole-trapping lifetime becomes shortened), the alloyed material chlorine is doped in order to improve the hole transport. A standard vacuum deposition technique is used to fabricate the samples. Cleaned corning glass substrates coated with a layer of aluminum are used as substrates for the samples. The aluminum serves as the electrode for the TOF/IFTOF measurements. The aluminum layer is thin but has sufficient conductance to serve as the rear electrode. Some of the samples do not have this aluminum layer; instead, they use a thin layer of ITO as the electrode. Most samples use the aluminum layer. The substrates are put into an NRC 3117 stainless steel vacuum coater system, which is shown in Figure 3.1. Vacuum deposition of samples begins with selenium pellets being evaporated inside an evacuated chamber. The selenium vapors then condense onto the substrate, which is held just above the glass transition temperature of a-Se. This allows the selenium atoms to rearrange themselves into a structurally relaxed amorphous state as they condense. Figure 3.2 shows a schematic diagram of what are inside the NRC 3117 stainless steel vacuum coating system and how it works.

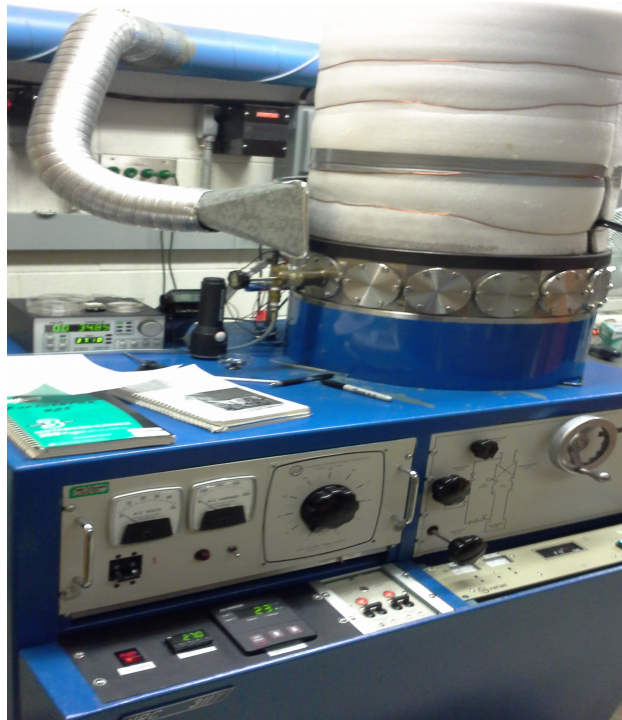


Figure 3.1 NRC 3117 stainless steel vacuum coater system

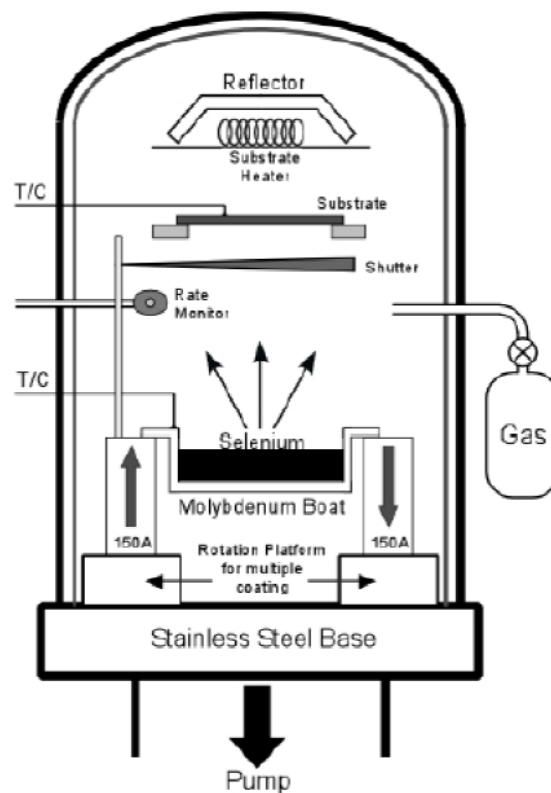


Figure 3.2 Schematic diagram of the NRC 3117 vacuum deposition system used to make the samples in this study. After Fogal [3]

As shown in Figure 3.2, the selenium pellets are loaded into a molybdenum boat and evaporated by running a large current through the boat. The boat is heated to about 250 °C by passing a 100 – 150 A AC current. The chamber is evacuated to a base pressure of $\sim 10^{-6}$ Torr. The substrate heater keeps the glass substrate around 60 °C, just above the glass transition temperature of a-Se. The temperatures of both the boat and substrate are controlled through temperature controllers. The temperature of the boat governs the rate of evaporation and the temperature of the substrate largely affects the condition of the sample. A mechanical shutter covers the substrate until the evaporation has reached a steady rate. At that time the shutter is opened, the selenium begins to condense onto the substrate. A digital quartz crystal rate monitor is used to monitor the evaporation rate of source selenium material. After the desired thickness is reached, the shutter is closed. The current will not be switched off immediately. It will be switched off when the evaporation rate of selenium becomes a small. The samples are kept in the chamber for 24 hours before they are taken out.

Since the research goal is to examine the electronic properties of the a-Se, electrodes are required on the samples. A layer of aluminum on the substrate has been served as the bottom electrode. Gold contact will be deposited on the surface of selenium samples. A Hummer VI sputtering system was used to deposit the top gold contact and it is shown in Figure 3.3.



Figure 3.3 Hummer VI sputtering system

To begin the sputtering process, a mask with a circular opening 0.5 cm in diameter covers the sample. The chamber is pumped down to a pressure of 110 m Torr and filled with Argon gas. When a high voltage is applied between the anode and cathode within the chamber, the argon gas ionizes. These positively charged argon ions begin to collide with the negatively charged gold target at the top of the chamber and dislodge gold particles. These free gold particles evenly cover the exposed area on the sample surface. The sputtered gold films have an edge-to-edge resistance of 100 – 200 Ω , and were sufficiently thin to allow light to pass through. Figure 3.4 shows how the contact is deposited on the sample. Figure 3.5 shows the actual appearance of the a-Se film which is used in the experiment.

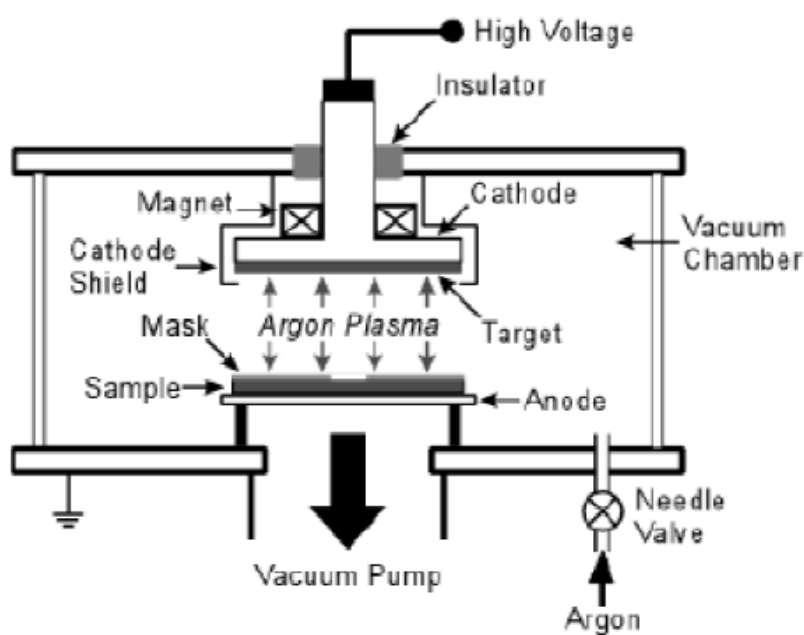


Figure 3.4 Schematic diagram of the Hummer VI sputtering system used to generate contacts on the a-Se samples. After Fogal[3]



Figure 3.5 A typical 150um thick a-Se:0.3%As:5ppm Cl sample.

3.2 X-ray dose measurement

3.2.1 X-ray Tube System

Gendex GX-1000 X-ray tube system is used as the X-ray source for the experiments. Its peak voltage can be adjusted from 50 kVp up to 100- kVp. Its filament current can be set to be either 10 mA or 15 mA. It has a 2.5mm aluminum half-value layer. The X-ray tube is a tungsten target X-ray tube that produces a wide range of x-ray energy spectrum. The X-ray beam pulses at 1/60 of a second impulse due to the half-wave rectifier used by the system and a 60 Hz power supply. The system has a timer, which can generate a succession of pulses for a duration from (1/12)th to 5 s. Figure 3.6 shows a photograph the X-ray system along with the protection steel chamber.



Figure 3.6 Gendex GX-1000 X-ray system and steel chamber protection

There is limited irradiation duration due to the overheating of the X-ray tube. The maximum

working cycle of the X-ray tube within 5 minutes is listed in Table 3.1.

Table 3.1 Working cycle of the X-ray tube [60]

kVp	10mA	15mA
50-70	30	20
80	26	17.5
90	23	15.5
100	21	N/A

A steel chamber was used to protect users from X-ray irradiation. The steel chamber was manufactured by X-ray Products Corp of Pico Rivera California; the model number of the unit is A9002-16

3.2.2 X-ray Dose Measurement System

The X-ray dose measurement system consists of two parts. One part is the dosimeter system for X-ray exposure measurement and the other is theoretical dose estimation program. A Keithley 35050 Ion Chamber along with the Keithley 35050 Dosimeter measures the actual X-ray exposure, in the units of Rontgens (R), irradiated from X-ray tube. A digital voltmeter was attached to the Keithley 35050 Dosimeter in order to obtain the read-out from the dosimeter and convert the voltage reading to exposure in Roentgens. The ion chamber is 1.25 cm thick and the total volume is 15 cm³. The dosimeter system and the ion chamber are shown in Figure 3.7.



Figure 3.7 Keithley 35050 Dosimeter and Ion chamber for X-ray exposure measurement.

The voltage readout from the multimeter can be converted into dose by applying the conversion factor for this particular Keithley model, i.e. Keithley 35050 Ion Chamber [21]

$$V(\text{Volts}) \times 0.743 \left(\frac{\text{Rontgen}}{\text{Volts}} \right) = \text{Dose}(\text{Rontgen}) \quad (3.1)$$

Knowing the dose deposited into the ion chamber and the thickness of the sample, one can use program dose.py to calculate the dose deposited into the sample. The dose.py is written in Python 2.7 and it follows the methodology for the theoretical calculation of X-ray dose described in the theory part (Chapter 2). The dose.py can be run under terminal in Mac OS system or in command terminal in Windows system. The program asks user to provide some inputs in order to calculate the dose. The peak voltage of the X-ray tube, sample material composition, position or thickness of the sample, the exposure obtained from dosimeter and the density of the sample material are needed in order to calculate the dose. Figure 3.8 is a screenshot of an example of deposited dose calculation for a typical a-Se sample in the sample by dose.py. The code of dose.py is attached in Appendix A.

```
C:\Users\mac>cd C:\p\python27

C:\p\Python27>python
Python 2.7.3 (default, Apr 10 2012, 23:31:26) [MSC v.1500 32 bit (Intel)] on win
32
Type "help", "copyright", "credits" or "license" for more information.
>>> import dose
>>> dose.dose()
Enter the peak voltage(kvp) of the X-ray tube:75
Enter the material for dose calculation:Se
Enter the position(cm) of the sample for dose calculation, if it is for average
dose please enter thickness+L(eg. 0.015L for average dose over 0.015cm sample):0
.004
Enter the read out from ionization chamber(R):0.335
Enter the density of the sample(g/cm^3):4.3
0.1868955776749727
>>>
```

Figure 3.8. An example of dose calculation by dose.py is shown above. The sample is selenium and its density is 4.3 g/cm³. The peak voltage of X-ray tube is 75 kVp and the exposure obtained from the dosimeter is 0.335 R. The dose is calculated for 40 μm beneath the surface. The result is in the units of Gy.

3.2.3 X-ray Dose Rate Adjustment

X-ray dose rate depends on two factors in the experiment. One is the output dose rate from the X-ray tube and other is the absorbed dose rate in the sample. The output dose rate of the X-ray tube can be adjusted through using different filament currents in the X-ray tube. At

the sample peak voltage, the output dose rate of X-ray tube is proportional to the filament current. The Gendex GX-1000 X-ray tube system provides two different filament current options. One is 10mA and other is 15mA. The dose rate for 15 mA is 1.5 times larger than that for 10 mA. In addition to the adjustment of the filament current in the X-ray tube itself, one can change the distance between the sample and X-ray tube. Since the X-ray energy that reaches the sample decreases with distance, the sample position is adjusted to achieve different dose rates. An adjustable sample holder is used to adjust the distance from sample to the X-ray tube. The setup is shown in Figure 3.9.

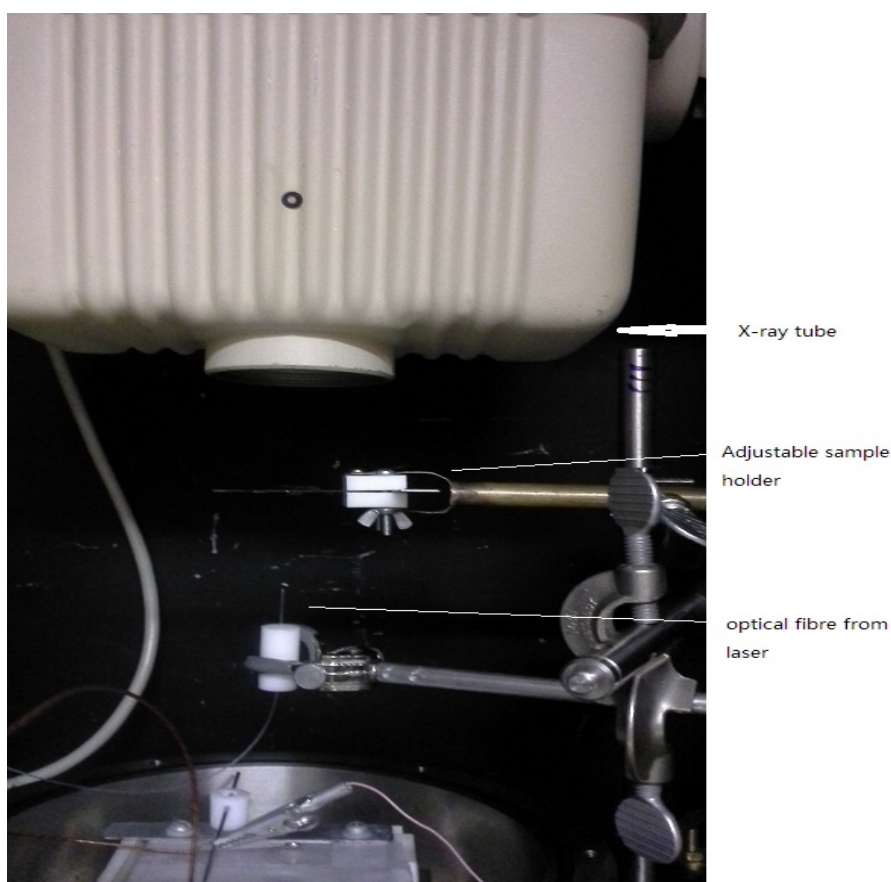


Figure 3.9. A movable white sample holder holds the a-Se film. The film can be moved closer to X-ray tube or further away. The laser optical fiber is placed beneath in order to generate injected carriers at the surface of the sample.

3.3 Carrier-Trapping Lifetime Measurement and IFTOF Experiments

3.3.1 Overview

The carrier-trapping lifetime is measured by the IFTOF method. A schematic diagram

of how the IFTOF measurement works is shown in Figure 3.11 below. A bias voltage $V(t)$ is applied onto the sample shortly before $t = 0$. The laser is triggered at $t = 0$ and photons are absorbed very near surface of the sample. The bias voltage separates the electrons and holes generated by the photons. Depending on the bias voltage, one type of carrier will be collected by the electrodes immediately. The other type of carrier will drift through the sample under the applied field. The bias voltage is normally switched on 500 μs before the laser is triggered.

The drift of the carriers under the bias field generates a current $i(t)$ which is monitored by the digital scope. In most cases, the response collected from the drift of the carriers is the voltage $V(t)$ instead of current $i(t)$; the latter is passed through a sampling resistor and the voltage $V(t)$ is across the sampling resistor. Since the drift current due to carriers is relatively small, it requires a very sensitive and stable experiment setup. The drift current for an a-Se sample under $1 \text{ V}/\mu\text{m}$ field is typically on the order of $10 \mu\text{A}$. It is more convenient to measure the voltage across a sampling resistor instead of the current passing through the sample. The bias voltage is switched off at t_1 and back on at t_2 . Due to the protection circuit in the amplifier, a small delay occurs when the high voltage is switched back. The high voltage is switched back at t_2 , while the scope begins to receive signal at $t_2 + \Delta t$. The time delay Δt is normally 5 to 20 μs depending on the resistance value set in the amplifier. The high voltage is switched off once all the carriers reach the collecting electrode. A typical signal response of the transient voltage during IFTOF measurement is shown in Figure 3.11.

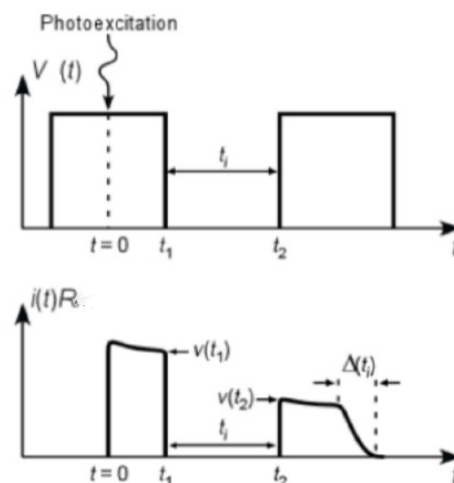


Figure.3.10. A schematic process of IFTOF measurement is shown above. The above diagram shows how bias voltage is applied and interrupted. The diagram shows the corresponding photocurrent. Adapted from Fogal [3].

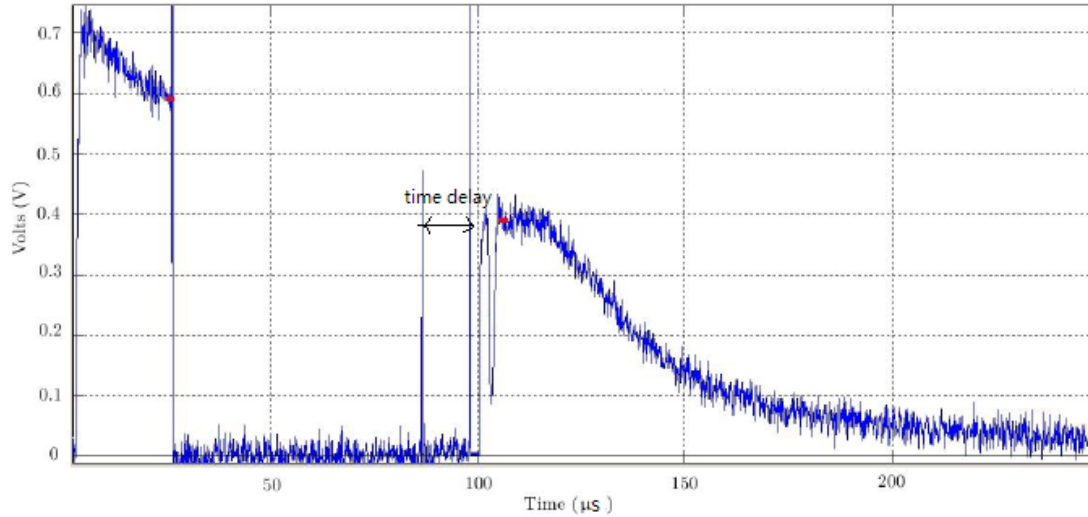


Figure 3.11 A typical IFTOF signal. The transient voltage drops to zero when the applied field is switched off. When the applied field is switched on, the voltage response recovers. The signal experiences a magnitude drop due to deep trapping. A significant signal delay can be observed when high voltage is switched back. The protection circuit in the amplifier circuit causes this delay. Adapted from Walornjy [21]

The voltage response (across the sampling resistor so that $V(t) = Ri(t)$) before the interruption $V(t_1)$ and the voltage response after the interruption $V(t_2)$ are captured from the IFTOF measurement signal. Since the interruption time t_i is known, one can calculate the carrier-trapping lifetime based on Equation (2.29) in Chapter 2. For instance, in Figure 3.11, the voltage before the interruption is 0.60 volts, and the voltage after the interruption is about 0.40 volts. The interruption time is about 75 μs . The carrier-trapping lifetime is then given by

$$\tau = \frac{t_i}{-\ln(V(t_2)/V(t_1))} = \frac{75}{-\ln(0.4/0.6)} \mu\text{s} = 185 \mu\text{s} \quad (3.2)$$

This carrier-trapping lifetime might be longer than this because of the inherent delay in the IFTOF measurement. The interruption time is set to be 60 μs and the field is back after a 60 μs interruption. However, the system does not immediately begin to monitor the signal after the field is back. It begins to collect the signal 15 μs later due to the protection circuit. Therefore, the photocurrent drop now is not completely caused by the deep trapping process during interruption; and the carrier-trapping lifetime obtained is not the real carrier-trapping lifetime. As suggested in the Chapter 2, in order to obtain the real carrier-trapping lifetime, one can use a set of different interruption times. For each interruption time, the voltage drop

is different. If the ratio of voltage drops and the interruption time are plotted on a semi-logarithmic plot, the slope will be the reciprocal of the real carrier-trapping lifetime. This multiple interruption time measurement depends on the actual experiments. If the delay time is very short or the results from two methods are very close, then there is no need to do multiple IFTOF measurements for a single lifetime measurement. Therefore, it is necessary to do a test on the actual experimental system with an actual sample before extensive lifetime measurements especially in monitoring the effects of x-ray irradiation on the lifetime; and its recovery. The Figure 3.12 shows a typical case that uses semi-logarithm to obtain the carrier-trapping lifetime.

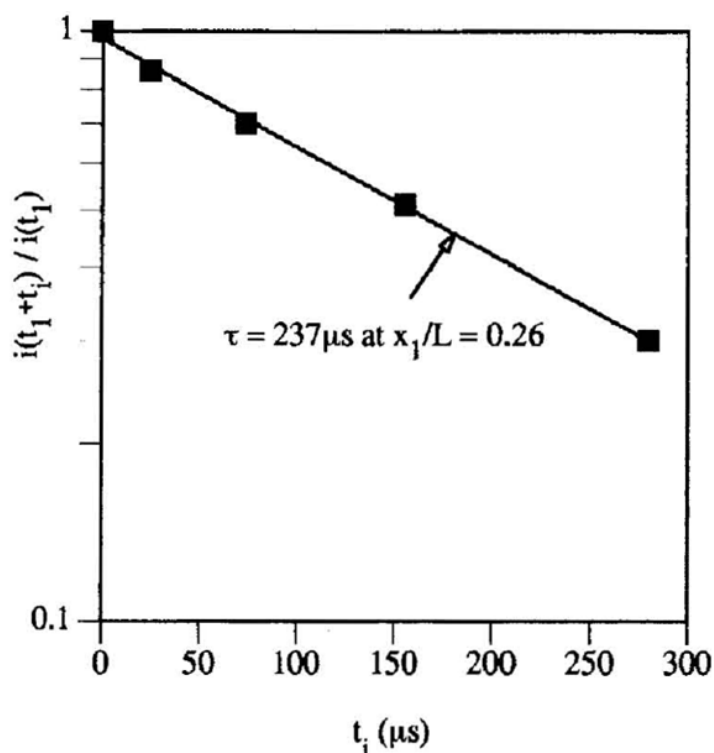


Figure 3.12 A typical example of semi-logarithm plot of ratio of photocurrent drop and interruption time. The slope of the fitting line is the carrier-trapping lifetime. After Walornyj [21]

The mobility or carrier-trapping lifetime measurements are realized by a TOF/IFTOF experimental setup, which includes a laser, an amplifier system, a high voltage (HV) supply and a HV switch system and a control and data acquisition system. A nitrogen gas laser is used to generate a very short light pulse that is absorbed near the surface of the a-Se film; this induces carriers near the surface of the sample. Since the transient photocurrent response is very small, an amplifier is used to amplify the signal. The amplifier is a voltage amplifier system. A high voltage switch system is used to perform the bias voltage interruption for

IFTOF measurements. The data were collected through a digital scope.

A grounded bridge network is used in the TOF/IFTOF experimental system. It is used to eliminate the displacement voltage transients that occur during the IFTOF measurement. [61] When the high voltage switches off and switches on during the IFTOF measurement, a displacement current will occur. In this bridge network, if the variable capacitance is adjusted to be equivalent to sample's capacitance, the voltage caused by the displacement current on both branches is equal. Then the differential amplifier system will only detect the photocurrent response since it is the only contribution to voltage difference across the bridges. A typical setup of the TOF/IFTOF measurement system is shown in Figure 3.13. Figure 3.14 and Figure 3.15 show the actual experimental setup used in the present experiments.

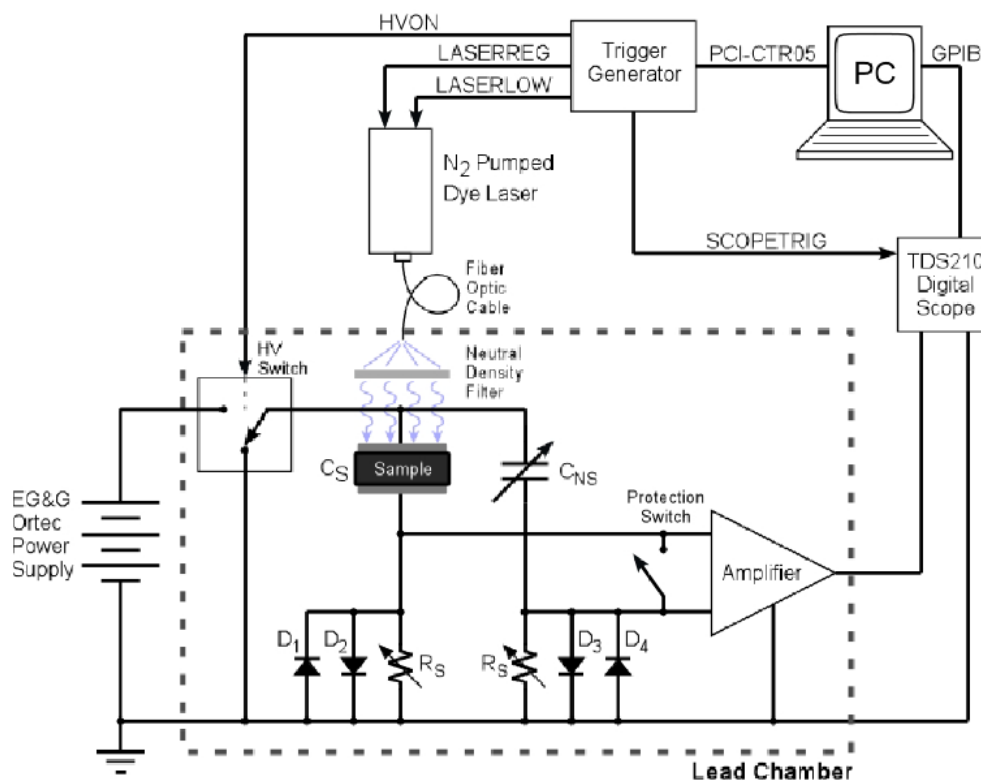


Figure 3.13 The TOF/IFTOF system schematic diagram. The amplifier system and high voltage system are simplified as the functional blocks in the diagram. After Fogal [3]

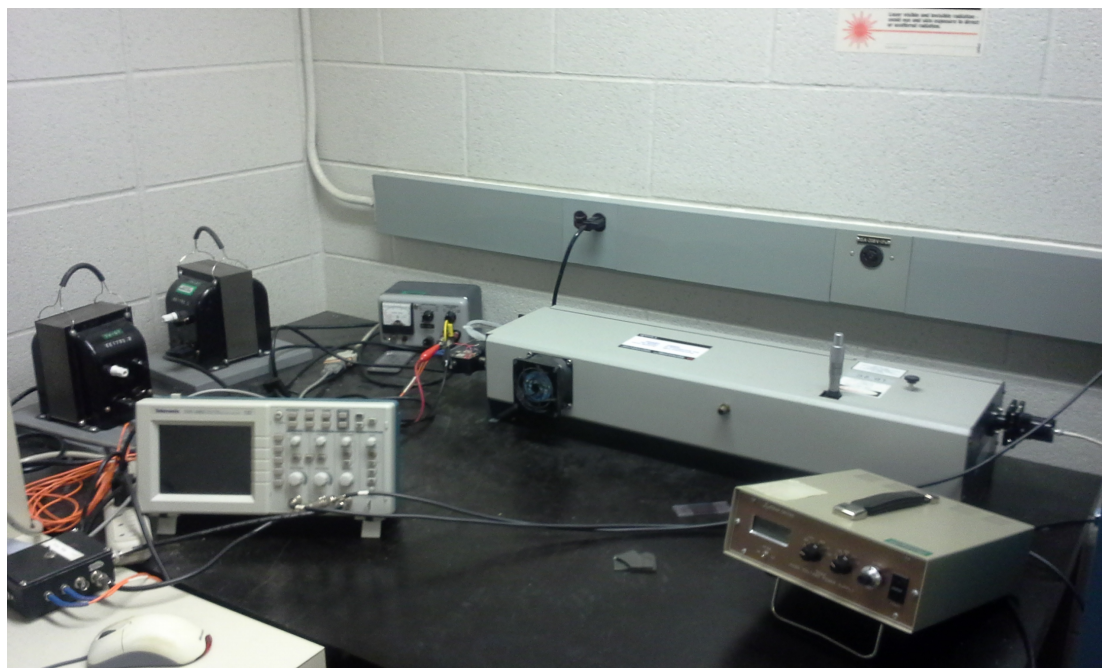


Figure 3.14. A partial experimental setup for TOF/IFTOF is shown above. A LN103C nitrogen UV laser, a 10V supplied triggering system, an EG&G high voltage supply, a Tektronix digital oscilloscope and a GPIB data acquisition box has shown in the figure.



Figure 3.15 The experimental setup inside the steel x-ray chamber. The Gendex GX-1000 X-ray tube head is above the whole TOF/IFTOF system. The grounded bridge network is built inside the black box at the bottom. A high voltage switch system is placed on the left side of the bridge network. A differential amplifier system and a protection switch are placed in the box on the right side of the bridge network. A temperature control system, which

includes a 12 volts power supply and an Omega temperature control system, is placed on the left side.

3.3.2 Laser and Trigger System

The experiments performed in this study used a nitrogen pumped LN103C laser with pulse duration of ~ 300 ps, power of 250 kW, and a peak spectral output at 337.1 nm (UV) with a 0.1 nm spread. This laser pulse is then fed through a Newport Optical Fiber adapter and into the X-ray chamber where the samples are placed for testing. It is possible to add a neutral density filter to reduce the photon flux within the laser path if the output is too intense, and the small signal condition is not satisfied. A black mask slightly smaller than the contact diameter is placed over the semitransparent top contact to stop any edge illumination and photo-generation within the fringe field around the edges.

The LN103C laser uses TTL signals to initiate triggering. Two inputs (REG and LOW) with BNC connections are used to fire the laser by creating a high voltage discharge across a spark gap. The timing begins with a pulse (with width longer than 100 ns) applied to REG. Between 30–50 μs later, a second 100 ns pulse must be applied to the LOW input; otherwise, after 50 μs , the laser will self-fire. This has been measured by Fogal [3] and it is shown in Figure 3.16.

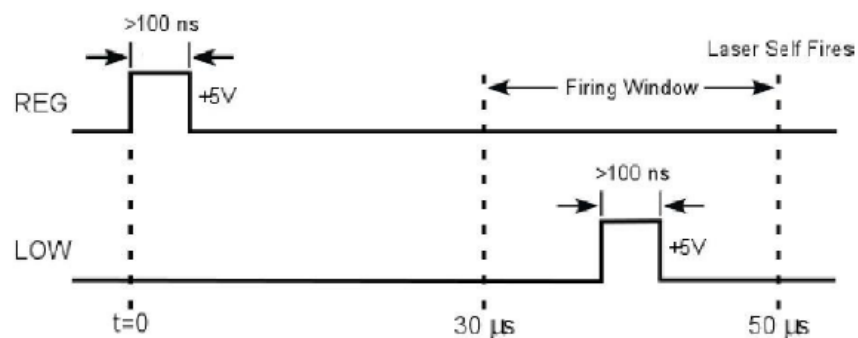


Figure 3.16 Trigger timing requirements for LN103C Laser. After Fogal [3]

These inputs have been optically coupled to the laser trigger electronic circuitry to avoid the feedback from large voltage switching transients effecting measurements. The laser triggering is controlled from a computer. A PCICTR05 counter board interfaced with the PCI bus provides the required signal timing. The counter board utilizes an AMD 9513 timer. The timing chip contains five 16 bit up/down counters. The counter board is controlled at a high

level by a library of manufacturer provided C++ functions. A LabView GUI called the C++ functions. Figure 3.17 shows the PCI-CTR05 interface circuit for generating the trigger system

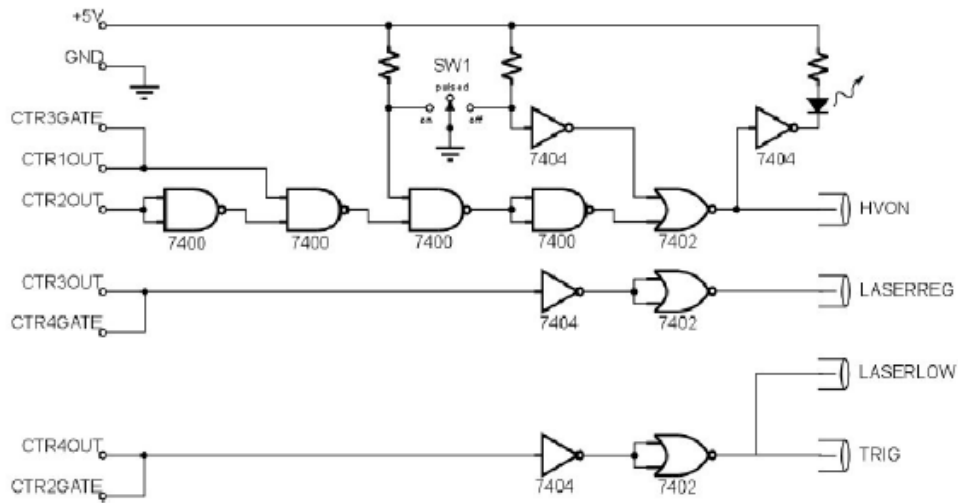


Figure 3.17 The PCI-CTR05 interface circuit for generating the trigger required trigger pulses. After Fogal [3]

The control signals from the counter board are sent to the interface circuit through a ribbon cable. The PC's power bus powers the interface circuit. A three setting manual switch allows for manual high voltage control. The switch allows user to choose high voltage mode during the measurement. The Timing signals from the PCI-CTR05 counter board and interface is shown in Figure 3.18.

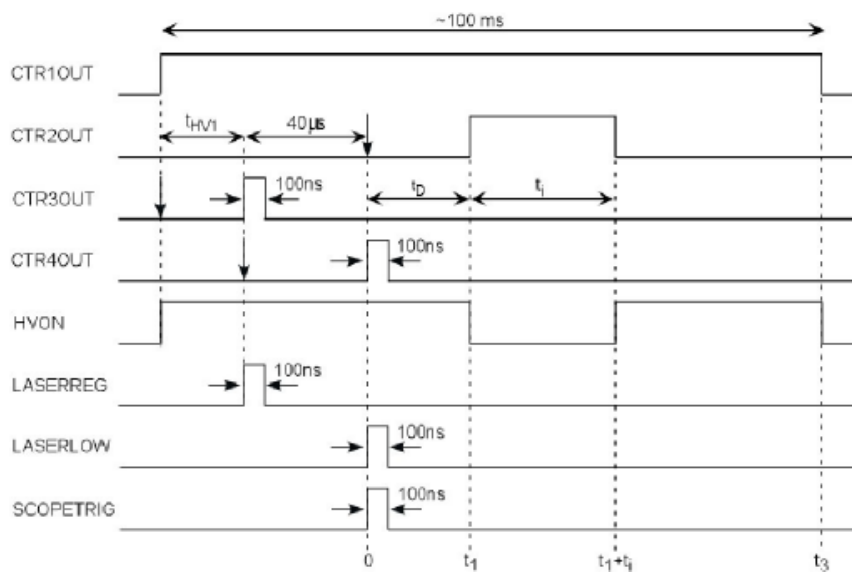


Figure 3.18 The Timing signals from the PCI-CTR05 counter board and interface. After Fogal [3]

The off-mode switches the high voltage supply off all the time while the on-mode switches it on all the time. The pulse-mode lets the user control the high voltage through various control signals. An LED is used to indicate the current state of the high voltage. A timing diagram is shown in Figure 3.18. This diagram provides the information on the sequence of signal triggering pulses and durations. HVON controls the state of the high voltage supply. The LASERREG commands the laser to be charged while LASERLOW makes the laser fire. The oscilloscope and laser firing are triggered simultaneously.

3.3.3 High Voltage Switch

The HV switch uses two fast switching n-channel HEXFETS in a totem pole configuration. It has a maximum switching voltage of 1 kV. When driven into conduction, the HEXFET passes current from the high voltage input to the high voltage output. Its circuit design is shown in Figure 3.19 below.

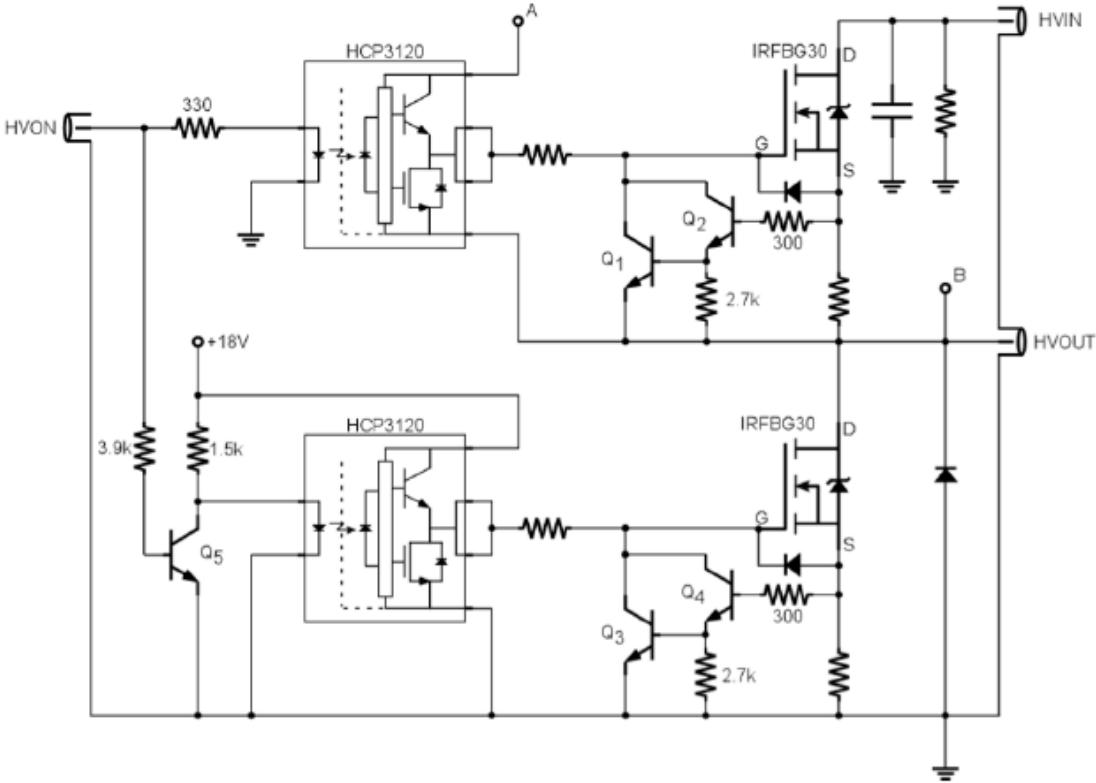


Figure 3.19 a 1kV fast switching high voltage HEXFET switch. After Fogal [3]

The type of HEXFET transistor used is a fast switching n-channel IRFBG30. It has a maximum rated gate-source voltage of $\pm 20V$. The gate voltage required to drive the

HEXFETs are supplied by two HCPL-3120 optocouplers, which also serve to isolate the control circuitry from the high voltage output of the switch. A floating, +18 V power supply provides the power to the upper optocoupler while a grounded +18 V power supply provides power to the lower optocoupler. The BJT transistors (Q1 – Q4) provide protection to the HEXFETS in case of a fault on the output since if the output current exceeds its maximum rating, Q₁ and Q₃ will switch on providing a short circuit path between the gate and source terminals. The bias voltage was supplied by an EG&G Ortec 556 high voltage power supply, which was connected to the input of the HV switch. To provide a positive bias for the transient photoconductivity measurements, the output of the HV switch was connected to the top electrode on the sample. The HV switch functions as a single pole double-throw switch with the output normally connected to ground through the lower HEXFET. A +5 V pulse at the trigger input connects the high voltage power supply to the sample through the upper HEXFET for the duration of the trigger pulse. A BJT invert (Q₅) at the input of the lower optocoupler ensures that only one HEXFET is conducting at a given time.

3.3.4 Amplifier System

A two-stage wide band differential amplifier is used to amplify the induced photocurrent signal across the sampling resistor. The design of this amplifier is shown in Figure 3.20 below.

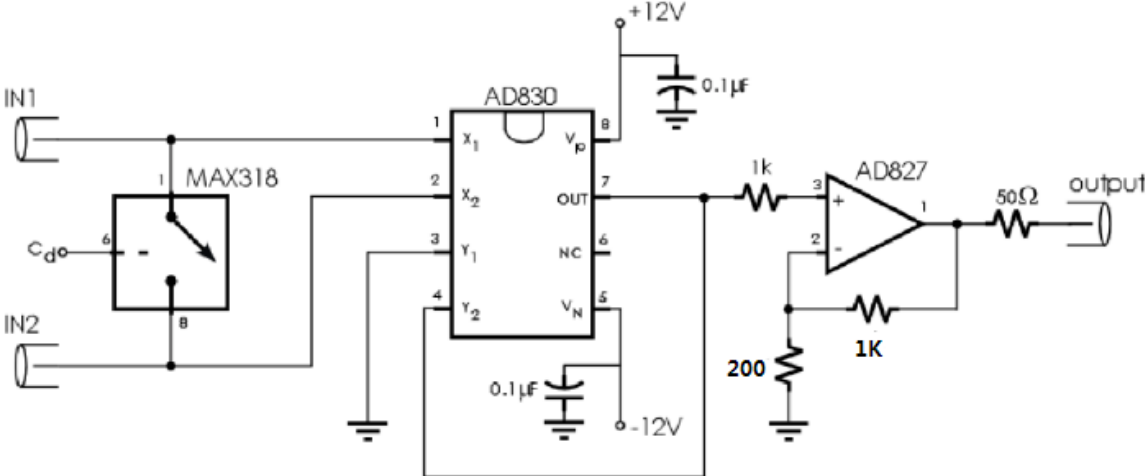


Figure 3.20 2-Stage bandwidth difference amplifier with 16 dB gain. Adapted from Fogal [3]

The first stage uses an Analog Devices AD830 wide bandwidth, which is a high CMMR video amplifier. This stage is configured to amplify the differential photocurrent

signal from the displacement current signal. The second stage uses an Analog Device AD827 non-inverting operational amplifier configured with 16 dB of gain to raise the signal above the noise floor of the oscilloscope and to drive the capacitance of the coaxial line connecting the amplifier to the oscilloscope. In order to protect the amplifier from the high voltage-switching transients, a Maxim MAX318 is connected across the inputs of the differential amplifier. It is a normally open CMOS analog SPST switch. The operation of MAX318 is controlled by an additional circuit, which provides the timing control for the switch. The circuit consists of an LS123 monostable multivibrator and an LS74 positive-clocked D flip-flop. The small signal bandwidth of the amplifier is estimated to be 12 MHz [3]. The transit time of carriers in a-Se is normally much longer than 1 μ s; therefore, the performance of the amplifier is more than satisfactory for the TOF/IFTOF measurement for the present test samples. The circuitry of the protection circuit is shown below along with its timing pulse duration in Figure 3.21.

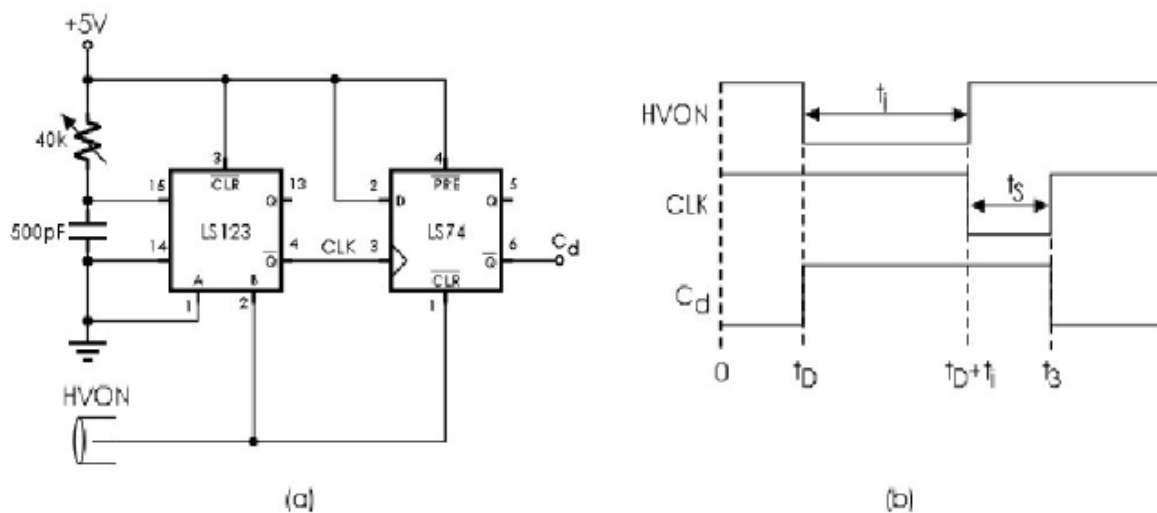


Figure 3.21 (a) The circuitry of the protection system. (b) The timing diagram. After Fogal [3]

3.3.5 Control and Data Acquisition System

The data acquisition system consists of two parts. The oscilloscope acquires the signal that comes out from the differential amplifier system. An 8-bit Tektronix TDS210 digital oscilloscope with a sampling rate of 1 Gb/s is used in the experimental setup. The amplifier is connected to the channel 1 of the oscilloscope through a cable. The input of channel 2 for the oscilloscope is the high-voltage controlling signal from the command terminal. The oscilloscope was interfaced with an OC using GPIB connection. A GUI user interface was

implemented on the PC. This GUI user interface was realized through LabView software. The parameters of the oscilloscope can be adjusted on this interface. User is able to choose the TOF/IFTOF modes for the measurement. A laser trigger delay set allows oscilloscope to capture the signal simultaneously with laser firing. The delay time set allows user to decide when to interrupt the applied field during the IFTOF measurement. User is also able to set the interrupt field duration for the IFTOF measurement on the interruption set. The system also allows user to perform TOF/IFTOF measurements for multiple times. The program can capture both the background signal and the photocurrent signal. Then it can acquire the true photocurrent signal from background subtraction. The waveform can be save in text.txt form on the computer. In addition, the interface provides calculation for the drift mobility and carrier-trapping lifetime. The interface is shown in Figure 3.22.

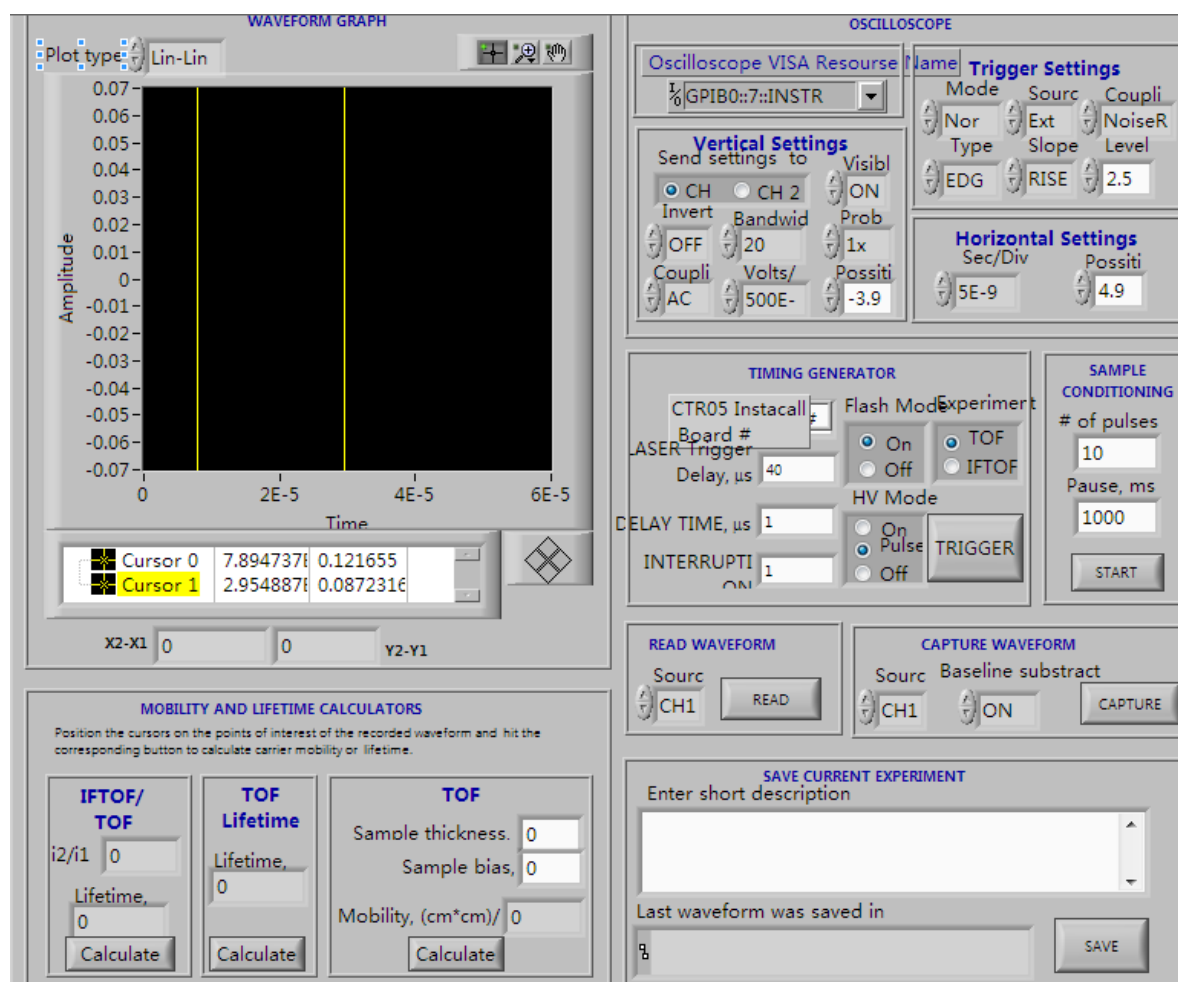


Figure 3.22 GUI user interface in LabView for TOF/IFTOF measurements

3.4 X-ray Induced Carrier-Trapping Lifetime Changes

The whole research hinges on two main goals. One goal is investigate how X-ray dose changes the carrier-trapping lifetime and other is to investigate how these changes recovery. Two measurement methods are then developed to achieve these goals

3.4.1 Accumulated Dose Measurement

The accumulated dose measurement investigates the X-ray induced carrier-trapping lifetime changes. It tracks the carrier-trapping lifetime changes under rapid irradiation. The a-Se device was placed on the sample platform. Two metal needles were attached to the sample, one to the gold contact on the surface of the a-Se and the other to the ITO on the glass substrate of the sample. In order to reduce the contact resistance, a small piece of indium was pasted to make better contacts. The sample was irradiated from the X-ray tube described above at 75 kVp for a time t seconds. Then the IFTOF measurement was immediately performed in order to acquire the carrier-trapping lifetime. The carrier-trapping lifetime is recorded and the process is repeated at each 30 seconds. A schematic diagram of the experimental schedule is shown in Figure 3.23.

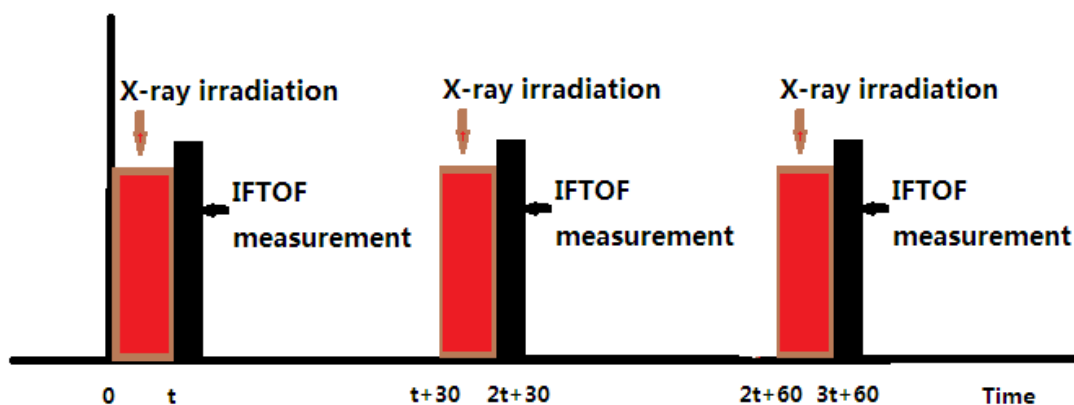


Figure 3.23 Procedure for accumulated dose measurements

The carrier-trapping lifetime of the sample is measured before the X-ray irradiation. This is not shown in the diagram above in Figure 3.23. The amount of dose that deposited into the sample is the same for each t period of irradiation. In most cases, the sample is irradiated multiple times until the dose deposited into the designed location reaches 10 Gy or more. In other cases, the experiment is terminated once the change of the lifetime is significant, normally a 40% change. Due to the nature of the defects generated by X-rays, the

carrier-trapping lifetime may recover a little during the 30 s step. At room temperature, the relaxation process is slow so that the carrier-trapping lifetime changes contributed from the relaxation process is negligible. The 30 s time step is shortened at higher temperatures.

3.4.2 Lifetime Recovery Measurement

The carrier-trapping lifetime decreases after irradiation by X-rays, and the carrier-trapping lifetime will gradually recover to the state before the irradiation. The lifetime recovery measurement tracks the carrier-trapping lifetime changes over a long period. The carrier-trapping lifetime was recorded during this recovery process. The IFTOF measurements were performed every $t(n)$ seconds for n time measurements, where

$$t(n) = \{t_n \in T \parallel t_n < t_{n+1}\}, T = \{t_1, t_2 \dots\} \quad (3.2)$$

The time step $t(n)$ for different recovery measurements is different because some relaxation processes are rapid while others are not. The time $t(n)$ increases with time because; initially the carrier-trapping lifetime changes quickly while the rate of change decreases later. A typical experimental process is shown in Figure 3.24.

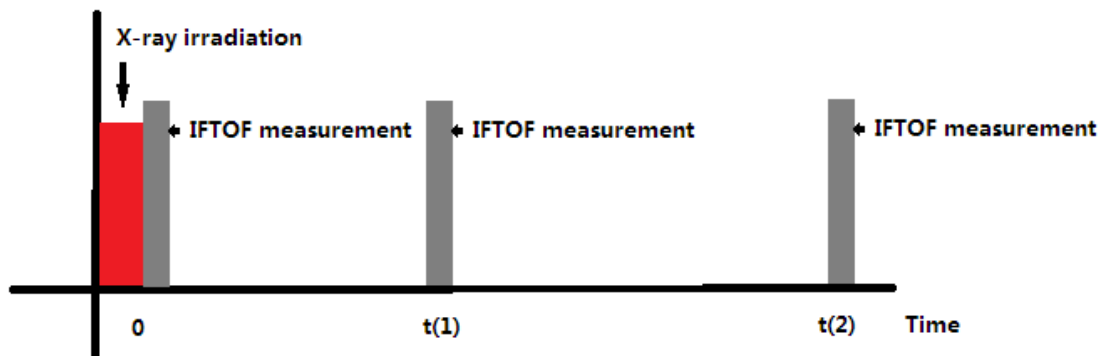


Figure 3.24 Schedule for lifetime recovery measurements

The experiment does not terminate until the carrier-trapping lifetime is approximately equal to the carrier-trapping lifetime before the irradiation. The time it takes for carrier-trapping lifetime to return to its initial state is different for each measurement. Hole and electron lifetimes have different relaxation times. In addition, the relaxation time also depends on the temperature. The time of recovery measurement may range from minutes to weeks; therefore, some trial measurements are conducted for samples. These trial measurements provide information on the range of recovery times expected.

3.5 Temperature Control System

One of the major goals in this experiment is to investigate the temperature dependence of the X-ray induced hole-trapping lifetime changes. The sample is placed in a sealed chamber. The temperature in the chamber is controlled through a heater and cooler. A 50 ohms resistor heater is used as a heating source. A CP60440 peltier cooler from CUI.inc is used as the cooling source. The Peltier cooler is 40×40 mm with a 6 A input. The Peltier cooler draws heat from the sample to the underside. A tube with continuous flowing water is used as the heat sink under the Peltier cooler in order to effectively dissipate the heat. The water following through the tube is about 0 °C. The heater is able to heat up the sample to hundred degrees alone while the Peliter cooler is able to cool it down below zero degrees alone. An Omega CNI3252-C24 temperature controller externally controls the heater and cooler. The temperature controller is supplied by an external +20 V DC source. It controls the temperature through thermal coupling. It passes a controlled current through the heater when the sample temperature is below the desired temperature. Once the desired temperature is reached, it cuts the current into the heater and switches on the Peltier cooler simultaneously to prevent further heating. The temperature of the sample is controlled to within 0.5°C of the desired temperature. Figure 3.25 shows a schematic diagram of the temperature control system.

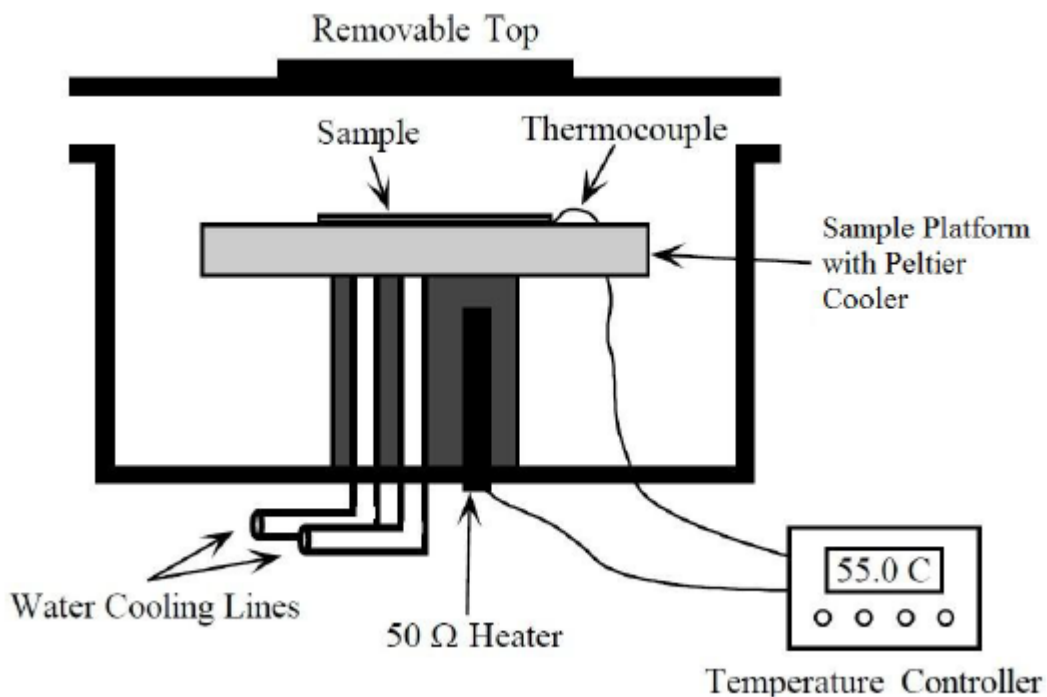


Figure 3.25 A chamber with the temperature control system. Adapted from Allen [62]

Before the experiment starts, the chamber is filled with ultra high purity nitrogen gas. A vacuum pump is connected to the chamber. It first drains air out of the chamber. Then, a bottle of ultra high purity nitrogen gas bottle is connected to the chamber. The chamber is filled with nitrogen gas before the temperature control system to adjust the temperature inside the chamber. The main goal for this process is to provide a stable environment for experiments. If the chamber is full of air, then water vapor condenses at lower temperatures (around and below 0 °C). Condensation will affect the photo-generation of carriers at the surface of the sample and it will also affect the stability of the a-Se sample, which may crystallize over time, before all the experiments could be done. Therefore, water vapor needed to be extracted from the chamber at the beginning of the experiments.

3.6 Measurement of Capacitance Changes Due to X-rays

3.6.1 Capacitance Measurement

The capacitance is measured through GenRad RLC 1658 digibridge. Two contact needles from GenRad RLC 1658 digibridge were attached to the top and bottom electrode of the sample. The capacitance of sample is then obtained. The digibridge is shown in Figure 3.26 below.



Figure 3.26 GenRad RLC 1658 digibridgre

3.6.2 Long Time Irradiation Measurement

The Faxitron X-ray cabinet system shown below is used to perform long-time irradiation. It is shown in Figure 3.27 below.



Figure 3.27 Faxitron X-ray cabinet

The Faxitron X-ray cabinet system has a Tungsten X-ray tube head with a 0.76 mm Beryllium window. The filament current of X-ray tube is 2.5 mA and it can operate from 30 kVp up to 140 kVp. The maximum continuous irradiation time for the system is 59 minutes and 59 seconds. For the capacitance changes measurement, the Faxitron X-ray tube was set to be 75 kVp and 30 minutes for the irradiation time. The sample is placed at the bottom of the chamber. The capacitance of the sample is measured after the 30 minutes irradiation and compared to its initial capacitance.

3.7 Summary

In this chapter, the experimental procedure for sample preparation is shown. The samples that are used in the research are stabilized amorphous selenium (a-Se) films and. The samples are fabricated through vapor deposition and the thickness of the samples is designed to be 150 μm . The electrodes are deposited on the samples through a sputtering system. The

X-ray dose measurement and delivered dose estimation are also introduced in this chapter. A dental X-ray tube is used as the main X-ray source in the experiments that examined the carrier lifetimes. A dosimeter system along with an ion chamber is used to measure the exposure from the X-ray tube. A python based program is used to perform the estimation of X-ray dose delivered into the sample

The main research goal is to investigate the X-ray induced changes in carrier-trapping lifetime. Therefore, IFTOF technique is used and a corresponding IFTOF measurement system is described. IFOTF measures the transient current caused by the drift of carriers. A pulsed UV laser and these photo-injected carriers move under an applied field, which is provided by a high voltage bias on the sample, generate carriers. During the IFTOF measurement, the applied field is interrupted. The field is switched off and it is switched on after an interruption time. A high voltage switching system realizes this process. Since a displacement current or displacement voltage transient will occur during the interruption, a grounded bridge network along with a differential amplifier system was used to eliminate this effect. The differential amplifier system also amplifies the transient signal, which makes it easier for the observer to acquire the signal. The transient signal is acquired by a digital oscilloscope and transferred to the computer. A user interface is created on the computer, which allows the user to control the whole IFTOF experimental setup and the measurement sequence

In addition to the IFTOF measurement setup, a temperature control system is also developed to realize the control of the sample temperature. A resistance heater and a Peltier cooler are used to realize the thermal coupling process and the control of the temperature by a heater and a cooler. The sample and the platform are inserted in an isothermal chamber. Two sets of measurements are designed to study the X-ray induced carrier-trapping lifetime changes. The accumulated dose measurements track the carrier-trapping lifetime changes with deposited and accumulated X-ray dose. The IFTOF measurement is performed on the sample right after irradiation, and the whole process is repeated until a large amount of dose is deposited. The recovery process measurements track the carrier-trapping lifetime changes (recovery) after the cessation of all X-ray irradiation. The sample is put in the dark and IFTOF measurement is performed on the sample at certain time periods. In addition, a capacitance measurement is conducted. The latter measurement has the goal of investigating whether a=Se films experience capacitance changes under X-ray irradiation due to polarization effects such as trapped charges in the bulk.

4. Results and Discussion

4.1 Introduction

The experimental setup and methodology have been introduced in the last chapter. The experiments have been conducted and the results are presented in this chapter. The experimental results include the X-ray dose measurement, dose rate dependence in carrier trapping lifetime measurements, temperature dependence in carrier-trapping lifetime measurements and lifetime recovery measurements, and X-ray capacitance measurements. All samples, which are used in the X-ray dose rate dependence and temperature dependence measurements, are a-Se:0.3%As:5ppm Cl samples. The nominal thickness of the samples is 150 μm . The sample thickness has 1~2 μm variance at different positions of the samples. Since the variance is very small, it does not affect the result of the experiments.

4.2 Experimental Calculation of X-ray Dose Deposited in the a-Se Samples

The dose delivered into an ion chamber at fixed X-ray tube peak voltage depends on the distance between ion chamber and X-ray tube. It also depends on the filament current of the X-ray tube. A set of different sample positions and different X-ray filament currents are chosen in order to realize the dose rate difference. The X-ray tube is Gendex GX-1000 and its peak voltage has been fixed at 75 Kvp during measurement. The X-ray dose rate measurements are done for all different sample positions and X-ray tube filament current. The dose rates from dosimeter are shown below in Table 4.1. The sample position is the distance between sample and X-ray window. The X-ray window is not the head of the actual

X-ray tube, so the sample position and dose rate do not follow the inverse square relation. The exposure rate measured from X-ray tube is given in Table 4.1 below. The dosimeter and the ion chamber that are mentioned in Chapter 3 are used.

Table.4.1 Dosimeter measurement results for Gendex GX-1000 at 75 Kvp at different position and different filament current.

Sample Position (cm)	Filament Current (mA)	Dose rate (R/s)
1.0	15	3.55
7.5	15	0.67
8.9	15	0.52
8.9	10	0.35
9.7	15	0.46
9.7	10	0.31

The measurements give the dose rate that is deposited into the ion chamber. The dose deposited into the sample is then calculated through a program dose.py. The dose.py follows the calculation methods described in the theoretical part and its code has been listed in the appendix part. Since the dose deposited into the sample has an exponential decay with respect to the depth from the surface, it is more accurate to examine the dose effect at a specific position. Since the dose varies through the bulk structure of the sample, the amount of traps generated by X-ray is different through the sample. Additionally, the IFTOF measurement studies the carrier-trapping properties at a specific location in the sample or a small region in the sample. Since average dose rate may not be the true dose rate at specific position, the result obtained from IFTOF measurement would lose its validity. In the experiment, the position was chosen to be 40 μm beneath the top surface of the sample. The dose is at this position is then calculated through dose.py and the result is shown in Table 4.2.

Table.4.2 Dose deposited rate at 40um beneath the surface.

Sample Position (cm)	Filament Current (mA)	Dose rate (Gy/s)
1.0	15	1.95
7.5	15	0.37
8.9	15	0.29
8.9	10	0.19
9.7	15	0.26
9.7	10	0.17

The estimated distance from X-ray tube to the window of the X-ray tube is about 4 cm. So a theoretical estimation of dose rate at different positions can be obtained through the relation

$$\text{Dose rate}(\dot{D}) \propto \text{Distance}^{-2} \quad (4.1)$$

The highest dose rate was used as the reference point. The dose rate was then examined at various positions to verify the inverse square decay relationship. The theoretical estimated dose rate at different positions was then calculated and listed in Table 4.3 below.

Table 4.3 Theoretical dose rate estimation based on inverse square law.

Distance (cm)	Filament Current (mA)	Dose rate (Gy/s)
5.0	15	1.950
11.5	15	0.369
12.9	15	0.293
12.9	10	0.195
13.7	15	0.260
13.7	10	0.173

The comparison of the theoretical estimation to experimental measurement shows that the result is very close and the maximum difference is only 2%. This indicates that our experimental setup for different dose rate measurements has been verified.

In summary, the X-ray dose rate measurement shows that the dose rate adjustment setup fulfills its design purpose. In addition, the dose rate result obtained from the X-ray dose rate measurement can then be applied in the following studies.

4.3 X-ray Dose Rate Dependence of Carrier-trapping Lifetime Reduction

The research goal is to examine if there is dose rate dependence in the carrier-trapping lifetime reduction due to accumulated X-ray dose. The research is conducted on both electrons and holes. The previous experiment has shown that the carrier-trapping lifetime for both electrons and holes will decrease upon X-ray irradiation deposition into the sample. The analysis is done on normalized carrier-trapping lifetime in order to have a better understanding of the reduction effects brought by X-ray irradiation. The normalized

carrier-trapping lifetime is the ratio between the carrier-trapping lifetime after irradiation and the carrier-trapping lifetime before irradiation. It provides a direct view of reduction percentage of the carrier-trapping lifetime. In addition, it allows the comparison of lifetime reduction between different samples.

As mentioned in Chapter 3, the actual IFTOF experimental setup experiences a time delay during the interrupted field time of flight measurements. The carrier-trapping lifetime obtained from the transient signal drop might not be the true carrier-trapping lifetime from the IFTOF measurement. Therefore, it is necessary to test if the carrier-trapping lifetime from interrupted field time of flight measurement is sufficiently accurate enough to be useful.

In Chapter 2 and Chapter 3, it is demonstrated that there are two ways to obtain the carrier-trapping lifetime through interrupted field time of flight measurements. The first one uses the voltage drop at certain interruption time to calculate the carrier-trapping lifetime. The other one uses the semi-logarithm plot of transient signal drop verse interruption time. The first one only requires one single IFTOF measurement while the second one requires multiple time measurements. For the current experiment setup in the laboratory, it is necessary to do a comparison of the results obtained from two methods. This comparison will provide the information on which method should be used to obtain the carrier-trapping lifetime in the later experiments.

The IFTOF measurements are performed on the sample and the carrier-trapping lifetimes are obtained. Three different interruption times are chosen and they are listed in Table 4.4. The corresponding IFTOF waveform is shown in Figure 4.1.

Table 4.4 Different interruption times for IFTOF measurements.

Label	t_2	t_3	t_4
Interruption time	6 μ s	9 μ s	12 μ s

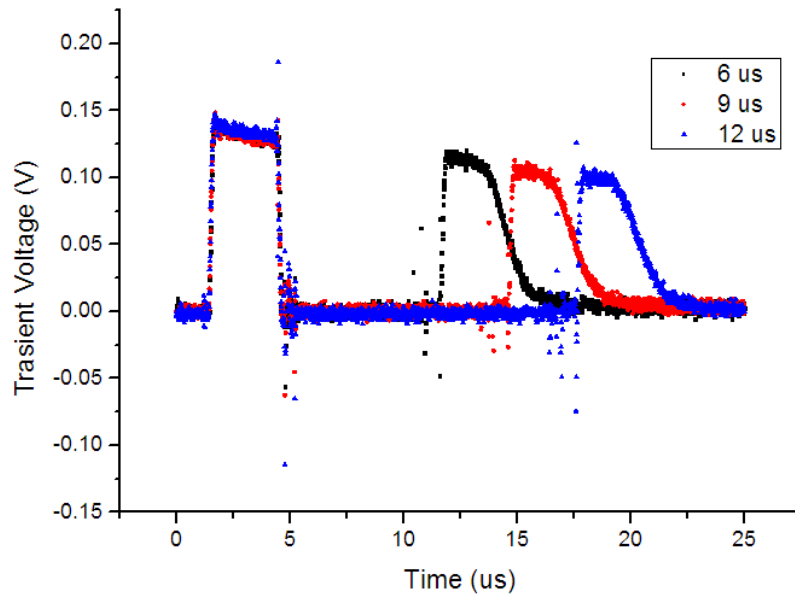


Figure 4.1. The interruption field time of flight waveform for three different interruption time.

For different interruption times, the ratio between the transient voltage before the irradiation and after the irradiation is listed in Table 4.5 below. The logarithm of the voltage ratio versus the interruption time is also plotted in Figure 4.2 in order to obtain the carrier-trapping lifetime from the slope.

Table 4.5 The transient voltage drop ratio for different interruption time.

Interruption time (μs)	6	9	12
Voltage ratio $v(t_2)/v(t_1)$	0.89	0.84	0.80

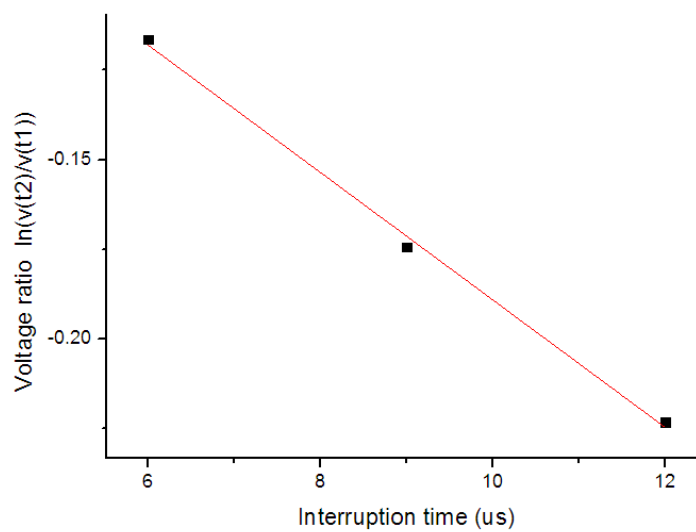


Figure 4.2 The logarithm of voltage ratio verse the interruption time.

The slope of the Figure 4.2 is about 0.0175, which give a hole-trapping lifetime about of 57 μs . The hole-trapping lifetime obtained from the direct calculation through Equation 2.29 in Chapter 2 is about 52 μs . This is much smaller than the slope method. However, if one uses the interruption time plus the delay time as the interruption time for the calculation, the result is about 57 μs . This value is very close to the value that is obtained from the slope of Figure 4.2. Therefore in the later experiment, it is still valid to apply Equation 2.29 in Chapter 2 to calculate the carrier-trapping lifetime. The only difference is that the interruption time is the interruption set for the experiment plus the delay time due to protection circuit.

Therefore, the carrier-trapping lifetimes for both hole and electron were acquired through IFTOF measurement at room temperature before X-ray irradiation. They are listed in Table 4.6 below.

Table 4.6 Carrier-trapping lifetime before irradiation

Carrier	Carrier-trapping lifetime (μs)
Hole	59 ± 5
Electron	462 ± 40

The hole-trapping lifetime is much smaller than electron-trapping lifetime. This indicates that it takes much less time for a hole to be trapped than for an electron when it drifts through the sample. This does not directly imply that concentration of electron traps is higher than that of hole traps. The drift mobility of holes is much larger than that of electron. The mobility of hole in a-Se alloy is normally about 4 - 5 times larger than that of electron.

Accumulated dose measurements are then repeated at different dose rates for the samples. The dose rate is chosen based on the previous X-ray dose measurements. The amounts of dose delivered into the sample each irradiation are fixed for different dose rates.

$$\text{Dose(Gy)} = \text{Dose Rate} \left(\frac{\text{Gy}}{\text{s}} \right) \times \text{Time(s)} = \text{Constant} \quad (4.2)$$

The dose for each irradiation interval is fixed so that the dose rate is the only variable for different dose rate measurements. The dose that is delivered into the sample at different dose rates may vary a little. Since the dose rate varies a lot, the irradiation time for each dose rate changes a lot. For instance, at a dose rate of 0.17 Gy/s, the irradiation time for each interval is 5.5 s. At a dose rate of 1.95 Gy/s, the irradiation time for each interval is 0.5 s. The interval of irradiation for each measurement is smaller than the time step 30 s between each

irradiation. For both electron and hole measurements four different dose rates have been chosen. The dose rates that are used in the experiments are listed in Table 4.7.

Table 4.7 Different dose rate chosen for electron and hole measurements

Hole (Gy/s)	0.17	0.26	0.37	1.95
Electron (Gy/s)	0.19	0.26	0.29	1.95

The carrier-trapping lifetime is obtained through accumulated dose measurement and saved as raw data. For each dose rate, a set of accumulated dose rate measurements are done on the samples. The raw data have been listed in the appendix. The carrier-trapping lifetime is normalized with respect to the carrier-trapping lifetime before the irradiation.

$$\tau_{\text{normalized}} = \frac{\tau_{\text{IFTOF measurement}}}{\tau_{\text{Initial}}} \quad (4.3)$$

For hole-trapping lifetime reduction due to X-ray irradiation, the accumulated X-ray dose was deposited up to 10 Gy. For electron-trapping lifetime reduction due to X-ray irradiation, the accumulated X-ray dose was deposited up to 20 Gy. The normalized hole-trapping lifetime changes due to X-ray accumulated dose is shown in Figure 4.3. The normalized electron-trapping lifetime changes due to X-ray accumulated dose is shown in Figure 4.4. The accumulated dose effect is conducted under four different dose rates for both electron and hole.

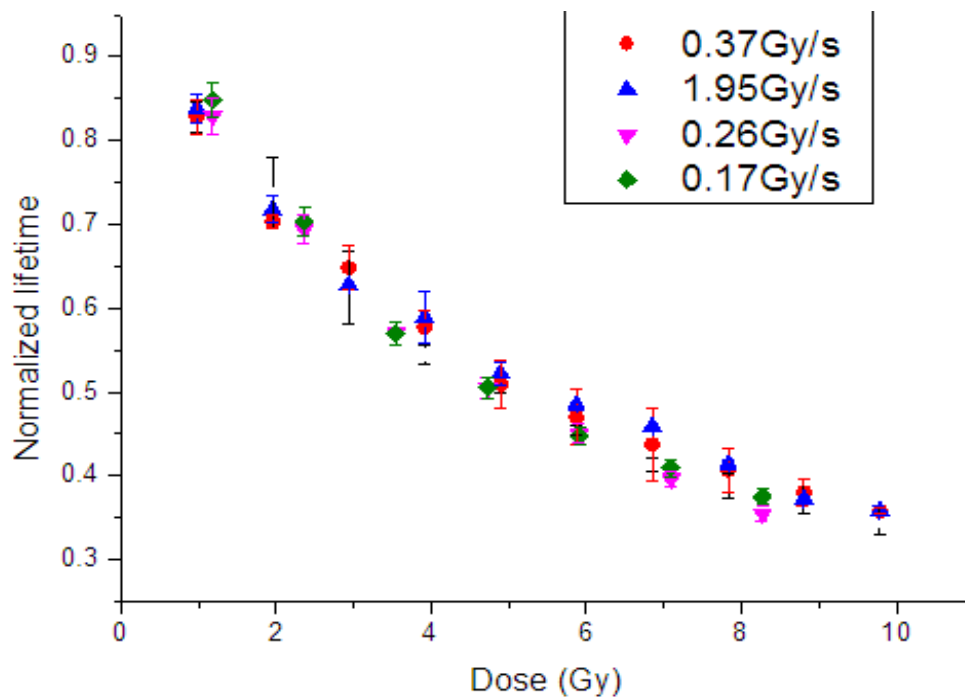


Figure 4.3 Normalized hole-trapping lifetime reduction due to X-ray irradiation at different dose rates.

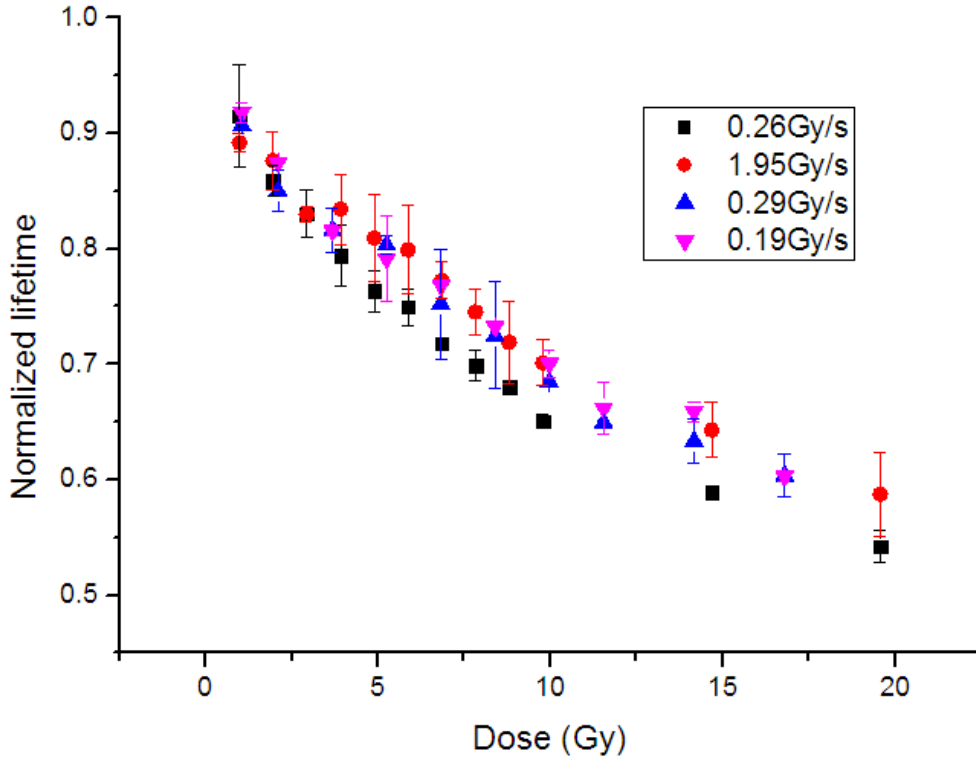


Figure 4.4 Normalized electron-trapping lifetime reduction due to X-ray irradiation at different dose rates.

The normalized hole-trapping lifetime reduces up to 40% when the accumulated dose reaches 10 Gy. The normalized electron-trapping lifetime is reduced up to 60% when the accumulated dose reaches 20 Gy. For both electrons and holes, their normalized carrier-trapping lifetimes reduce as accumulated dose increases. Comparing electrons and holes, at same amount of dose, the normalized hole-trapping lifetime reduces more than normalized electron-trapping lifetime.

For accumulated dose measurement at a fixed dose rate, the normalized carrier-trapping lifetime decreases as the X-ray dose increases. The X-ray energy deposited into the sample generates new defects in the sample. As the number of defects increases, the average time of a carrier to be trapped by defects decreases. Comparing the carrier-trapping lifetime reductions due to X-ray dose at different dose rates, they vary only a little. Furthermore, the normalized carrier-trapping lifetime shows a decay with respect to dose. That can be described as ^[14]

$$\tau_{\text{normalized}} = \frac{1}{1+A \times \text{Dose}} \quad (4.4)$$

where A is defined as normalized lifetime change rate. The larger normalized lifetime change

rate means that it requires less deposited X-ray energy to generate defects.

This relation can be explained by assuming that the probability of trapping per unit time is proportional to the connection of traps, that is $\frac{1}{\tau} \propto N_{\text{traps}}$. The traps are essentially capture centers in the samples. Before irradiation, carrier-trapping lifetime is determined by intrinsic defect concentration. One can define the initial carrier-trapping lifetime as [21]

$$\frac{1}{\tau_0} = C \times N_0 \quad (4.5)$$

Where C is the capturing coefficient and N_0 is the initial number of defects per unit volume in the sample. The X-ray dose generates new defects with a concentration $N_{\text{X-ray}}$; we assume the concentration of defects generated by X-ray is proportional to the dose [21]

$$N_{\text{X-ray}} \propto \text{Dose} \quad (4.6)$$

The total concentration of defects after irradiation is then

$$N = N_0 + N_{\text{X-ray}} \quad (4.7)$$

By applying the proportional relation of reciprocal carrier-trapping lifetime and defects concentration, the equation can be simplified as

$$\frac{1}{C \cdot \tau} = \frac{1}{C \cdot \tau_0} + \text{Constant} \times \text{Dose} \quad (4.8)$$

Rearranging the equation

$$\frac{\tau_0}{\tau} = 1 + C \cdot \text{Constant} \times \text{Dose} \quad (4.9)$$

Using the notation of normalized carrier-trapping lifetime and defining $C \times \text{Constant}$ as A

$$\tau_{\text{normalized}} = \frac{1}{1 + A \times \text{Dose}} \quad (4.10)$$

The normalized lifetime change rate A is then obtained through rational fitting of normalized carrier-trapping lifetime and the accumulated dose data. The normalized lifetime change rate is calculated for all dose rates. The fitting diagrams are listed in the appendix. The normalized lifetime change rate of hole at different dose rates is listed in Table 4.8. The normalized lifetime change rate of holes at different dose rates is listed in Table 4.9.

Table 4.8 The dependence of the normalized lifetime change rate of holes on the dose rate.

Dose rate (Gy/s)	Normalized lifetime change rate (Gy ⁻¹)
1.95	0.186 ± 0.03
0.37	0.191 ± 0.02
0.26	0.206 ± 0.11
0.17	0.199 ± 0.02

Table 4.9 The dependence of the normalized lifetime change rate of electrons on the dose rate.

Dose rate (Gy/s)	Normalized lifetime change rate (Gy^{-1})
1.95	0.043 ∓ 0.01
0.29	0.046 ∓ 0.01
0.26	0.054 ∓ 0.02
0.19	0.043 ∓ 0.01

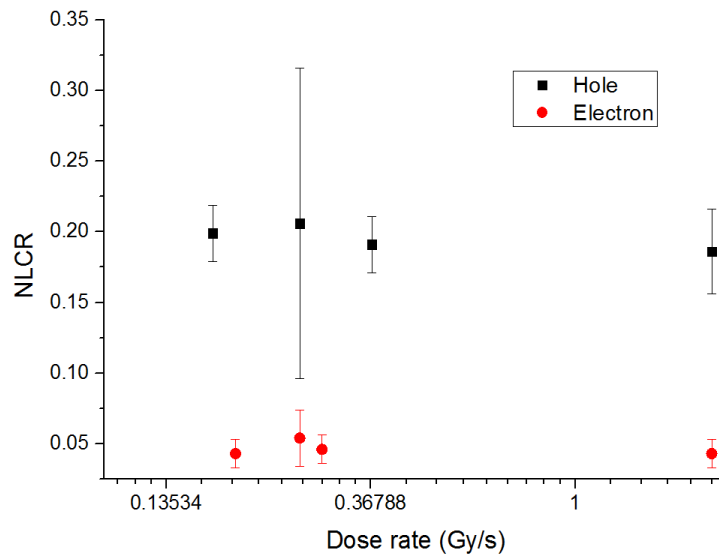


Figure 4.5 NLCR at different dose rates.

The maximum dose rate is an order of magnitude larger than the minimum dose rate differs; however, the normalized lifetime change rate only varies by about 10%. The normalized lifetime change rate does not depend on the dose rate. At different dose rates, the decrease of normalized carrier-trapping lifetime, due to deposited X-ray dose, differs very little. The dose based exponential decay is sufficient to describe the normalized carrier-trapping lifetime decay. It does not show a necessity to add a new dose rate variable to describing the lifetime vs. X-ray irradiation data.

The total amount of dose seems to determine the number of defects generated during the X-ray photon interaction in the sample. The dose rate decides the rate of energy deposited into the sample or X-ray photons interacted with the a-Se atoms. The experimental observation suggests that the defects generated by X-rays are stable. They do not disappear immediately which accords with other experiments. In addition, the generated defects will not be affected by X-ray photons. At higher dose rates, most of defects are generated simultaneously. At lower dose rate, some defects are generated initially and they have time to

further interact with later X-ray photons or a-Se structure itself. However, based on the experimental results, the defects either do not further interact with X-ray photons or have less priority when an X-ray photon interacts with a-Se structures. Therefore, when X-ray dose rate is in a range of 0.2 Gy/s to 2 Gy/s, the carrier-trapping lifetime due to X-rays only depends on the total X-ray energy that is deposited into the sample. This conclusion may not be applied to an extremely high dose rate. At extremely high dose rates, a large number of defects are generated at a short time. These defects tend to experience a structural relaxation process, which has a dependence on the number of defects in the sample. If the concentration of defects were extremely high, then the initial recovery speed would be very quick. Since the carrier-trapping lifetime is obtained through an IFTOF experimental measurement, there is small experimental time delay between the X-ray irradiation and IFTOF experimental measurement. Some of the defects may disappear during that time delay. Therefore, the carrier-trapping lifetime may be somewhat larger than the true carrier-trapping lifetime caused by X-ray.

In summary, for both electrons and holes, during the accumulated dose measurements, the carrier-trapping lifetime reduction due to deposited X-ray dose is independent of the X-ray dose rate. In addition, the normalized lifetime change rate for holes is much larger than that for electrons.

One can further explore the X-ray detector sensitivity changes due to accumulated dose based on the results above. The mobility change due to deposited X-ray dose is very small ^[3]. However, the carrier-trapping lifetime change due to accumulated dose is very significant. As shown in this section, the hole-trapping lifetime decreases by 40% of its initial value upon receiving a dose of 10 Gy. The electron-trapping lifetime also decreases down to 70% of its initial state upon receiving 10 Gy. Therefore the sensitivity changes due to deposited X-ray dose will be mainly contributed from carrier-lifetime changes.

The sensitivity is related to mobility and carrier-trapping lifetime as stated in Chapter 1. A numerical relationship between these two parameters and sensitivity can be given by [10].

$$S = P \times \{R_e + R_h\} \quad (4.11)$$

where

$$P = \frac{5.45 \times 10^{13} \times e}{\left(\frac{\alpha_{\text{air}}}{\rho_{\text{air}}}\right) W_{\pm}} \left(\frac{\alpha_{\text{en}}}{\alpha}\right) \quad (4.12)$$

$$R_h = \mu_h \tau_h E \left[(1 - e^{-\alpha L}) + \frac{1}{\frac{1}{\alpha \mu_h \tau_h E} - 1} \left(e^{-\frac{L}{\mu_h \tau_h E}} - e^{-\alpha L} \right) \right] \quad (4.13)$$

$$R_e = \mu_e \tau_e E \left[(1 - e^{-\alpha L}) + \frac{1}{\frac{1}{\alpha \mu_e \tau_e E} + 1} \left(e^{-\frac{L}{\mu_e \tau_e E} - \alpha L} - 1 \right) \right] \quad (4.14)$$

where α_{air} is the energy absorption coefficient for air, α_{en} is the energy absorption coefficient of amorphous selenium, α is the linear attenuation coefficient of amorphous selenium, ρ_{air} is the density for air, W_{\pm} is the EHP creation energy in amorphous selenium, E is the applied field, L is the thickness. The normalized sensitivity can be given as

$$S_{\text{normalized}} = \frac{S_{\text{irradiated}}}{S_{\text{unirradiated}}} \quad (4.15)$$

One can assume that the first term P for sensitivity remains unchanged after irradiation. A simple analysis of how deposited X-ray dose changes the sensitivity can be now done as follows. Considering two samples, one is 200 μm and the other is 500 μm . X-ray induced electronic property changes follows the result above. The normalized lifetime change rates for electrons and holes are 0.046 Gy/s and 0.2 Gy/s respectively. The hole mobility is about $0.13 \text{ cm}^2\text{V}^{-1}\text{s}^{-1}$ and The electron mobility is about $0.03 \text{ cm}^2\text{V}^{-1}\text{s}^{-1}$. The mean X-ray energy for 75 kVp is 40 keV. Two samples are examined under two operating field corresponding to 1 V/ μm and 10 V/ μm . Then, the normalized sensitivity changes due to X-ray dose can be obtained from Equation 4.11- 4.15 and it is plotted on Figure 4.6

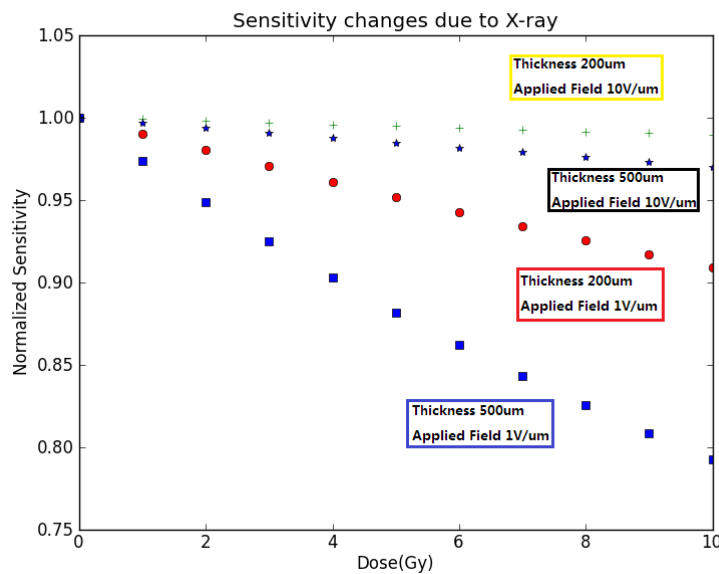


Figure 4.6 Normalized X-ray sensitivity versus deposited X-ray dose.

The X-ray sensitivity decreases with deposited X-ray dose. The X-ray sensitivity of the thicker sample decreases more under the same field. The X-ray sensitivity decreases less under a larger field. The results are in agreement with the theoretical analysis and experimental observations. The normal working field for a-Se based X-ray detector is about 10 V/ μm . [3] The sensitivity loss is less than 2 %. Therefore, a-Se is a good choice as a large area X-ray photoconductor.

4.4 Temperature Dependence of X-ray Induced Hole-trapping Lifetime Changes

The previous experiments have shown that the X-ray induced carrier-trapping lifetime changes and its structural relaxation process depend on the temperature. [21] The measurement of electron-trapping lifetime changes due to a temperature difference has been done previously. In this work, the goal is to investigate the X-ray induced effects on the hole-trapping lifetime as a function of temperature. In addition, samples, which have composition a-Se:0.3%As: 5ppm Cl are used for the temperature experiments.

The hole-trapping lifetime is measured at different temperatures before the X-ray irradiation. The sample temperature was controlled through a temperature controller. Three different temperatures corresponding to 10 °C, 23.5 °C, 35.5 °C are chosen. The glass transition temperature of a-Se:0.3% As:5ppm Cl sample is about 50 °C. All the experimental temperatures are chosen to be below glass transition temperature in order to avoid rapid structural changes at the glass transition temperature. The IFTOF measurements were conducted at different temperature in order to measure the hole-trapping lifetime. The hole-trapping lifetime at different temperature is given below in Table 4.10.

Table 4.10 Hole-trapping lifetime before irradiation at different temperatures

Temperature (°C)	Hole-trapping lifetime (μs)
10	76 \pm 8
23.5	60 \pm 4
35.5	48 \pm 4

The hole-trapping lifetime decreases as temperature increases. From 10°C to 35.5°C,

the average lifetime decreases from 76 μ s to 48 μ s, from 10 °C to 35.5 °C, nearly 40% reduction. The hole-trapping lifetime reduction is about 1.5% per temperature increase of 1°C. This increment is not a linear increment. At higher temperature, the carrier-trapping lifetime changes more rapidly.

Accumulated dose measurements are performed on hole-trapping lifetime at different temperature. Since the carrier-trapping lifetime is different at each temperature, the hole-trapping lifetimes obtained from IFTOF measurements are normalized with respect to initial hole-trapping lifetimes at different temperature. The accumulated dose deposited into the sample at different temperature is different since the normalized carrier-trapping lifetime reduced at different rates. The measurements are terminated when the measured hole-trapping lifetime has been reduced to almost 45% of its initial hole-trapping lifetime for all the measurements. The total amount of the accumulated dose for different temperature varies significant. Only a very small amount of dose is deposited in the sample each time at high temperatures. This makes it possible to acquire enough data points in order to calculate the normalized lifetime change rate later. The normalized hole-trapping lifetime reduction due to accumulated dose at different temperatures is plotted in Figure 4.7.

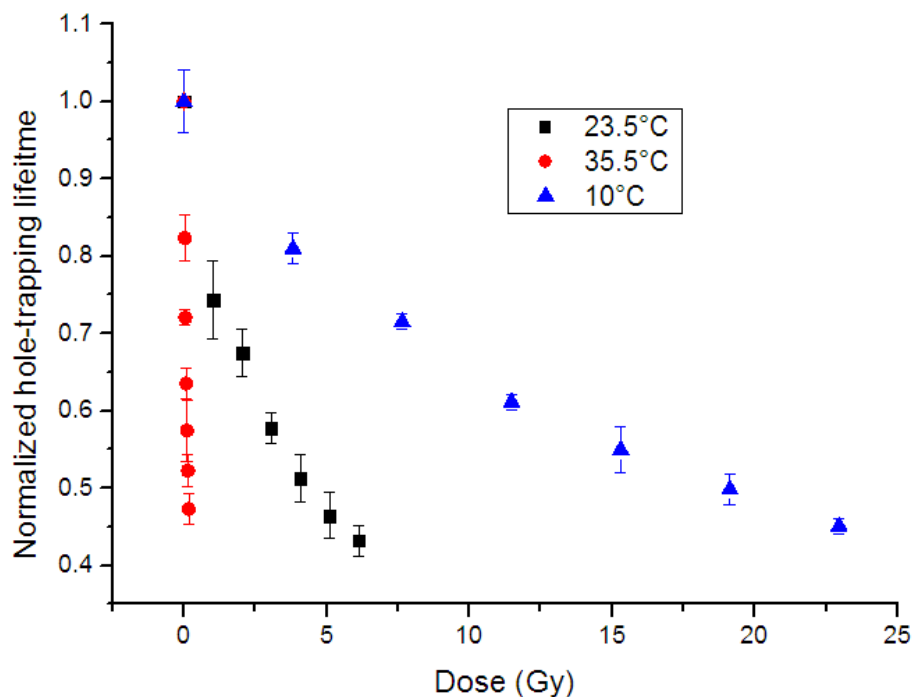


Figure 4.7 Normalized hole-trapping lifetime reduction due to X-ray dose at different temperatures.

At different temperature, as the X-ray dose increases, the hole-trapping lifetime

decreases at a different rate. Similarly to the analysis in the dose rate dependence measurement, the normalized lifetime change rate is introduced. The normalized lifetime change rates at different temperature are listed below in Table 4.11.

Table 4.11 The normalized lifetime change rate of hole at different temperature

Temperature (°C)	Normalized lifetime change rate (Gy ⁻¹)
10	0.054 ± 0.02
23.5	0.231 ± 0.03
35.5	6.61 ± 0.90

The normalized lifetime change rates vary greatly at different temperatures. From 10 to 35.5°C, the normalized lifetime change rate increases by a factor about 122 times. This implies that at higher temperature, same amount of X-ray energy can generate more defects than it at lower temperature. In addition, this increment is not linear from low temperatures to high temperatures. From 10 to 23.5 °C, the normalized lifetime change rate increases about 4 times. From 23.5 to 35.5°C, the normalized lifetime change rate increases about 29 times. At higher temperatures, the normalized lifetime change rate increases more; in other words, it becomes easier for X-ray to induce defects. The strong temperature dependence of the normalized lifetime change suggests that the defects or hole capture rate is probably thermally activated. Indeed if we were to fit an Arrhenius temperature dependence to the three points in Table 4.11, we would find an activation energy of ~ 1.4 eV.

To have a better understanding of the temperature affect in carrier-trapping lifetime reduction, a comparison can be made with previous electron measurements. This comparison is shown in Table 4.12. [21]

Table. 4.12 Comparison with previous measurement on normalized lifetime change rate at different temperature

Temperature°C	a-Se:0.2%As Electron normalized lifetime change rate (Gy ⁻¹)	a-Se:0.3%As:5ppm Cl Hole normalized lifetime change rate (Gy ⁻¹)
10	N/A	0.054 ± 0.02
21 – 23.5	0.052	0.231 ± 0.03
35 ~ – 35.5	0.19	6.61 ± 0.90

For both electrons and holes, the normalized lifetime change rate increases with increasing temperature. The normalized lifetime change rate for holes is larger than that for electron. This indicates that upon deposition of the same amount of dose, the hole-trapping lifetime reduced more than the electron-trapping lifetime. More hole defects are generated than electron defects. In addition, from 21 to 35 °C, the normalized lifetime change rate for electrons increases about 4 times while the normalized lifetime change rate for holes increases about 29 times. This indicates that the X-ray induced lifetime changes are more sensitive to temperature for holes than that for electrons. This result is not completely accurate since the sample compositions are not identical. Based on the previous dose rate measurement, the average normalized lifetime change rate is about 0.043 for a-Se: 0.3%As: 5ppm Cl at room temperature. So a composition difference will cause some variation in the parameters.

Beyond the carrier-lifetime reduction measurement, the carrier lifetime recovery measurements are performed on irradiated samples at different temperature. Three different temperatures, which are the same as the temperatures in the accumulated dose measurement, were chosen. The samples are kept in the dark and the temperatures of the samples remain stable during the whole experiment. The recovery process of hole-trapping lifetime after X-ray irradiation at different temperatures is shown in Figure 4.8.

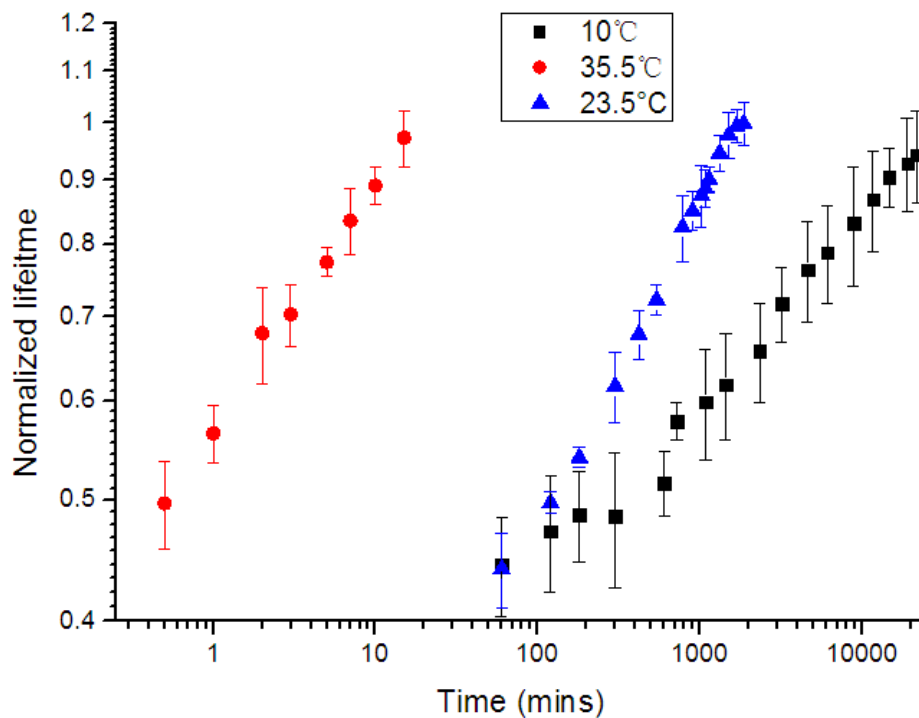


Figure 4.8 Normalized hole-trapping lifetime versus time on a semi-logarithmic plot. The

sample has been pre-irradiated and the normalized lifetime $\tau_{\text{normalized}}$ has decreased as a result of irradiation. $\tau_{\text{normalized}}$ recovers with time.

The X-ray dose amount deposited into the sample initially at different temperatures is the same as that in accumulated dose measurements. The normalized hole-trapping lifetime is reduced to 45% of its initial value. The normalized hole-trapping lifetime begins to recover gradually after the irradiation. At higher temperatures, the time it takes for sample's normalized hole-trapping lifetime to come back to 100% is shorter than that at lower temperature. It takes less than 20 minutes for the normalized hole-trapping lifetime to come back to 100% at 35.5°C. It takes about 2000 minutes (33 hours) for the normalized hole-trapping lifetime to recover back to 100% at 23.5 °C. It takes more than 20000 minutes (14 days) for the normalized hole-trapping lifetime to come back to 100% at 10°C. The hole-trapping lifetime shows a strong dependence in the recovery process of the normalized hole-trapping lifetime. The relaxation process of hole lifetime was observed to follow a stretched exponential behavior. [21] This relaxation process can be well fitted by

$$\tau_{\text{irradiated}} = \tau_{\text{unirradiated}} - (\tau_{\text{unirradiated}} - \tau_{\text{initial}})e^{-\left(\frac{t}{\tau_{\text{sr}}}\right)^\beta} \quad (4.16)$$

or

$$\tau_{\text{normalized}} = 1 - (1 - \tau_0)e^{-\left(\frac{t}{\tau_{\text{sr}}}\right)^\beta} \quad (4.17)$$

where τ_0 is the normalized carrier-trapping lifetime after irradiation, τ_{sr} is the structural relaxation time and β is the exponential stretch coefficient, which is between 0.8-0.9. The structural relaxation time τ_{sr} is different for each sample. It is independent of the X-ray dose, and it is a parameter that characterizes the recovery process of the carrier-trapping lifetime.

When time t is 0, which stands for immediately after irradiation, Equation 4.17 is simplified into

$$\tau_{\text{normalized}} = \tau_0 \quad (4.18)$$

since the exponential term becomes 1. When time t goes to infinity, which means that a sufficient long time has passed, the Equation 4.17 is simplified into

$$\tau_{\text{normalized}} = 1 \quad (4.19)$$

Since the exponential term becomes 0. Equation 4.14 shows that when time is long enough the carrier-trapping lifetime recovers to its unirradiated state. This agrees with the experimental observation. The Equation 4.17 can be also written as using Equation 4.5

$$\frac{\Delta N_r}{N_r} = \frac{\Delta N_0}{N_0} e^{-\left(\frac{t}{\tau_{sr}}\right)^\beta} \quad (4.20)$$

where N_r is the concentration of traps at time t after irradiation and ΔN_r is the excess concentration of traps with respect to unirradiated state; N_0 is the concentration of traps initially at the recovery process and ΔN_0 is the concentration of traps with respect to unirradiated state. As time increases, N_r and ΔN_r both decrease. The ratio $\frac{\Delta N_r}{N_r}$ will follow a stretched exponential decrease with respect to time.

The structural relaxation time for different temperatures is obtained through fitting Equation (4.20) to experimental results. The fitting plots are given in the appendix. The structural relaxation times at three different temperatures are listed in Table 4.13 below.

Table 4.13 Structural relaxation time for different temperatures

Temperature °C	Structural relaxation time (minutes)
10	5836 \mp 1090
23.5	498 \mp 26
35.5	5 \mp 1

The structural relaxation time takes a range from several minutes up to days. From 35.5 to 23.5 °C, the structural relaxation time increases about 100 times. From 23.5 to 10 °C, the structural relaxation time increases about 10 times. Since the structural relaxation time is independent of normalized carrier-trapping lifetime, it provides a useful indication about the relaxation process. At a higher temperature the relaxation process of hole lifetime is much quicker than at a lower temperature. In addition, the lifetime was observed to change with temperature in an Arrhenius fashion, which suggests a thermally activated process. [21] The thermal activation energy can then be calculated based on the results obtained from previous measurements. By plotting the structural relaxation time versus the inverse temperature, the activation energy could be obtained. The structural relaxation time and temperature follows an exponential relationship, which is given by

$$\tau_{sr} \propto \exp\left(\frac{E_{\text{activation}}}{k_B T}\right) \quad (4.21)$$

The activation energy is then obtained through fitting structural relaxation time versus inverse temperature data. The logarithm of structural relaxation time versus the inverse temperature is plotted in Figure 4.9 and the slope of this plot can be used to determine

activation energy. The activation energy is then the product of the slope and the Boltzmann constant. From Figure 4.9, the activation energy is 2.11 ± 0.24 eV for the relaxation of excess hole traps.

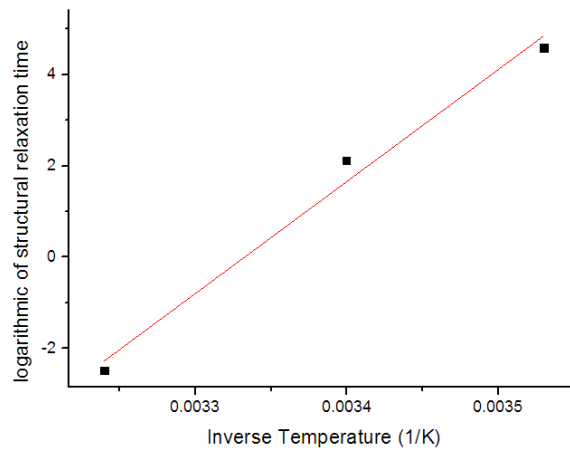


Figure 4.9. The fitting plot of logarithmic structural relaxation time versus inverse temperature.

A comparison can be made between the hole lifetime relaxation process and the electron lifetime relaxation process as shown in Table 4.14. [21]

Table 4.14 Comparison with previous electron measurement

Temperature °C	a-Se:0.2%As (τ_{sr} for electron traps)	a-Se:0.3%As:5ppm Cl (τ_{sr} for hole traps)
10	N/A	98 ± 18 hrs
21 ~ 23.5	3.36 ± 1.8 hrs	8.3 ± 0.4 hrs
35 ~ 35.5	5.9 ± 1.4 mins	5.0 ± 1.0 mins
Activation energy	1.89 ± 0.47 eV	2.11 ± 0.24 eV

The structural relaxation time is quite short at high temperature. The activation energy for relaxation of electron traps is slightly smaller than that for relaxation of hole traps. For both electrons and holes, it shows that as the temperature increases, the structural relaxation time decreases. Since the two samples are not exactly the same, the result of comparison is not completely valid. A small portion of arsenic doping or chlorine doping may significantly change the relaxation process involved in carrier traps. In order to make a valid comparison between hole and electron trap relaxation process, the sample composition should be the same.

In summary, at a higher temperature, the hole-trapping lifetime decreases more upon

receiving the same amount of dose than that at a lower temperature. The hole-trapping lifetime also recovers more quickly at a higher temperature than that do at a lower temperature. The electron-trapping lifetime also has a similar behavior at different temperatures. The temperature effect is valid for both hole and electron traps.

4.5 Capacitance Changes Due to X-ray Irradiation

The experimental goal is to see if there would be difference in the capacitance of the sample caused by X-ray irradiation. Two different samples are used in these experiments and the capacitance changes are listed in Table 4.15 below.

Table 4.15 Samples used in effective capacitance measurements

Sample / Capacitance	Before (pF)	After (pF)
Sample 1: α – Se: 0.03%SeO, 144 μm thickness	51.8	51.6
Sample 2: α – Se: 0.3%As: 5ppm Cl, 114 μm thickness	67.6	66.7

The capacitance changes have shown in Figure 4.10.

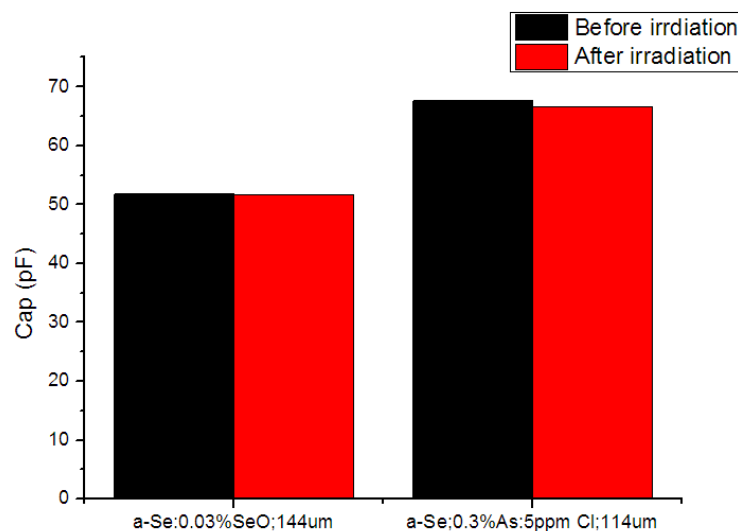


Figure 4.10 Measured capacitance changes due to X-ray

Considering the measurement error in the bridge, which is about 1 %, the changes due

to X-ray irradiation are negligible. The capacitance does not change upon receiving the X-ray irradiation and this indicates that there are no trapped charges in bulk or changes in the relative permittivity. Based on the statements in chapter 2, the unchanged capacitance is mostly likely due to the absence of X-ray induced polarization. There is not enough evidence to say that deposited X-ray dose not generate any electric dipoles in the bulk. This is because the polarization that changes the electric susceptibility of the material is the vector sum of all the single polarization vectors. Deposited X-ray dose may result in the generation of local polarization of the medium but the sum, as indicated by the experiments, is negligible.

4.6 Summary

In this chapter, the results of several X-ray induced changes in electronic properties of amorphous selenium alloy are collected. The X-ray dose that deposited into the sample is measured before the experiment. The maximum dose rate that is used in later experiments is about 2 Gy/s and the minimum is about 0.2 Gy/s.

The carrier-trapping lifetime test has shown the experiment setup is reliable for carrier-trapping lifetime measurements. The dose rate dependence measurements were carried out. Four different dose rates have been applied on the samples during the accumulated dose measurements. The measurements were done for both electrons and holes. The normalized lifetime change rate is obtained for each measurement as well. For hole-trapping lifetime measurement, the normalized lifetime change rate was about 0.2 Gy^{-1} for all different dose rates. For electron-trapping lifetime measurement, the normalized lifetime change rate is about 0.046 Gy^{-1} for all different dose rates. Though the dose rate has an order of magnitude difference, the X-ray induced carrier-trapping lifetime changes were very close for different dose rates.

The temperature effects on X-ray induced hole-trapping lifetime changes have been investigated as well. Three different temperatures 10 °C, 23.5 °C, 35.5 °C were chosen to be the experimental temperature. The accumulated dose measurements at different temperatures provide the normalized lifetime change rates for different temperature. At higher temperature, the hole-trapping lifetime decreases very fast with a normalized lifetime change rate of about 6.6 Gy^{-1} . At the lower temperature, the hole-trapping lifetime decreases very slowly with a

normalized lifetime change rate of about 0.05 Gy^{-1} . The same temperatures are chosen for the study of relaxation process as well. At the higher temperature, the hole-trapping lifetime recovers very quickly with a structural relaxation time of about 5 minutes. At the lower temperature, the hole-trapping lifetime recovers very slowly with a structural relaxation time of about 100 hours. The results are in accord with the results from the electron-trapping lifetime measurements. The activation energy for the relaxation of hole traps is about 2.11 eV. An accurate comparison cannot be made with the activation energy for electron lifetime relaxation due to the composition difference.

The X-ray induced capacitance change measurements were also done for two different samples. The capacitance changes due to X-ray irradiation are negligible.

5. Conclusion and Summary

The research objectives of this project were to investigate the X-ray induced carrier-trapping lifetime changes in amorphous selenium alloy based photoconductive layers. Carrier-trapping lifetime changes due to delivered dose at different dose rates were observed as well as hole-trapping lifetime changes due to delivered dose at different temperatures. These observations provide a deeper understanding of amorphous selenium and these could be useful to improve the performance of amorphous selenium based X-ray detectors.

5.1 X-ray Induced Changes in the Electronic Properties of Amorphous Selenium

The samples that are used in the experiments are a-Se: 0.3% As: 5ppm Cl films. The thickness of the films is about 150 μm . The exposure from the X-ray tube is measured by a dosimeter system and the delivered dose is estimated through a computer program, which includes photon energy dependence of attenuation and absorption coefficients.

One of the major experimental goals was to investigate if there is dose rate dependence in the accumulated and delivered dose measurement. The carrier-trapping lifetime decreases upon the sample receiving X-ray dose. The more X-ray dose that is deposited into the sample the more carrier-trapping lifetime decreases. This is observed for both electrons and holes. The amorphous selenium alloy samples were irradiated under different X-ray dose rates. After receiving a total 10 Gy of X-ray dose, the hole-trapping

lifetime decreased up to 40% of its unirradiated state. After the deposition of a total 20 Gy of X-ray dose, the electron-trapping lifetime decreased up to 60% of its unirradiated state. The dose rate ranged from 0.2 Gy/s up to 2 Gy/s, over an order of magnitude. There was no significant difference between different dose rates. The normalized lifetime change rates, which are used to describe the carrier-trapping lifetime changes due to deposited X-ray dose, are very close between different dose rates. Therefore, the X-ray dose induced carrier-trapping lifetime decrease does not depend on the X-ray dose rate. It makes X-ray imaging system design much simpler since the performance of X-ray detector is independent of the exposure rate to the X-rays

Another experimental goal was to investigate the different temperature effects on X-ray induced hole-trapping lifetime changes. Two types of temperature dependence measurements were done. First, the temperature effects during the accumulated dose measurement were investigated. At higher temperature, the carrier-trapping lifetime decreases faster at the same amount of deposited dose. The normalized lifetime change rates can be different by more than 100 times. Such changes are greater at higher temperatures. The hole-trapping lifetime exhibits a relaxation process after irradiation. At higher temperatures, the relaxation process is very short while it takes a long time at lower temperatures. The structural relaxation time, which is used to characterize the relaxation process, varies sharply with temperature. From 10 °C to 35.5 °C, the difference can be more than 1000 times. These results are in agreement with the previous results obtained from electron-trapping lifetime measurements. At higher temperatures, the amorphous selenium structure is more flexible, which makes it easier for X-ray to generate defects. Because of this flexibility, this is also easier for these defects to relax. This suggests that an optimized mode of operation based on such temperature effects may be developed in order to minimize the accumulated dose effects.

The carrier-trapping lifetime fall with deposited dose leads to a decrease of X-ray sensitivity, which is a metric crucial for the performance of these X-ray detectors. It is shown

that a thicker X-ray detector experience more significant sensitivity loss than a thinner one operating at the same field. It is also shown that a lower applied field will induce a more significant sensitivity loss than a higher applied field. Even though carrier-trapping lifetime may experience up to 50% loss, the X-ray sensitivity loss is only about 1% for a 200 μm thick X-ray detector with 10 $\text{V}/\mu\text{m}$ applied field. This provides some guides to overcome carrier-trapping lifetime changes in X-ray detector design. An additional measurement for capacitance dependence on deposited dose was also done. Two different samples have been irradiated with X-rays for a long time. The capacitance is measured before and after the irradiation. The capacitance change due to deposited dose is negligible. The result suggests that there is no effective internal polarization after the irradiation.

5.2 Future Works

The current research has provided much information on amorphous selenium. The X-ray induced changes in the amorphous selenium have been intensively studied for changes in the mobility and carrier-trapping lifetime. However, there are still many issues to be investigated. The present study on X-ray induced carrier-trapping lifetime changes only investigated the dose rate dependence. It did not include the X-ray energy dependence. The number of defects is proportional to the total amount of X-ray energy deposited into the sample. It does not indicate if low-energy X-ray photons and high-energy X-ray photons have the same contribution. This investigation would provide a better understanding of the performance of the amorphous selenium based X-ray detectors under different X-ray energy range. In order to implement such an experiment, a more monochromatic X-ray source is required. As shown in the previous chapters, the conventional X-ray tube only provides a continuous spectrum of X-rays. Therefore, it is necessary to add some filters to the current X-ray tube or to replace the current X-ray tube with a synchrotron source. Besides the damage process, some experiments could be done on the recovery process as well. Bandgap of sub-bandgap light may have effects on the relaxation process of the defects generated by

the X-ray. However, the actual mechanism remains unknown. The amorphous selenium has an absorption band gap about 532nm. [21] Therefore; three separate experiments could be done on the relaxation process. One is in the dark, one is irradiated by a laser with wavelength below 532 nm, and the other is irradiated by a laser with wavelength above 532 nm. The goal of the experiment would be to see if there is a difference caused by photons during the relaxation process. In addition, it would also help to understand if this difference is caused by absorption of photons or something else. Since the TOF and IFTOF are two powerful techniques for mobility and carrier-trapping lifetime measurement, the present study can also be applied to other potential X-ray detector materials.

6. Reference

- [1] Kasap S.O. and Rowlands J.A., “Review: X-ray photoconductors and stabilized a-Se for direct conversion digital flat-panel x-ray image detectors”, *Journal of Materials Science: Materials in Electronics*, 11, 2000, pp. 179-198.
- [2] Bone J.M., “ Chapter 1: X-ray production, interaction, and detecting in diagnostic imaging”, *Handbook of Medical Imaging: Volume 1. Physics and Psychophysics*, edited by Beutel J., Kundel H.L., and VanMetter R.L., SPIE Press, Bellington, 2000, pp. 1-78
- [3] Fogal B. *Electronic Transport Properties of Stabilized Amorphous Selenium X-ray Photoconductors*, M.Sc Thesis, University of Saskatchewan, 2005
- [4] Ritman E, “X-ray phase-based imaging: the third wave”, *Acad Radiol* 2009;16(8):909–10.
- [5] Conner D.M, Zhong Z., “ Diffraction Enhanced Imaging”, *Curr Radiol Rep* (2014) 2:55
- [6] Chapman D., Thomlinson W., Johnston R.E, Washburn D., Pisano E., Gmur N., Zhong Z, Menk R, Arfelli F, Sayers D. “ Diffraction Enhanced X-ray Imaging”, *Phys. Med. Biol* 42 (1997)
- [7] DeHaven S.L. “Microstructured Optical Fiber for X-ray detection”, NASA Technical Reports. PACS: 07.85.Fv, 29.40.Mc, 42.81.Wg, 42.81.Pa
- [8] Kim H.K, Cunningham I.A, Yin Z., Cho G., “ On the Development of Digital Radiography Detectors: A Review”, *International Journal of Precision Engineering and Manufacturing* Vol.9 No.4 pp.86-100. (2008)
- [9] Kasap S., Koughia C., Berashevich J., Johnason R., Reznik A., “ Charge transport in pure and stabilized amorphous selenium: re-examination of the density of states distribution in the mobility gap and the role of defects”, *J Mater Sci: Mater Electron* (2015) 26:4644–4658
- [10] Kasap S.O., “X-ray sensitivity of photoconductors: application to stabilized a-Se”, *Journal of Physics D: Applied Physics*, 33, 2000, pp. 2853-2865.
- [11] Suzuki K., *Amorphous and Microcrystalline Semiconductor Devices: Optoelectronic Devices*, edited by J.Kanicki, Artech House, Boston, 1991, Ch.3.

- [12] Que W. and Rowlands J.A., “X-ray photogeneration in amorphous selenium: geminate versus columnar recombination”, *Physical Review B*, 51, 1995, pp. 10500-10507.
- [13] Kasap S.O. and Rowlands J.A., “Direct-conversion flat-panel x-ray image detectors”, *IEEE Proceedings: Circuits, Devices, and Systems*, 149, 2002, pp. 85- 96.
- [14] Kasap S.O., Frey J.B., Belev G., Tousignant O., Mani H., Greenspan J., Laperriere Luc., Bubon O., Reznik A., DeCrescenzo G., Karim K.S., Rowlands J.A. “Amorphous and Polycrystalline Photoconductors for Direct Conversion Flat Panel X-Ray Image Sensors” *Sensors* **2011**, *11*(5), 5112-5157
- [15] Haugen C., Kasap S., Rowlands J. “ Charge Transportation and Electron-Hole-Pair Creation Energy in Stabilized a-Se based Photoconductors”, *J. Phys. D: Appl. Phys.* 32 (1999) 200–207
- [16] Frey J. *AN EXPERIMENTAL AND THEORETICAL STUDY OF THE DARK CURRENT AND X-RAY SENSITIVITY OF AMORPHOUS SELENIUM X-RAY PHOTOCONDUCTORS*, Ph.D thesis, University of Saskatchewan, 2011
- [17] Simon M., Ford R.A, Franklin A.R., Grabowski S.P, Menser B., Much G., Nascetti A., Overdick M., Powell M.J., Wiechert D.U. “Analysis of Lead Oxide (PbO) Layers for Direct Conversion X-Ray Detection”, *IEEE TRANSACTIONS ON NUCLEAR SCIENCE*, VOL. 52, NO. 5, OCTOBER 2005
- [18] Zentai G., Schieber M., Partain L., Pavlyuchkova R., Proano C. “Large area mercuric iodide and lead iodide X-ray detectors for medical and non-destructive industrial imaging”, *Journal of Crystal Growth* 275 (2005) e1327–e1331
- [19] Yakunin S., Sytnyk M. Kriegner D., Shrestha S., Richter M., Matt G., Azimi H., Brabec C.J., Stangl J., Kovalenko M.V, Heiss W., “ Detection of X-ray photons by solution-processed lead halide perovskites ”, *Nature Photonics* Vol 9. (2015)
- [20] Roo J.D, Ibanez M., Geiregat P., Nedelcu G., Walravens W., Maes J., Martins J.C, Driessche I.V., Kovalenko M.V., Hens Z., “Highly Dynamic Ligand Binding and Light Absorption Coefficient of Cesium Lead Bromide Perovskite Nanocrystals”, *ACS Nano* 2016, 10, 2071-2081
- [21] Walornyj M. *ELECTRON LIFETIME AND ITS DEPENDENCE ON TEMPERATURE AND DOSE IN a-Se PHOTOCONDUCTORS*, M.Sc thesis, University of Saskatchewan, 2013
- [22] Street R.A., *Hydrogenated amorphous silicon*, Cambridge University Press, London

1990

- [23] Mott N.F., "Electrons in disordered structures", *Advances in Physics*, 16, 1967, pp. 49-57.
- [24] Mott N.F. and Davis E.A., *Electronic processes in non-crystalline materials*, Clarendon Press, Oxford, 1979.
- [25] Cohen M.H., Fritzsche H. and Ovshinski S.R., "Simple band model for amorphous semiconductor alloys", *Physical Review Letters*, 22, 1969, pp. 1065-1068.
- [26] Marshall J.M. and Owen A.E., "Drift mobility studies in vitreous arsenic triselenide", *Philosophical Magazine*, 24, 1971, pp. 1281-1290.
- [27] Lucovsky G. *Physics of selenium and tellurium*, edited by E. Gerlach and P. Grosse, Springer-Verlag, vol.13, New York, 1979, pp. 178-192
- [28] Lucovsky G. and Galeener F.L., "Intermediate range order in amorphous solids", *Journal of Non-Crystalline Solids*, 35-36, 1980, pp. 1209-1214.
- [29] S.O. Kasap, Chapter 9: "Photoreceptors - The Chalcogenides", in *The Handbook of Imaging Materials*, Second Edition, (Marcel Dekker, New York, 2002), 329-368
- [30] Abkowitz M., "On the question of chain-end ESR in amorphous selenium", *Journal of Chemical Physics*, 46, 1967, pp. 4537-4538.
- [31] Agarwal S.C., "Nature of localized states in amorphous semiconductors- a study by electron spin resonance", *Physical Review B*, 7, 1973, pp. 685-691.
- [32] Adler D. and Yoffa E.J., "Localized electronic states in amorphous semiconductors", *Canadian Journal of Chemistry*, 55, 1977, pp. 1920-1929.
- [33] Abkowitz M., "Density of states in a-Se from combined analysis of xerographic potentials and transient transport data", *Philosophical Magazine Letters*, 58, 1988, pp. 53-77.
- [34] Spear W.E., "Transit time measurements of charge carriers in amorphous selenium films", *Proceedings from the Physical Society of London*, B70, 1957, pp. 669-675.
- [35] Marshall J.M. and Owen A.E., "The hole drift mobility of vitreous selenium", *Physica Status Solidi A*, 12, 1972, pp. 181-191.
- [36] Orłowski T.E. and Abkowitz M., "Microstripline transient photocurrents in a-Se

- structure resolved in shallow and tail states”, Solid State Communications, 59, 1986, pp. 665-668
- [37] Abkowitz M., “Evidence of the defect origin of states which control photoelectric behavior of amorphous chalcogenides”, Journal of Non-Crystalline Solids, 66, 1984, pp. 315-320.
- [38] Abkowitz M., “Relaxation induced changes in electrical behavior of glassy chalcogenide semiconductors”, Polymer Engineering Science, 24, 1984, pp. 1149-1154.
- [39] Abkowitz M. and Markovics J.M., “Evidence of equilibrium native defect populations in amorphous chalcogenides from analysis of xerographic spectra”, Philosophical Magazine B, 49, 1984, pp.L31-L36
- [40] Pai D.M. “Time-of-flight study of the compensation mechanism in a-Se alloys”, Journal of Imaging Science and Technology, 41, 1997, pp 135-142.
- [41] Hartke J.L. and Regensburger P.J., “Electronic states in vitreous selenium”, Physical Review, 139, 1965, pp. A970-A980.
- [42] Davis E.A., “Optical absorption, transport and photoconductivity in amorphous selenium ”, Journal of Non-Crystalline Solids, 4, 1970, pp. 107-116.
- [43] Adachi H. and Kao K.C., “Dispersive optical constants of amorphous selenium $Se_{1-x}Te_x$ films ”, Journal of Applied Physics, 51, 1980, pp. 6326-6331.
- [44] Pai D.M. and Enck R.C., “Onsager mechanism of photogeneration in amorphous selenium ”, Physical Review B, 11, 1975, pp. 5163-5174.
- [45] White S.C., Pharoah M.J., Goaz P.W., *Oral Radiology: Principles and Interpretation* Elsevier- Health Sciences Division ,1999, pp. 20-22.
- [46] Kasap S.O. and Juhasz C. "Time-of-flight drift mobility measurements on chlorine-doped amorphous selenium films", *J. Phys. D: Appl. Phys.* **18** 703, 1985
- [47] Kasap S.O., Polischuk B., Dodds D. and Yannacopoulos S. "Charge trapping studies in a-Se films via interrupted field TOF technique" Journal of Non-Crystalline Solids Volume 114, Part 1, 1 December 1989, Pages 106-108
- [48] Polischuk B., Interrupted Field Time-of-Flight Transient Photoconductivity Technique and its Applications to Amorphous Semiconductors, Ph. D. Thesis, University of Saskatchewan, Saskatoon, Canada, 1994.

- [49] Spear W.E., “Drift mobility techniques for the study of electrical transport properties in insulating solids”, *Journal of Non-Crystalline Solids*, 1, 1969, pp. 197-214.
- [50] Kasap, S.O., *Optoelectronics and Photonics: Principles and Practices*, Prentice Hall, Upper Saddle River, New Jersey, 2001.
- [51] Hecht K. “Zum mechanismus des lichtelektrischen primarstromes in isolierenden kristallen”, *Zeitschrift Fur Physik*, 77 ,1932, pp. 235-245
- [52] Zanio K.R., Akutagawa W.M., and Kikuchi R., “Transient currents in semi-insulating CdTe characteristic of deep traps”, *Journal of Applied Physics*, 39, 1968, pp. 2818-2828.
- [53] Akutagawa W. and Zanio K., “The possibilities of using CdTe as a gamma spectrometer”, *IEEE Transactions on Nuclear Science*, 15, 1968, pp. 266-274.
- [54] Nerdoly M.T.A., *X-ray Sensitivity and X-ray Induced Charge Transport Changes in Stabilized a-Se Films*, Ph. D. Thesis, University of Saskatchewan, Saskatoon, Canada, 2000.
- [55] Martini M., Mayer J.W., and Zanio K.R., “Drift velocity and trapping in semiconductors – transient charge technique”, *Applied State Science: Advances in Materials and Device Research* , edited by R. Wolfe, Academic Press, 1972.
- [56] Blakney R.M. and Grunwald H.P., “Small-signal current transients in insulators with traps”, *Physical Review*, 159, 1967, pp. 658-664.
- [57] Blakney R.M. and Grunwald H.P., “Trapping processes in amorphous selenium”, *Physical Review*, 159, 1967, pp. 664-671.
- [58] Kasap S.O., Thakur R.P.S., and Dodds D., “Method and apparatus for interrupted transit time transient photoconductivity measurements”, *Journal of Physics E: Scientific Instrumentation*, 21, 1988, pp. 1195-1202.
- [59] Jackson J.D. *Classical Electrodynamics Third Edition*, John Wiley & Son inc 1998.
- [60] Gendex Corp, *GX-1000 intra oral x-ray system installation/maintenance manual*. Gendex Corp, Milwaukee, WI, USA
- [61] Helfrich W. and Mark P., “Space charge limited currents in anthracene as a means of determining the hole drift mobility”, *Zeitschrift Fur Physik*, 166, 1962, pp. 370-385
- [62] Allen. C.S, *Relaxation in the Electrical Properties of Amorphous Selenium Based Photoconductors*, M.Sc thesis, University of Saskatchewan, 2009

Appendix A

The program, dose.py, which is used to calculate the dose deposited into the sample is listed in this appendix. The dose.py is used to calculate the dose deposited into the sample. It is based on the X-ray dose estimation in Chapter 2. It combines the experimental measurement and theoretical estimation. The code is written in python 2.7 but it can be also applied in other language.

The code is listed below

```
.....  
##import library  
import os import  
string import  
numpy as np import  
shutil  
  
##.....  
## The main program is dose.py and it consists of three major parts.  
## spectrum.py imports the X-ray energy spectrum from the library  
## thickness.py calculates the mass-attenuation effect which is related to thickness  
## acoeff.py imports the attenuation coefficient from the library  
## Norm.py normalized the flux based on the exposure measurement in the lab  
## integral.py is a integration function  
##.....  
  
##.....  
## Note that the spectrum of the X-ray tube can be directly measured by spectrometer or  
## One can use the X-ray spectrum simulator from Siemens:  
## http://www.oem-products.siemens.com/x-ray-spectra-simulation  
## The attenuation coefficient can be obtained from NIST or other X-ray material handbook  
##.....  
  
##.....  
##spectrum(pkv) convert the strings in the text file into float numbers in a list  
##pkv is the peak-voltage chosen for the X-ray tube def  
spectrum(pkv):
```

```

name=pkv+'.txt'
file=open(name,'r')
kvp=file.read()
strlst=kvp.split()
L=len(strlst)
lst1=[] lst2=[]
N=0
## the separates the energy strings and photon flux strings in the files.
while L>0:      if N%2==0:
                lst1+=[float(strlst[N])]
                N+=1
L-=1          else:
                lst2+=[float(strlst[N])]
                N+=1
L-=1
lst=[lst1,lst2]
return lst
##.....
##.....
## integral function that integrals the four lists.
def integral(lst1,lst2,lst3,lst4):
    L=len(lst1)
    N=0
    Total=0
    while L>0:
        Total+=lst1[N]*lst2[N]*lst3[N]*lst4[N]
        N+=1
    L-=1      return
    Total
##.....

##.....
## Position coefficient
## thickness calculates the attenuation effects brought by thickness
## L is the thickness list. If it contains the two variable x1 and x2. The thickness if x2-x1 ##
rho is the density of material; material is the name of material.
def thickness(L,rho,material,lst):
    if L[-1]=='L':
        Lposition=0
        Rposition=float(L[:-1])
    else:
        Lposition=float(L)*0.9999
    Rposition=float(L)*1.0001
    name=material+'mass'

```

```

mlst=spectrum(name)
col_len=len(lst)    mlst1=mlst[0]
    Dex=mlst1.index(lst[0])
Aex=Dex+col_len
coeff_lst=mlst[1][Dex:Aex]
    Diff_L=Rposition-Lposition
Length=col_len    thick_lst=[]
density=float(rho)
    Num=0
while Length>0:
## var is the thickness effect at each energy
var=(np.exp(-1*density*coeff_lst[Num]*Lposition)-np.exp(-1*density*coeff_lst[Num]*Rposition))/Diff_L
thick_lst+=[var]
    Num+=1
Length-=1    return
thick_lst

```

```
##.....
```

```
##.....
```

```
##  attenuation coefficient def
```

```
acoeff(M,lst):
```

```
    M_energy=M+'energy'
```

```
M_mass=M+'mass'
```

```
lst_energy=spectrum(M_energy)
```

```
lst_mass=spectrum(M_mass)
```

```
lst_e=lst_energy[1]
```

```
lst_m=lst_mass[1]    coeff_lst=[]
```

```
L=len(lst)
```

```
    Initial_energy=lst[0]
```

```
    dex=lst_energy[0].index(Initial_energy)
```

```
N=dex    while L>0:
```

```
        ratio=lst_e[N]/lst_m[N]
```

```
coeff_lst+=[ratio]
```

```
        L-=1
```

```
N+=1
```

```
    return coeff_lst
```

```
##.....
```

```
##.....
```

```
##  Norm coefficient; pkv is the peak voltage and Rontgen is the readout from Dosimeter
```

```
def Norm(pkv,Rontgen):    W_e=34.4    echarge=1.602e-19    coeff=2.58e-7
```

```
rho_air=1.205e-3    R=float(Rontgen)    lst_spectrum=spectrum(pkv)
```

```
lst1=lst_spectrum[0]    lst_coefficient=acoeff('Air',lst1)
```

```
    lst_position=thickness('1.2L','1.25e-3','Air',lst1)
```

```

    Energy=integral(lst_spectrum[0],lst_spectrum[1],lst_coefficient,lst_position)
    Q_ideal=1000*Energy*echarge/W_e
    Q_real=R*coeff*rho_air
Ratio=Q_real/Q_ideal
return Ratio
##.....

##.....
## Dose calculation function
## It calculates the dose deliver to position x or average dose into thickness L by R(Rontgen) irradiation def
dose():
    Kvp=raw_input("Enter the peak voltage(kvp) of the X-ray tube:")
    Material=raw_input("Enter the material for dose calculation:")
    Position=raw_input("Enter the position(cm) of the sample for dose calculation, if it is for average dose
please enter thickness+L(eg. 0.015L for average dose over 0.015cm sample):")
    Rontgen=raw_input("Enter the read out from ionization chamber(R):")
    Density=raw_input("Enter the density of the sample(g/cm^3):")
    lst_spectrum=spectrum(Kvp)
lst1=lst_spectrum[0]
lst_coefficient=acoeff(Material,lst1)
    lst_position=thickness(Position,Density,Material,lst1)
    Energy=integral(lst_spectrum[0],lst_spectrum[1],lst_coefficient,lst_position)
Norm_coefficient=Norm(Kvp,Rontgen)    rho=float(Density)
    Dose=Energy*Norm_coefficient/rho*1.6e-13
return Dose
.....

```

Appendix B

In the chapter 4 a lot of results only have final numerical number. The measurement result and fitting plot is not shown in the chapter 4. The fitting applies the mean value for each measurement and the results for each measurement are listed in this part.

Dose rate measurement

Hole lifetime measurement

Dose rate = 1.95 Gy/s

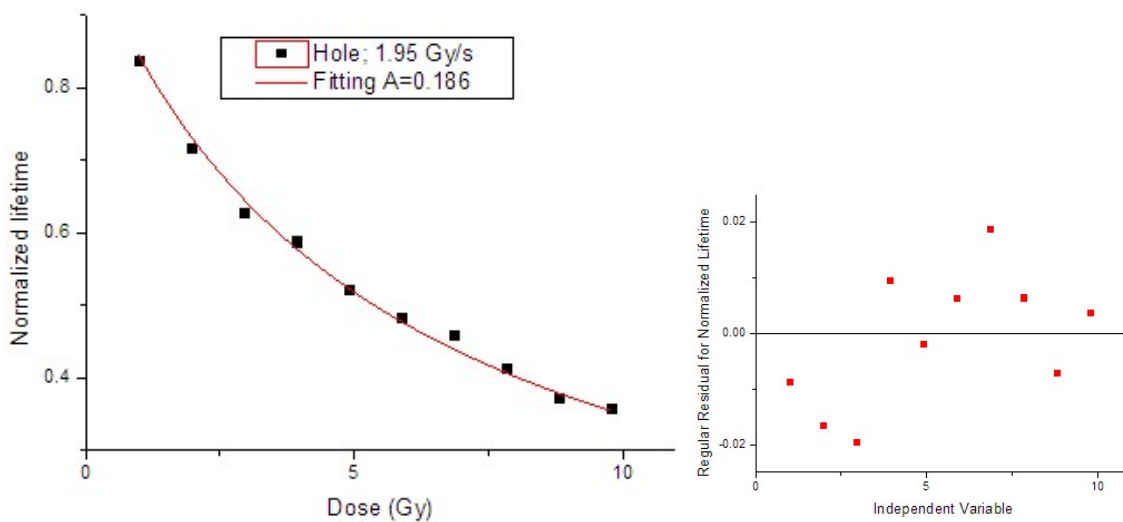


Figure 1 Accumulated dose measurement for hole at dose rate 1.95 Gy/s. The left diagram is the fitting plot of the normalized lifetime versus dose. The right is the regular residual for the data points.

Dose Rate = 0.37 Gy/s

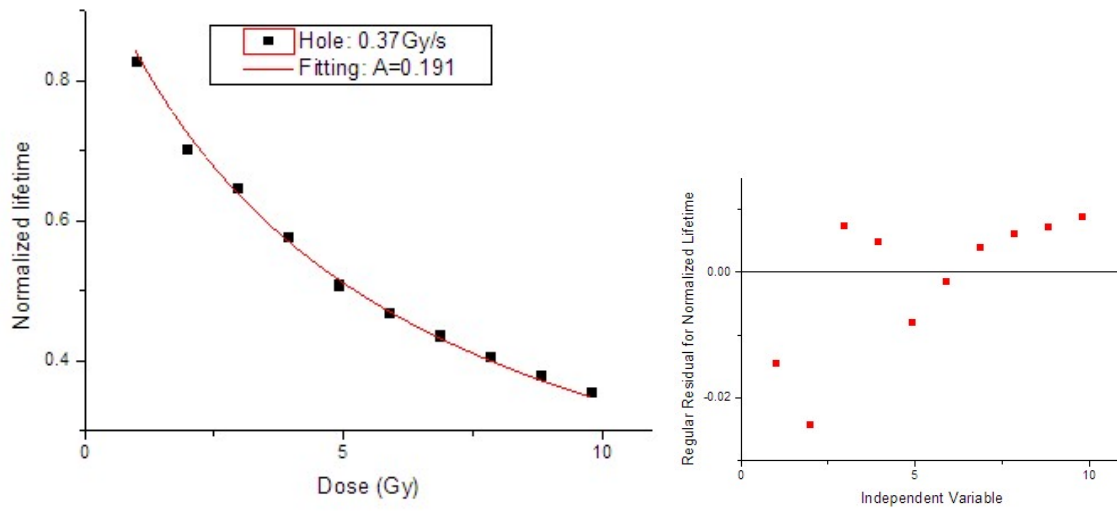


Figure 2 Accumulated dose measurement for hole at dose rate 0.37 Gy/s. The left diagram is the fitting plot of the normalized lifetime verse dose. The right is the regular residual for the data points.

Dose rate=0.26 Gy/s

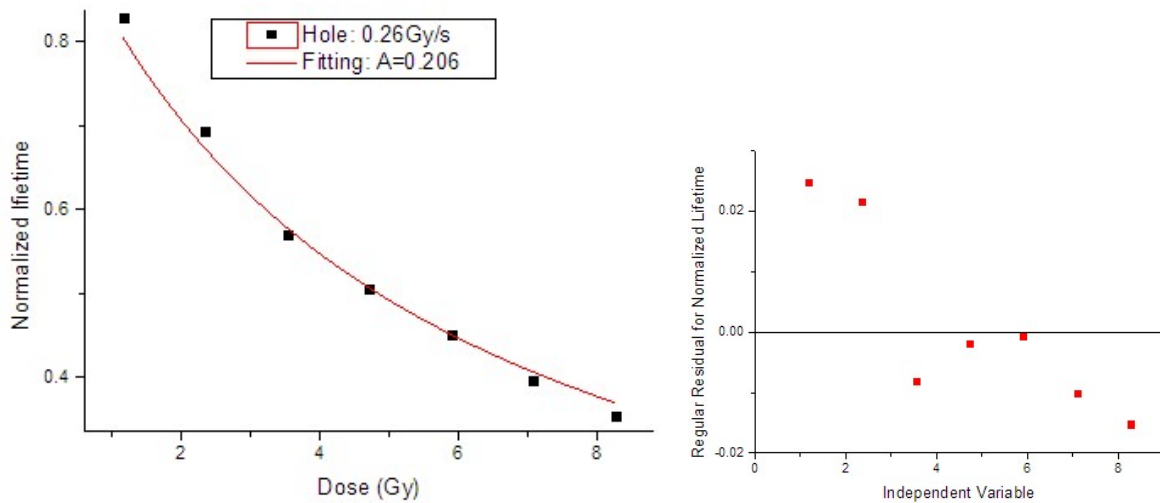


Figure 3 Accumulated dose measurement for hole at dose rate 0.26 Gy/s. The left diagram is the fitting plot of the normalized lifetime verse dose. The right is the regular residual for the data points.

Dose rate = 0.17 Gy/s

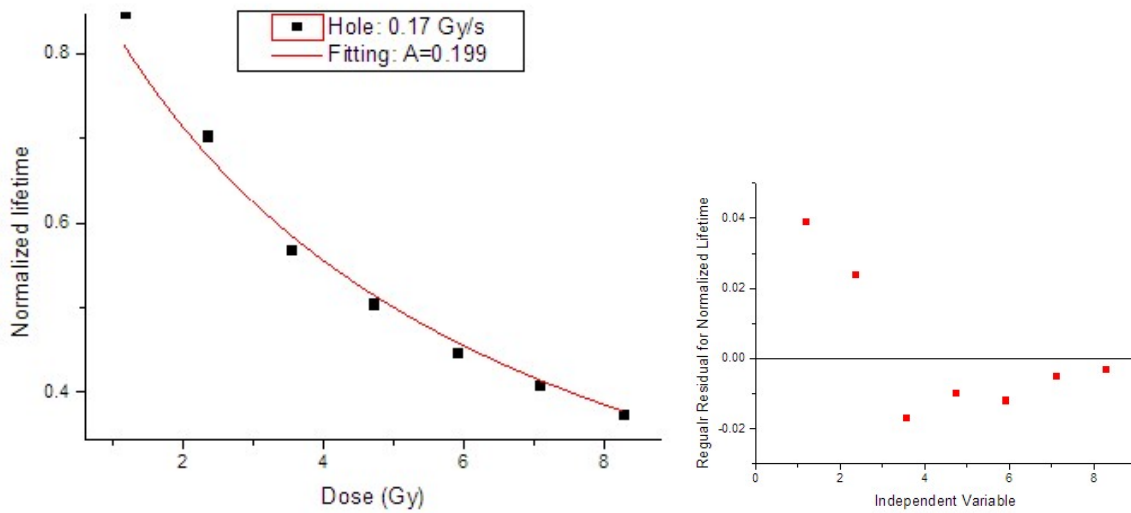


Figure 4 Accumulated dose measurement for hole at dose rate 0.17 Gy/s. The left diagram is the fitting plot of the normalized lifetime verse dose. The right is the regular residual for the data points.

Dose rate measurement

Electron lifetime measurement

Dose rate = 1.95 Gy/s

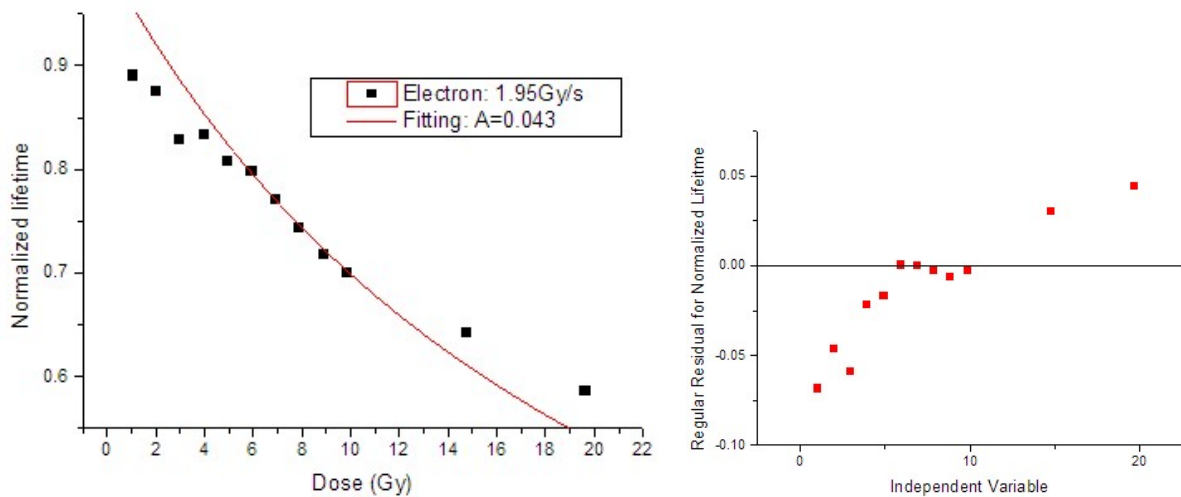


Figure 5 Accumulated dose measurement for electron at dose rate 1.95 Gy/s. The left diagram is the fitting plot of the normalized lifetime verse dose. The right is the regular residual for the data points.

Dose rate = 0.29 Gy/s

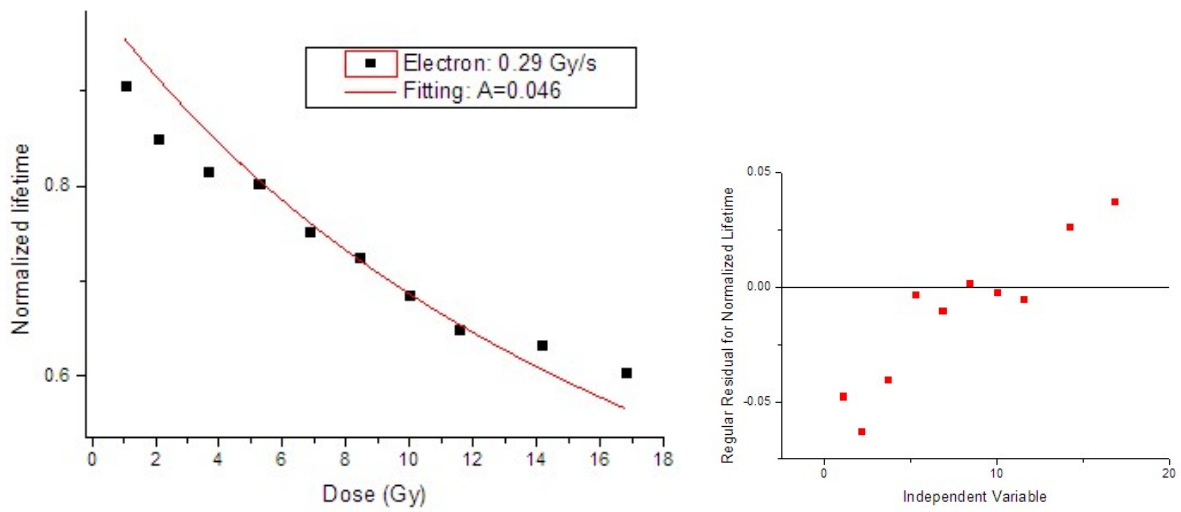


Figure 6 Accumulated dose measurement for electron at dose rate 0.29 Gy/s. The left diagram is the fitting plot of the normalized lifetime verse dose. The right is the regular residual for the data points.

Dose rate = 0.26 Gy/s

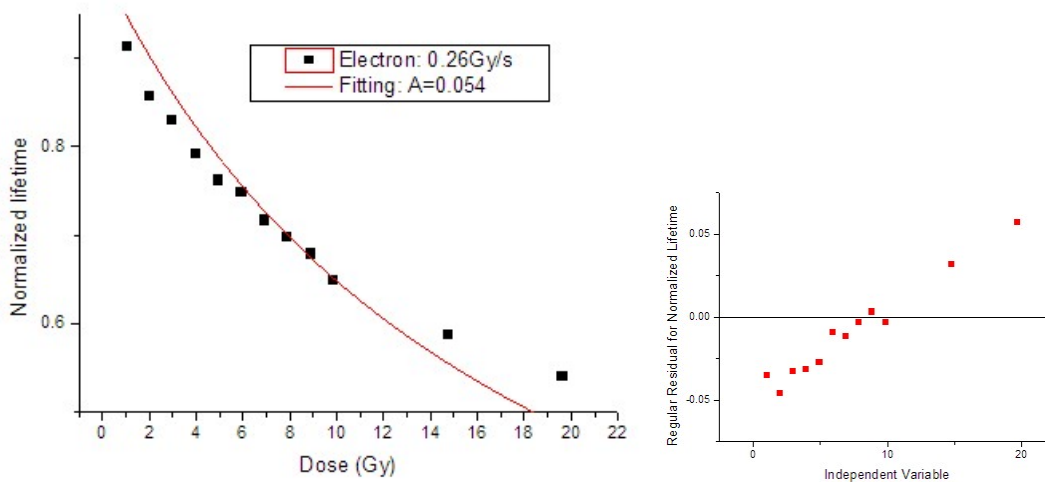


Figure 7 Accumulated dose measurement for electron at dose rate 0.26 Gy/s. The left diagram is the fitting plot of the normalized lifetime verse dose. The right is the regular residual for the data points.

Dose rate = 0.19 Gy/s

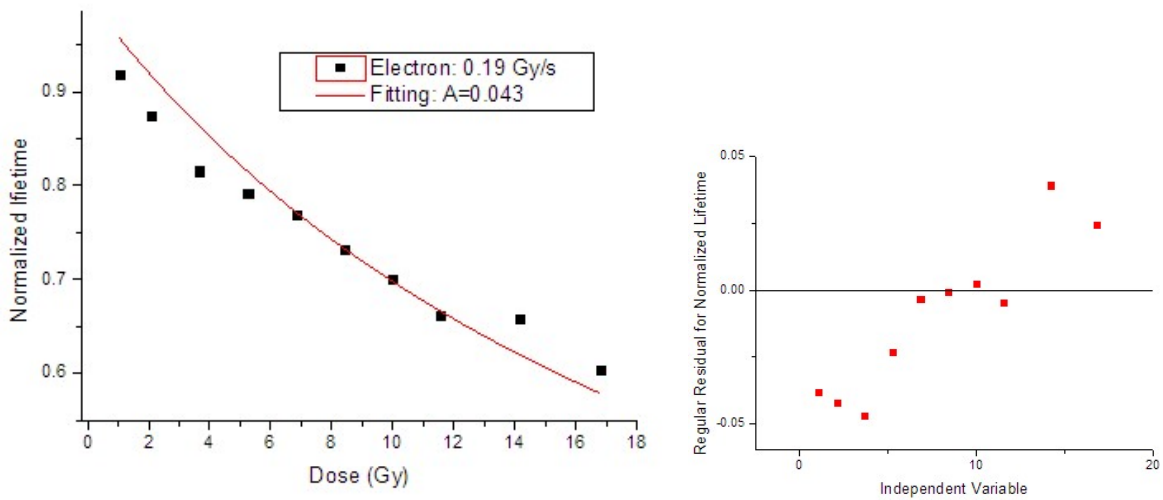


Figure 8 Accumulated dose measurement for electron at dose rate 0.19 Gy/s. The left diagram is the fitting plot of the normalized lifetime verse dose. The right is the regular residual for the data points.

Temperature effects measurement

Accumulated dose measurements at different temperature

T = 10 °C

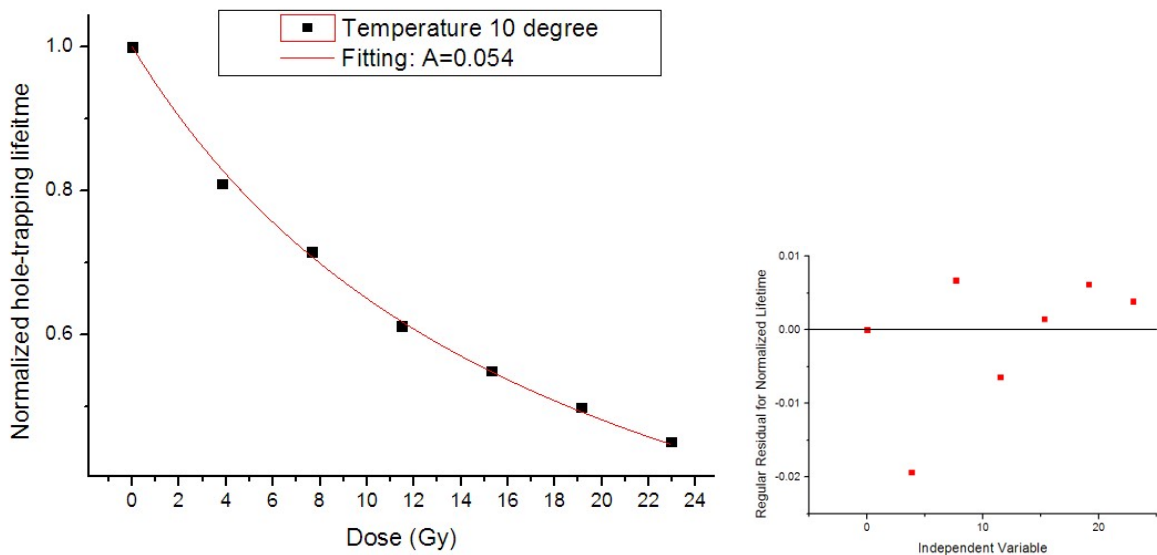


Figure 9 Accumulated dose measurement for hole at 10 °C. The left diagram is the fitting plot of the normalized lifetime verse dose. The right is the regular residual for the data points.

T= 23.5 °C

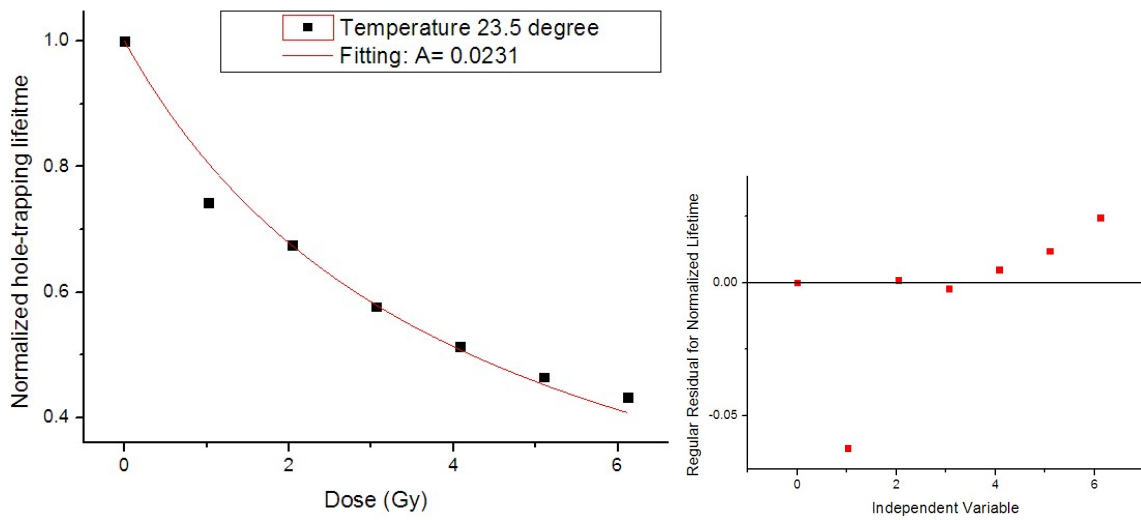


Figure 10 Accumulated dose measurement for hole at 23.5 °C. The left diagram is the fitting plot of the normalized lifetime verse dose. The right is the regular residual for the data points.

T=35.5 °C

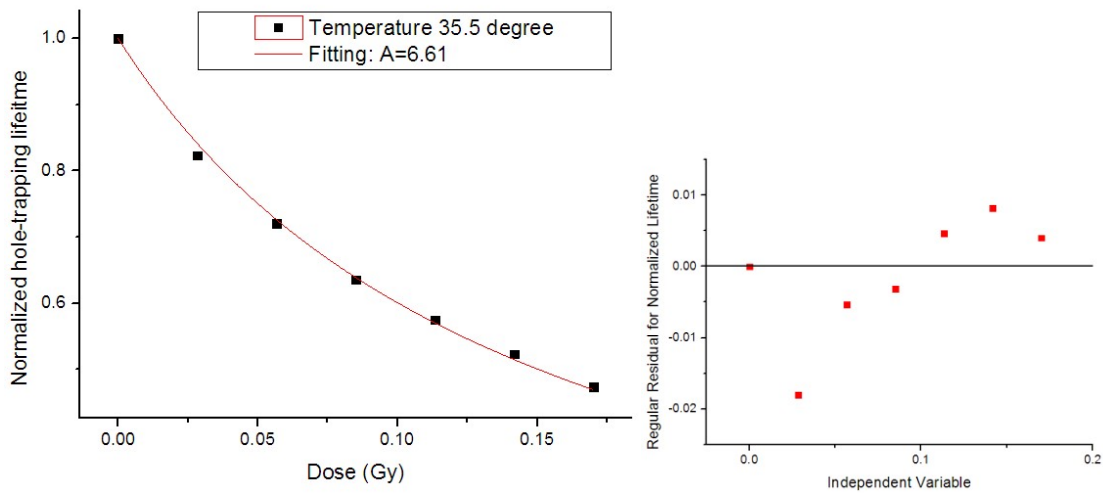


Figure 10 Accumulated dose measurement for hole at 35.5 °C. The left diagram is the fitting plot of the normalized lifetime verse dose. The right is the regular residual for the data points.

Relaxation Process

T = 10 °C

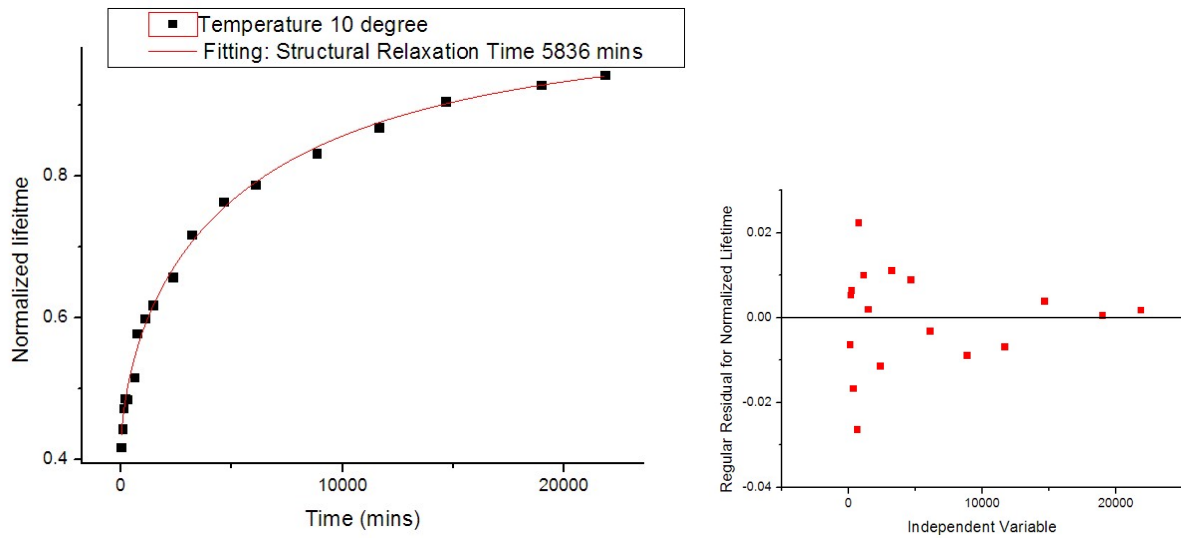


Figure 11 Hole-trapping lifetime relaxation process at 10 °C. The left diagram is the fitting plot of the normalized lifetime verse time. The right is the regular residual for the data points.

T = 23.5 °C

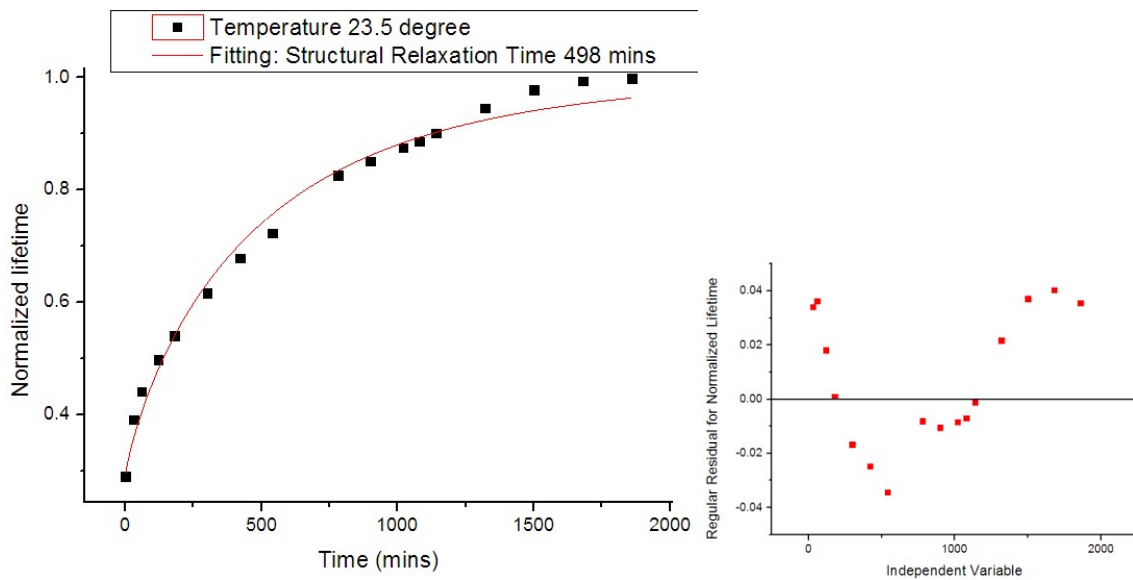


Figure 12 Hole-trapping lifetime relaxation process at 23.5 °C. The left diagram is the fitting plot of the normalized lifetime verse time. The right is the regular residual for the data points.

T = 35.5 °C

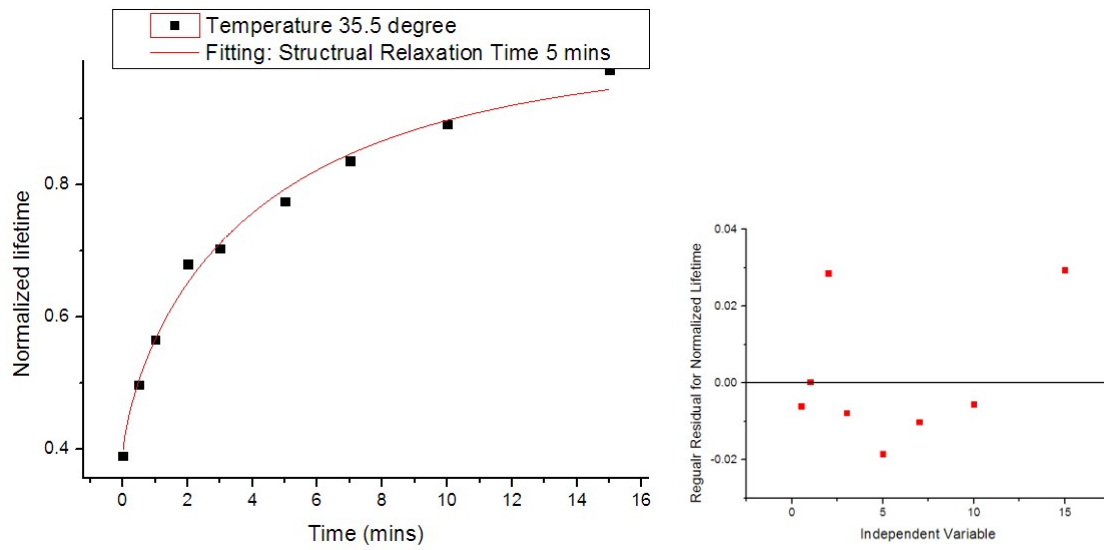


Figure 13 Hole-trapping lifetime relaxation process at 35.5 °C. The left diagram is the fitting plot of the normalized lifetime verse time. The right is the regular residual for the data points.